POLITECNICO DI MILANO

School of Industrial and Information Engineering

Department of Electronics, Information and Bioengineering

Integration of Magnetic Resonance Imaging and fundus photography for a personalized eye model in proton therapy of ocular tumours.

M.Sc. Thesis by:

Luca Antonioli, 899230

Supervisors: Prof. Guido Baroni, PhD

Jan Hrbacek, PhD

Co-Supervisors: Chiara Paganelli, PhD

Riccardo Via, PhD

Academic Year: 2018-2019

Contents

List of abbreviations

CT	Computed Tomography
MRI	Magnetic Resonance Imaging
PET	Positron Emission Tomography
SRT	Stereotactic Radiotherapy
EBRT	External Beam Radiation Therapy
COMS	Collaborative Ocular Melanoma Study
GTV	Gross Tumor Volume
PTV	Planning Tumor Volume
CTV	Clinical Target Volume
OPT	Ocular Proton Therapy
TPS	Treatment Planning System
ETS	Eye Tracking System
LED	Light Emitting Diode
PSI	Paul Scherrer Institut
UM	Uveal Melanoma
OM	Ocular Melanoma
US	Ultrasounds
OCT	Optical Coherence Tomography
SOBP	Spread Out Bragg Peak
LET	Linear Energy Transfer
RBE	Relative Biological Effectiveness
FOV	Field Of View
OHN	Optic Nerve Head

Abstract

Uveal melanomas are relatively rare (representing the 3-5% of all the melanomas), but highly malignant disease, for which until the 1970s the primary therapeutic choice was organ enucleation, i.e. the complete removal of the organ in order to avoid tumour spread. In the last decades however, treatment modalities have moved towards more conservative approaches aiming at avoiding eye enucleation and loss of sight: proton therapy and brachytherapy are nowadays considered the clinical standard for treating ocular tumors. Ocular proton therapy (OPT), thanks to its high geometrical selectivity and sharp dose fall-off, is considered the gold standard for uveal melanomas developing in the posterior eye region and thicker than 5 mm. The local tumor control reported by several institutions is as high as 90%.

OPT however requires an invasive surgical procedure in which radiopaque tantalum markers are sutured onto the sclera of the diseased eye. Clips are implanted for three main reasons: firstly, they are used to create a generic geometrical eye model, by which the sclera surface is fitted to the 3D positions of the clips determined by x-ray imaging; secondly, they serve as landmarks for defining the tumor base and therefore calculate the clinical target volume (CTV). i.e. the volume to be irradiated with protons; finally, they are used as a geometrical reference for precise patient positioning (tumor/proton-beam alignment) before treatment. However, the surgical procedure for placing the clips is expensive and obviously invasive for the patient.

This work of thesis is part of an ongoing research project between Politecnico di Milano and Paul Scherrer Institut (Villigen, Switzerland) aiming at the realization of a complete ocular melanoma treatment workflow without the use of clips. As such, for each task that the clips accomplish it is necessary to find and to evaluate alternatives. In particular, the use of MR imaging for defining the eye model, tumor and critical structures and eye tracking technology for eye localization before and during treatment have already been investigated and identified as pillars of this novel treatment workflow. This work of thesis consists in realizing a complete eye model based on the patient specific anatomy starting from the MRI scans. In particular, the aim of this work is to improve MRI-based target volume definition within the MRI model by including additional information that come from another imaging

modality, the fundus photography. The fundus image is a high resolution photograph of the inner surface of the eye, acquired through the pupil aperture with a dedicated camera; in the best case scenario it is able to capture the tumor and the notable eye structures such as macula, optic disk and blood vessels.

As previously mentioned, the conventional clinical workflow for target volume definition is based on geometrical references provided by the clips. During the surgical intervention, the surgeon performs manual measurements of the distances between the clips and lesion, and between clips to clips. This information is fed to a dedicated treatment planning system, EYEPLAN, that integrates the standardized eye model. It is noteworthy to highlight that in EYEPLAN the eye model is based on geometric considerations and is only personalised for eye length and target volume definition. Specifically, as regards to the definition of the tumor volume, the geometrical 3D model of the eye globe is at first unfolded onto a 2D plane and the tumor base is drawn with respect to the tantalum markers position. During these procedures EYEPLAN allows for fundus photography registration with the unfolded plane using the macula and the optic disk as landmarks for position and scaling. However, this registration is affected by significant uncertainties, as the landmarks used for the registration are not patient specific but follow a geometrical model. Optic disk and macula positions within the EYEPLAN model are indeed defined according to a standardized eye model rather than a patient-specific personalization. For this reason, even though fusing the fundus photography to the eye model is possible in EYEPLAN, this is currently used in the clinical routine more as a qualitative evaluation of the target volume definition than a quantitative validation.

It is obvious that replacing the generic geometric eye model of EYEPLAN with a patient-specific MRI based eye model would be beneficial under multiple aspects. Nevertheless, it is important to consider the outstanding clinical success that the current workflow can achieve with local control rates well over 90% for several institutions adopting it. Therefore, before introducing novel technologies, an extensive validation process is required. As shown in previous studies, despite MR imaging having the potential to provide a personalized eye model, it systematically underestimates the tumor volume with respect to EYEPLAN and is not capable to capture particularly thin lesions (inferior to 3 mm) that are not visible on MRI images. It has also been shown that the differences between lesions delineated on MRI and built using EYEPLAN mostly stem from discrepancies in the definition of the base of the

tumor. This suggests that MRI is unable to capture the thinner infiltrations of the lesion in the retina and defining the target solely on MRI could potentially lead to tumor miss.

In order to create a complete patient-specific MR model, it is necessary to integrate additional information to accurately define the tumor volume; one of the most important source of this information is fundus imaging. This work of thesis is focused on this topic: integration and registration of fundus image to an MRI based eye model for improved target volume definition. Our aim is therefore two-fold. Firstly, we aim at improving the actual EYEPLAN unfolding method by including the fundus acquisition geometry for a more accurate fundus fusion. Then, we proposed a methodological framework from MRI and fundus integration, which aims at avoiding anatomical constraints towards a patient-specific image-based approach. This would potentially provide a personalized model with respect to the current clinical procedure, as implemented in the EYEPLAN TPS.

The methods developed in this work of thesis were tested on a dataset including 10 patients referred to the PSI for ocular proton therapy. The fundus photographs used in this work were acquired at the Hôpital Ophtalmique Jules-Gonin in Lausanne (Switzerland) with a Panoret-1000 machine. All patients underwent clips surgery and conventional treatment planning with EYEPLAN. In addition, the 10 patients underwent MRI scans (imaging included 3D volumetric T1-weigthed and T2-weighted sequences) under ethical approval. The key criteria for choosing the patient cohort was the complete visibility of the tumor, the optic disk and the macula in the fundus photography (Figure 1).

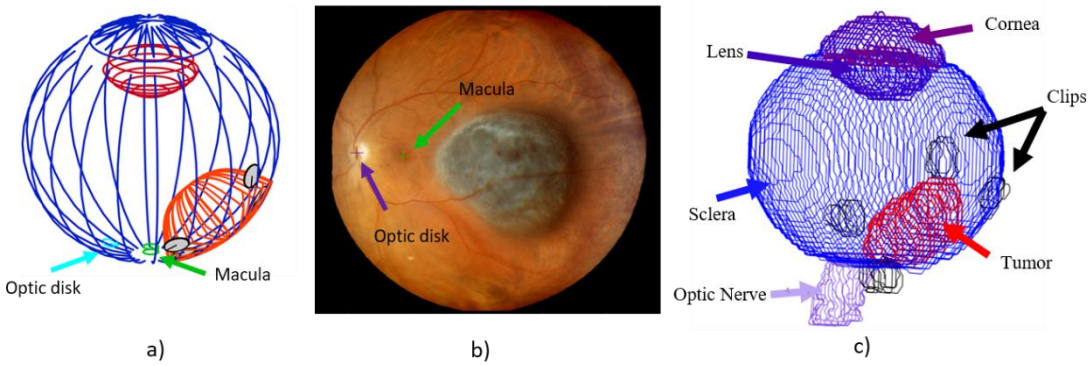

Figure 1- For the same patient are reported the EYEPLAN model (a), the fundus image (b) and the MRI model (c) obtained from the segmentation of the MRI volumes.

Modelling fundus image acquisition – the 'image center' method

In this section a novel unfolding method will be presented and compared to the traditional EYEPLAN one. In both the conventional and our proposed methods, the retinal unfolding is performed by having a point as the projection center and the radial distances on the bi-dimensional map correspond to the arc lengths on the 3D eye surface. However, this transformation does not guarantee point-to-point distance preservation along all the unfolded circumferences on the 3D spherical eye surface that do not pass across the projection center. This results in a distortion effect that is more prominent for unfolded structures that are further away from the projection center.

In EYEPLAN, regardless of patient specificity the macula is always considered as the projection center. Therefore, this method is macula position-dependent: if it is located in the fundus image periphery, the conventional EYEPLAN unfolding procedure may produce significant inconsistencies with the fundus, as the structures are more affected by this distortion. The method we proposed and tested considers the fundus image center as the center of projection. This procedure accounts for the variation of the image acquisition geometry caused by the operation with the aim of completely guaranteeing the tumor visibility. This approach leads to the generation of more truthful projections along with the reduction of contours' distortions. This is only a partial mitigation of the uncertainties affecting fundus photography acquisition but, nevertheless a significant one. The 'image center' method was evaluated by comparison with the traditional unfolding procedure embedded in EYEPLAN using the contours of the base in the geometrical eye model of EYEPLAN (see Figure 2). The resulting projection of the tumor base, either coming from EYEPLAN with or without center-of-projection or MRI with or without image-based macula selection was compared with manual delineation performed by a radiation oncologist directly on fundus photography. The metrics adopted to evaluate the similarity of contours, projected using both unfolding methods with the reference provided by manual delineation on fundus imaging, were Dice Similarity Coefficient (DSC), Jaccard Index, Overlap Index (OVL), Hausdorff distance (HD) and centroid distance (CD).

Overall, the above-mentioned metrics for the proposed approach improved compared to the EYPLAN's ones. On average, DSC, Jaccard index and OVL have improved by 5.5%, 8.7%

and 3.2%, respectively. The Centroid distance and the Hausdorff distance decreased of 1.08mm (corresponding to an improvement of 86.6%) and 0.11mm (corresponding to an improvement of 2.5%), respectively.

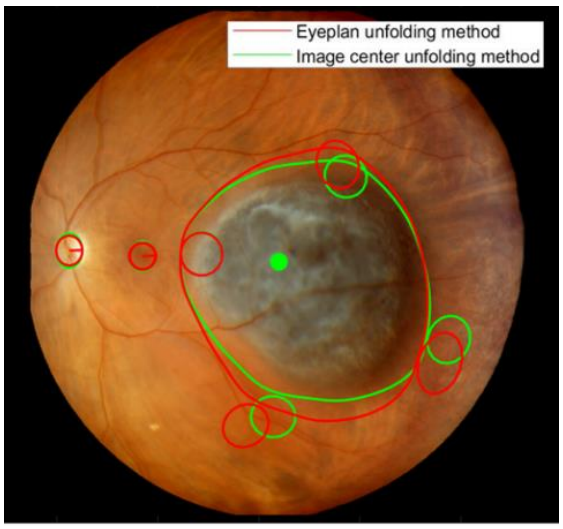

Figure 2-The projections of both methods are represented: the projection of the tumor according to the proposed method and the conventional EYEPLAN one is represented in green and in red, respectively.

Due to the better outcomes provided, the 'image center' unfolding method has been adopted as a standard one for the MRI part. Regardless of the unfolding method, it has to be considered that the registration process accuracy in EYEPLAN is mostly affected by uncertainties that derive from the approximate position of the macula and optic disk within the standardized eye model. Therefore, the adoption of the MRI model would guarantee an improved patient specificity with respect to the EYEPLAN model.

MRI ocular imaging and registration with fundus photography

Although MR imaging could provide a personalized model, it might be insufficient as a standalone tool for a proper tumor delineation and therefore, the combination with the higher resolution fundus photography is required. The fusion method developed in the work of thesis requires, much like EYEPLAN, the identification macula and optic disk in both the fundus photography and MRI scans.

The definition of the two landmarks could be establish within the MR model by means of the EYEPLAN approximations. The subsequent unfolding and registration of this MR model with the fundus can be performed, thus generating to what we refer as 'Geometric Approach'. Being the replica of how the actual TPS places macula and optic disk within the 3D model, this approach has been used for the comparison with our proposed method. However, the Geometric approach is still affected by several uncertainties stemming from the geometrical approximations, and because our purpose is the realization of a more accurate model, the landmarks have to be detected from the MR scans.

Even though both structures are not directly visible on MRI scans, they can be indirectly identified. The optic disk can be simply defined as the point at the intersection between the optic nerve head (visible in MR), i.e. the terminal part of the optic nerve that attaches to the eye globe, and the external sclera surface. On the other hand, the macula identification requires a greater effort.

This was already investigated by De Zanet et al (De Zanet, Ciller, Rudolph, & Maeder, 2010): in their approach, the macula position is restricted on the retina surface according to two anatomical constraints: (i) it is known from literature that the visual axis, i.e. the axis at which the macula belongs, deviates from the optical axis, i.e. the axis that passes through the lens center and the eye center, by an angle α of about $3.93 \pm 2.68°$ in the left eye and $3.91 \pm 2.73°$ in the right eye (Schaeffel, 2002); (ii) the macula to optic disk distance varies between 4.0 and 4.8 mm (De Silva, et al., 2006). As it can be noticed, the two constraints, however, present a high population-variability. For the implementation of their method, Zanet et al. have considered the population-based average values, thus neglecting the patient specificity.

In the proposed approach, the position of the macula within the MRI 3D eye model is established through an image-based approach which takes into account the patient-specific variability. The first step in the process is the selection of an area on the internal surface of the MRI eye model in a region located around the eye symmetry axis. Any point located in this region is considered as a potential macula candidate. By iteratively selecting all the macula candidates one at the time, a virtual image is generated with a 'pseudo-ray tracing' approach from both the T1 and T2 MR volumes, and subsequentially, each virtual image is compared with the real fundus photography through the mutual information (MI) metric.

The virtual image with the highest similarity value with respect to the fundus is chosen. This image corresponds to a specific macula candidate that is therefore defined as the macula for the specific patient. Nevertheless, the macula identification depends on the performance of the MI metric. Thus, we decided to evaluate the distance between the selected macula and the optic disk (i.e. second constraint), in order to: (i) provide a figure of merit able to evaluate the robustness of the MRI algorithm and (ii) improve the proposed procedure by including this as an anatomical constraint (in an average eye it should be between 4.0 mm and 4.8 mm) in the registration process. Specifically, after having selected the 'optimal macula' candidate, the algorithm evaluates if its position satisfies this constraint. If so, the macula is found, otherwise, the algorithm iteratively repeats this operation until the macula with the highest value of MI that satisfies the requirement is selected.

The same metrics adopted for the evaluation of the 'image center' method have been used for the comparison of the proposed 'image-based' method against the Geometric approach.

Overall, the proposed approach has been demonstrated to provide more accurate results compared to the Geometric method (Figure 3). Before the introduction of the second constraint, we observed an improvement in both the T1 and T2 approaches of 35.5% and 34.1%, respectively, and, after, 45% for T1 and 44% for T2 on the Hausdorff distance (HD) metric. On average, 2.8 iterations were required for T1-weigthed MRI and 3.9 iterations for T2-weighted MRI, suggesting that MI should be combined with the anatomical constraints. The introduction of the second constraint leads to better results and this is explained by the fact that the MI performance is significantly influenced by the type of pre-processing that is applied on both the fundus image and the virtual images. To evaluate this, three different pre-processing methods have been tested. We noticed that, with a heavier pre-processing applied to the fundus image, a better output is provided by MI algorithm.

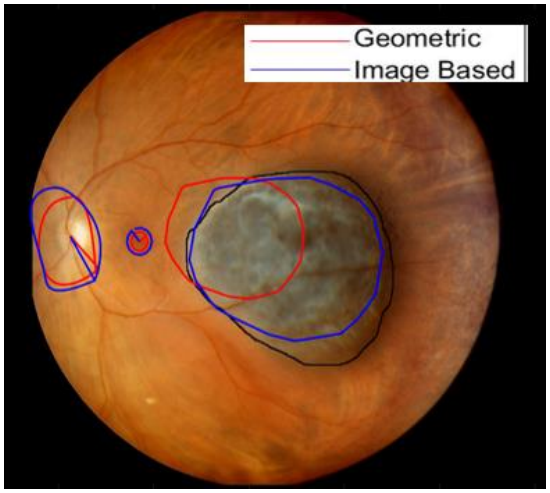

Figure 3- Projection of the tumor boundaries that come from the Geometric method (in red) and both the image-based methods (in blue). Also, the tumor delineation (in black) performed by a radiation oncologist is visible.

We expect a further improvement in the method when it will be applied on MRI volumes acquired with the use of contrast agents: an MRI campaign acquisition is ongoing at PSI and soon new data will be available. The use of the contrast agents will provide enhanced MRI volumes, in which (i) the accuracy in segmentation of the structures will be improved and (ii) the reduction of the noise will contribute to generate more consistent virtual images.

In conclusion, it has to be considered that the registration process is affected by uncertainties that derive from the approximate positioning of the macula and optic disk defined according to a standardized eye model. Despite EYEPLAN lacks in specificity, it is still able to generate a geometric ocular model capable of representing the structures within the eye with a certain precision and reliability. The use of MR shows promise for providing a personalized model of the eye, and for providing improved and patient specific anatomical information of the structures therein. Furthermore, the creation of the enhanced MR model, in which the tumor volume is generated by including the target outline delineated by the ophthalmologist on the fundus image, could provide a patient-specific eye model that one day could be adopted in a clipless workflow.

Sommario

I melanomi uveali sono relativamente rari (rappresentano il 3-5% di tutti i melanomi), ma altamente maligni, per i quali, fino al 1970, la scelta terapeutica primaria era l'enucleazione, ovvero la completa rimozione dell'occhio per evitare possibili metastasi. Negli ultimi decenni, tuttavia, le modalità di trattamento si sono spostate verso approcci più conservativi volti a preservare l'occhio ed evitare quindi la sua rimozione: la protonterapia e la brachiterapia sono oggi considerate lo standard clinico per il trattamento dei tumori oculari. La protonterapia oculare (OPT), grazie alla sua elevata selettività geometrica, è considerata la migliore scelta terapeutica per il trattamento dei tumori oculari. Il controllo locale del tumore che viene riportato da diversi istituti è pari al 90%.

Il trattamento con i protoni tuttavia richiede una procedura chirurgica in cui un determinato numero di marcatori radiopachi, realizzati in tantalio, vengono suturati sulla superficie della sclera. Le clip eseguono tre compiti principali: in primo luogo, vengono utilizzate per creare il modello geometrico dell'occhio del paziente; la superficie della sclera viene fittata attraverso le posizioni 3D delle clip acquisite mediante raggi X; in secondo luogo, servono come punti di riferimento per la definizione della base tumorale e quindi per la definizione del 'clinical target volume'(CTV), ovvero il volume che verrà irradiato mediante i protoni. Infine, le clip vengono utilizzate per posizionare e allineare correttamente il paziente nella sala di trattamento prima di procedere con l'irradiazione.

Tuttavia, la procedura chirurgica necessaria per la sutura delle clip è costosa, invasiva e abbastanza complicata da sopportare per il paziente.

Questo lavoro di tesi fa parte di un progetto di ricerca in corso tra il Politecnico di Milano e il Paul Scherrer Institut (Villigen, Svizzera) che ha l'obiettivo di realizzare un workflow nel quale non sia necessario l'utilizzo delle clip. Pertanto, per la realizzazione di questo ambizioso progetto, è necessario trovare delle alternative ad ogni compito che le clip eseguono: in particolare, l'utilizzo della risonanza magnetica (RM) per la realizzazione di un modello oculare comprendente le principali strutture dell'occhio e l'utilizzo di innovativi sistemi di eye tracking che permettano il corretto posizionamento e tracciamento dell'occhio prima e dopo il trattamento, sono già stati oggetto di studio e sono stati definiti come punti

chiave per la realizzazione di un ‘clipless workflow’. Questo lavoro di tesi ha l’obiettivo di generare un modello dell’occhio basato sull'anatomia specifica del paziente a partire dalla RM. In particolare, l'obiettivo principale consiste nel migliorare la definizione del clinical target volume (CTV) integrando alla risonanza magnetica le informazioni che provengono da un’altra modalità di imaging: la fotografia del fondo oculare (fundus photography).

L'immagine del fundus è una fotografia ad alta risoluzione della retina in grado di catturare la possibile presenza del tumore e le principali strutture oculari come macula, disco ottico e vasi sanguigni.

Come precedentemente descritto nel workflow convenzionale, la definizione del tumore è realizzata mediante le clip. Durante l’intervento chirurgico, il chirurgo, una volta suturate le clip, misura attentamente le distanze di ciascuna clip con il tumore e con le altre clip. Queste informazioni vengono, in fase di realizzazione del piano di trattamento, date in pasto ad EYEPLAN (treatment planning system), il quale genera un modello dell’occhio del paziente. È importante sottolineare che questo modello è un modello geometrico standard che viene ‘personalizzato’ adattandolo alla dimensione dell’occhio del paziente (misurata in fase diagnostica tramite ultrasuoni). Per la definizione del tumore, questo modello viene proiettato su un piano 2D e la base del tumore viene disegnata facendo riferimento alla posizione delle clip. Durante questa fase, EYEPLAN, permette la sovrapposizione dell’immagine del fundus tramite un’operazione di registrazione mediante due punti: macula e disco ottico. Tuttavia, poiché queste strutture sono definite all’interno del modello di EYEPLAN mediante approssimazioni geometriche piuttosto che paziente-specifiche, il processo presenta parecchie incertezze. Per questo motivo, nella pratica clinica l’informazione aggiuntiva fornita dal fundus è valutata solo qualitativamente.

È chiaro che la sostituzione del modello EYEPLAN, basato su considerazioni geometriche, con un modello paziente specifico basato su risonanza magnetica, porterebbe benefici sotto diversi aspetti. Tuttavia, è necessario considerare l'alto successo clinico che il workflow attuale possiede in cui il controllo del tumore superiore al 90%. La modificazione dell’attuale work flow può essere effettuata solo dopo un ampio protocollo di validazione del nuovo metodo. È già stato mostrato da precedenti studi che la risonanza magnetica è in grado di generare modelli paziente-specifici, ma che tuttavia, sottostima sistematicamente il volume del tumore rispetto a quello prodotto da EYEPLAN e, inoltre, non è in grado di rilevare

lesioni che siano più sottili di 3mm. È stato anche dimostrato come le differenze tra i due volumi tumorali dipendano principalmente da come la base del tumore viene definita. Questo suggerisce come la risonanza magnetica non sia in grado di fornire una corretta rappresentazione della base del tumore e che un workflow basato solamente su MR non può esistere.

È chiaro che per realizzare un modello completo e paziente specifico, è necessario introdurre informazioni addizionali che permettano una corretta definizione del volume tumorale e che la modalità di imaging più adatta a questo scopo è l'immagine del fundus oculare. Il nostro obiettivo è quindi duplice. In primo luogo, vogliamo migliorare l'attuale metodo che EYEPLAN utilizza per la proiezione dei contorni sul fundus (unfolding) e, in secondo luogo, proponiamo un metodo innovativo che integri i volumi di RM con la fotografia del fundus. Ciò fornirebbe potenzialmente un modello personalizzato rispetto a quello generato dall'attuale procedura clinica EYEPLAN.

I metodi sviluppati in questo lavoro di tesi sono stati testati su un set di 10 pazienti riferiti al PSI per essere sottoposti al trattamento con i protoni. Le immagini del fundus sono state acquisite presso l'Hôpital Ophtalmique Jules-Gonin di Losanna (Svizzera) con una Panoret-1000. Tutti i pazienti sono stati sottoposti all'impiantazione delle clip e pianificazione del trattamento convenzionale con EYEPLAN. Inoltre, sono state acquisite, per i 10 pazienti, le risonanze magnetiche (l'imaging include volumi 3D ottenuti con T1-w e T2-w) sotto approvazione etica. Il criterio chiave per la scelta della coorte di pazienti è stata la completa visibilità del tumore, del disco ottico e della macula nelle immagini del fundus (Figura 1).

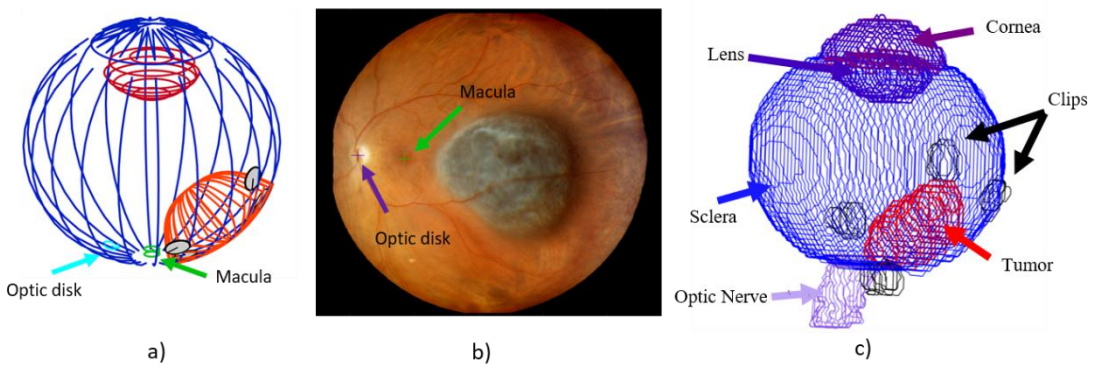

Figura 1-Per lo stesso paziente sono riportati: il modello EYEPLAN (a), l'immagine del fundus (b) e il modello RM ottenuto dalle segmentazioni dei volumi RM.

Variazione del campo di vista nelle immagini del fundus - il metodo "image center"

In questa sezione verrà presentato un nuovo metodo di unfolding e successivamente confrontato con quello tradizionale di EYEPLAN. Sia nel metodo convenzionale che in quello proposto l'unfolding delle strutture sulla retina viene eseguito avendo un punto che funge da centro di proiezione: le distanze radiali sul piano bidimensionale corrispondono alle lunghezze calcolate sulla superficie sferica dell'occhio 3D. Poiché ogni lunghezza è calcolata tramite un integrale di linea tra il centro di proiezione e qualsiasi punto che deve essere proiettato, questo metodo preserva le distanze lungo le circonferenze massime che attraversano il centro di proiezione. Tuttavia, le distanze tangenziali nel piano 2D sono distorte ed è chiaro che l'entità della distorsione è maggiore più ci si allontana del centro di proiezione. In EYEPLAN, le operazioni di unfolding vengono effettuate sempre dalla macula dato che questa è sempre considerata come centro di proiezione. Tuttavia, una volta che i contorni sono stati registrati con il fundus, l'entità della distorsione è macula-dipendente: se essa è localizzata alla periferia del fundus, le strutture sono maggiormente affette da distorsione e di conseguenza, il metodo convenzionale può produrre significative incoerenze con l'immagine del fundus.

Il metodo che proponiamo considera il centro dell'immagine del fundus come centro di proiezione. Questo permette di considerare la variazione della geometria con cui l'immagine del fundus è stata acquisita (con l'obiettivo di garantire la completa visibilità del tumore). Questo approccio porta alla generazione di proiezioni più veritiere attraverso la riduzione delle distorsioni dei contorni. Il metodo "image center" è stato valutato confrontandolo con la tradizionale procedura di unfolding incorporata in EYEPLAN (Figura 2).

La proiezione della base tumorale, con l'utilizzo o senza del centro di proiezione è stata confrontata con la delineazione manuale eseguita da un oncologo direttamente sull'immagine del fundus. Le metriche adottate per la valutazione della somiglianza dei contorni generati utilizzando entrambi i metodi di unfolding con la segmentazione effettuata dall'oncologo sono: Coefficiente di Similarità Dice (DSC), Indice di Jaccard, Indice di Overlap (OVL), Distanza di Hausdorff (HD) e distanza tra i centroidi (CD).

In media, DSC, indice di Jaccard e OVL sono migliorati rispettivamente del 5,5%, 8,7% e 3,2%. La distanza tra i centroidi e la distanza di Hausdorff sono diminuite rispettivamente di 1,08 mm (corrispondente a un miglioramento dell'86,6%) e di 0,11 mm (corrispondente a un miglioramento del 2,5%). Avendo dimostrato la superiorità del metodo introdotto, esso è stato adottato come metodo standard per le operazioni di unfolding per le successive parti.

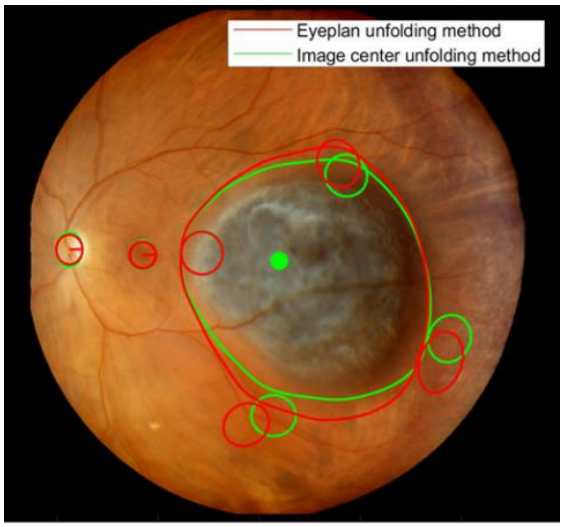

Figura 2-Sono riportate le proiezioni delle principali strutture per entrambi i metodi: in verde le proiezioni generate con il metodo 'image center' e in rosso quelle generate dal metodo convenzionale di EYEPLAN.

È importante sottolineare che, indifferentemente dal metodo di unfolding considerato, l'accuratezza del processo di registrazione effettuata da EYEPLAN è affetta da molteplici incertezze che derivano dalle approssimazioni, basate su un modello standard, adottate per il posizionamento di macula e disco ottico nel modello 3D. Sicuramente l'introduzione della risonanza magnetica garantirà un aumento della specificità rispetto al modello EYEPLAN.

Risonanza magnetica oculare e registrazione con l’immagine del fundus

Nonostante l’imaging RM sia in grado di fornire informazioni paziente specifiche, esso non è sufficiente per una completa descrizione del tumore e la combinazione con un’altra modalità di imaging è necessaria. Per permettere l’integrazione dell’immagine del fundus, come in EYEPLAN, macula e disco ottico devono essere identificati nei volumi RM.

Tuttavia, la loro definizione all’interno del modello potrebbe essere effettuata utilizzando le approssimazioni di EYEPLAN. Le successive operazioni di unfolding e di registrazione di questo modello MRI con l’immagine del fundus possono essere effettuate. All’interno del nostro lavoro di tesi, questo approccio prende il nome di ‘Approccio Geometrico’. Dal momento che quest'ultimo è segnale di come l'attuale TPS (treatment planning system) inserisca macula e disco ottico nel modello, l'approccio geometrico verrà, a buona ragione, utilizzato come metodo di paragone per confrontare e valutare il metodo che verrà proposto nella seguente sezione. Essendo macula e disco ottico affetti da numerose incertezze dato che la loro posizione è stabilita mediante approssimazioni geometriche, per la realizzazione di un modello più accurato e paziente specifico, è necessario che questi due punti di riferimento vengano rilevati a partire dai volumi MR.

Sebbene macula e disco ottico non siano direttamente visibili nelle scansioni RM, essi possono essere identificati indirettamente. Il disco ottico è definito come l’'intersezione tra la testa del nervo ottico (visibile in MR), cioè la parte terminale del nervo ottico che si attacca al globo oculare, e la superficie esterna della sclera. D'altra parte, l'identificazione della macula richiede uno sforzo maggiore.

Questo è già stato studiato da De Zanet et al. (De Zanet, Ciller, Rudolph, & Maeder, 2010): nel loro approccio, la posizione della macula viene definita sulla superficie della retina in base a due vincoli anatomici: (i) è noto dalla letteratura che l'asse visivo, cioè l'asse a cui appartiene la macula, si discosta dall'asse ottico, cioè l'asse che passa attraverso il centro della lente e il centro dell'occhio, di un angolo α di circa $3{,}93 \pm 2{,}68°$ nell'occhio sinistro e $3{,}91 \pm 2{,}73°$ nell'occhio destro (Schaeffel, 2002). (ii) La distanza tra macula e disco ottico varia tra 4,0 e 4,8 mm (De Silva, et al., 2006). Come si può notare, i due vincoli presentano tuttavia un'alta variabilità: per l'implementazione del loro metodo, Zanet et al. hanno deciso

di considerare solamente i valori medi dei due vincoli eliminando così la variabilità tra pazienti.

Nell'approccio proposto, la posizione della macula all'interno del modello oculare RM 3D viene stabilita attraverso un approccio image-based nel quale è mantenuta l'alta variabilità. In primo luogo, viene selezionata un'area sulla superficie interna della sclera del modello RM in una regione situata attorno all'asse ottico. Poiché la macula può venirsi a trovare in qualsiasi punto all'interno di questa regione, ogni punto è considerato come una potenziale macula. Per ciascuna candidata macula, viene generata un'immagine virtuale mediante una tecnica di "pseudo-ray tracing" sia dai volumi MR T1 che T2, e successivamente, ogni immagine virtuale viene confrontata con la reale immagine del fundus attraverso l'algoritmo di mutua informazione (MI). L'immagine virtuale che presenta la più alta similarità con il fundus viene selezionata, e la macula che ha generato tale immagine virtuale viene indentificata come 'macula ottima'.

Tuttavia, poiché l'identificazione della macula ottima è altamente dipendente dalle prestazioni della mutua informazione, abbiamo deciso di utilizzare la distanza tra la macula selezionata e il disco ottico al fine di: (i) fornire una figura di merito in grado di valutare la solidità dell'algoritmo MRI e (ii) migliorare la procedura proposta includendo questo requisito come un vincolo anatomico (in un occhio medio, la distanza dovrebbe essere compresa tra 4,0 mm e 4,8 mm). In particolare, dopo aver selezionato il candidato "macula ottima", l'algoritmo valuta se la sua posizione soddisfa questo vincolo. In tal caso, la macula è stata trovata, altrimenti l'algoritmo scarta questa macula e ripete iterativamente le precedenti operazioni fino a quando la macula con più alto valore di MI soddisfa il nuovo vincolo.

Le stesse metriche adottate per la valutazione del metodo "image center" sono state utilizzate per il confronto del metodo "image-based" con il metodo Geometrico (Figura 3).

Complessivamente, è stato dimostrato che il nuovo metodo è in grado di produrre risultati più accurati rispetto all'approccio geometrico. Prima dell'introduzione del secondo vincolo, abbiamo osservato un miglioramento nei metodi image-based T1 e T2 rispettivamente del 35,5% e del 34,1%, e, dopo l'introduzione del vincolo, del 45% per T1 e del 44% per T2 nella distanza di Hausdorff (HD). In media, sono state necessarie 2,8 iterazioni per T1 e 3,9 iterazioni per T2, suggerendo che la mutua informazione non è sufficientemente robusta e

che l'introduzione di una metrica per la sua valutazione è necessaria. È stato osservato come le prestazioni della MI siano significativamente influenzate dal tipo di pre-processing che viene applicato sia sull'immagine del fundus che sulle immagini virtuali. Sono stati testati tre diversi metodi di pre-processing; abbiamo notato come l'incremento della pesantezza nei metodi di pre-processing porta a risultati più consistenti dell'algoritmo di MI. Questo in parte è giustificato dal fatto che l'immagine del fundus ha un contenuto informativo superiore rispetto alle immagini virtuali e che la rimozione di particolari, come i vasi sanguigni e il colore della retina, sia in grado di aumentare la similarità con le immagini virtuali.

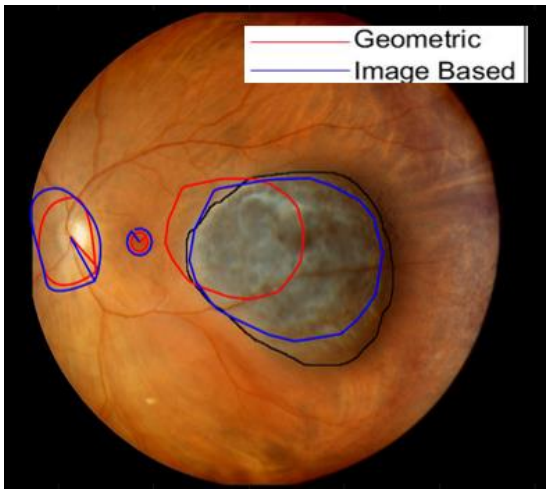

Figura 3-Proiezione del tumore generato mediante l'approccio Geometrico (in rosso) e tramite il metodo 'Image-based' (in blu). Anche la delineazione del tumore (in nero) eseguita da un oncologo è visibile.

Sicuramente il metodo produrrà risultati ancora migliori quando verrà impiegato su volumi RM ottenuti con l'utilizzo di agenti di contrasto: attualmente al PSI è in corso una campagna di acquisizione di RM con l'obiettivo di estendere il dataset disponibile e in cui si fa utilizzo di agenti d contrasto. L'introduzione del contrasto permetterà (i) una migliore visibilità delle strutture e (ii) la generazione di immagini virtuali meno rumorose.

Per quanto riguarda il metodo "image center", possiamo affermare che l'introduzione del FOV nel processo di unfolding porta alla generazione di proiezioni meno distorte. La modifica del volume tumorale, su suggerimento dell'immagine del fundus, può ora essere eseguita con meno incertezze. Tuttavia, si deve considerare che il processo di registrazione è influenzato da incertezze che derivano dal posizionamento approssimativo della macula e del disco ottico definiti secondo un modello oculare standardizzato. Nonostante EYEPLAN manchi di specificità, è in grado di generare un modello capace di rappresentare le strutture

oculari con una certa precisione e affidabilità. Tuttavia, l'uso della RM mostra risultati promettenti per la realizzazione di un modello personalizzato nel quale le strutture anatomiche al suo interno sono paziente-specifiche. Inoltre, con il nostro metodo è possibile generare il volume tumorale includendo il profilo del target definito dall'oftalmologo sull'immagine del fundus. Il modello così ottenuto potrebbe, un giorno, essere utilizzato in un workflow in cui l'utilizzo delle clip non è più necessario.

1 Introduction

1.1 Proton therapy

The use of proton beams for tumour treatment was proposed by Robert Wilson in 1946, with the first irradiations performed in 1954 at the Berkley Radiation Laboratory (BRL) for treating the pituitary gland in patients affected by metastasis of breast tumours.

This therapy has been consolidated during the years and, up to now, several proton-therapy centres are in operation worldwide and as many are under construction. The reason for the proliferation of proton-therapy centres is the potential advantages it presents with respect to conventional radiation therapy using photons: high geometrical selectivity allowing uniform dose distribution to the target while spearing surrounding healthy tissues, along with higher radiobiological effectiveness. (Durante, Orecchia, & Loeffler, 2017) (De Vera, Abril, & Garcia-Molina, 2018)

The advantage of proton therapy can be appreciated in the depth-dose curves of single beam irradiation with protons and X-rays in water (Figure 4).

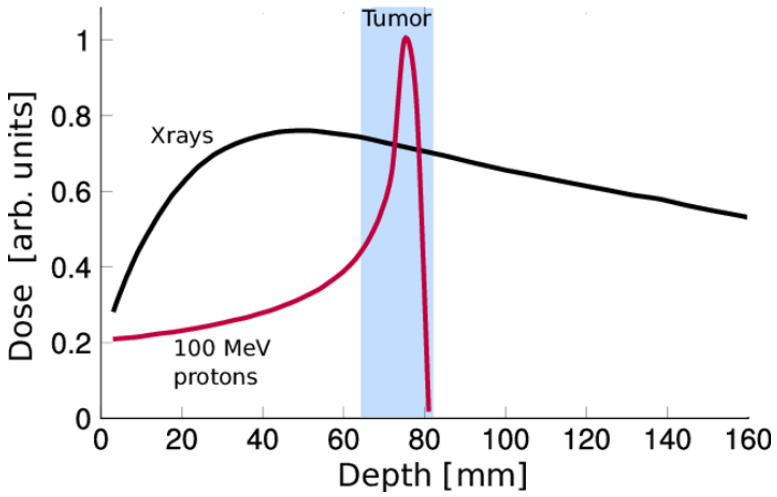

Figure 4-Bragg peak. Depth dose for X-Rays and protons.

X-ray and protons show substantial differences in their interaction with matter along the beam path due to their different physical properties.

Photons have no mass and no charge and when travelling through human tissues they deliver dose throughout their path. The highest dose is deposited at the beam entrance in the body (0.5cm - 3cm) typically in proximity of the patient's skin. Then, along its path dose deposition drops exponentially. As the majority of tumors treated with radiation therapy are so-called deep-seated, i.e. deeply located in internal organs, different entrance paths are combined to achieve a dose escalation at the target location. This technique is commonly known as Intensity Modulate Radiation Therapy (IMRT) and allows for optimal conformity of the dose distribution to the clinical target. Nevertheless, given the physical properties of the interaction of photons and human tissues, a significant amount of dose is going to be delivered at the beam entrance and in the tissues surrounding the tumors.

Conversely, protons are charged particles. As such, the amount of dose that is deposited at the beam entrance in the human body is quite low, with a maximum dose deposition reached at the so-called Bragg Peak. The depth at which the Bragg Peak occurs is a function of the beam energy at the entrance. In addition, after this burst of energy the beam stops, resulting in virtually no radiation to the tissue beyond the target or no "exit dose".

The complete target coverage, in proton therapy, is performed by using a series of Bragg peaks placed at different depths whose sum gives a uniform depth-dose distribution, which is called spread-out of Bragg peak (SOBP). The widen of the treatment depth range with a uniform dose is depicted in Figure 5.

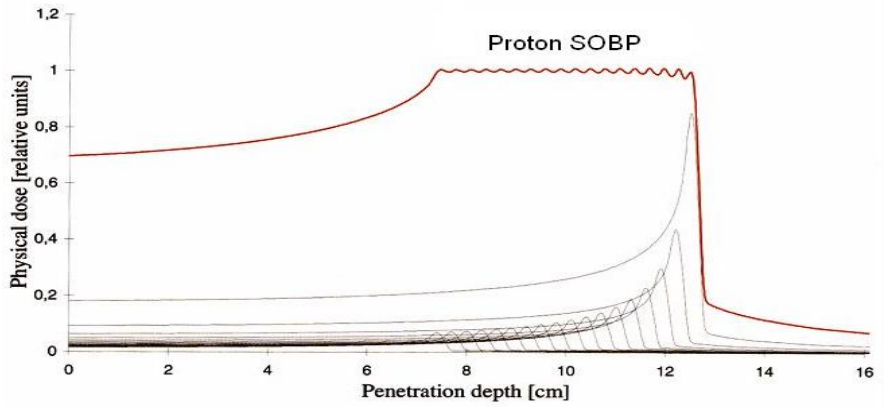

Figure 5- Depth dose distributions for a spread out bragg peak (SOBP)

The behaviour of the different radiations can be described by the Linear Energy Transfer (LET). It represents the amount of energy that an ionizing particle transfers to the material traversed per unit distance and can be expressed by the following formula:

$$LET = \frac{dE}{dx}$$

Where dE is the energy loss of the charged particle due to electronic collisions while traversing a distance dx. It is clear that the proton energy deposition compared to X-rays is higher when protons are close to the Bragg peak.

Figure 1 shows that, compared to radiotherapy, proton-therapy minimizes the dose to healthy tissues along the beam path preceding the tumour target (proximal to the Bragg peak) and gives an almost zero dose to the tissues at higher depths (*distal* to the Bragg peak). Thus, a better sparing of the healthy tissues surrounding the tumour (organs-at-risk) in combination with improved dose distribution conformity to the target is achievable by using protons instead of photons. Figure 6 shows a treatment plan with photons (on the left) and proton (on the right) for a head and neck tumour, showing more conformal isodose curves on the target for proton therapy.

Along with the geometrical benefit, a brief mention should be given to the biological advantage of using protons instead of photons. The *relative biological effectiveness (RBE) is* a quantity used for expressing the biological effects of one particular radiation technique, in terms of the response of different cellular cultures to radiation fields, with respect to a reference.

$$RBE = \frac{D}{Dref}$$

D is the absorbed dose necessary to produce a given effect (e.g., a given survival rate of cells) and Dref is the absorbed dose from the reference radiation field generating the same

biological effect. Commonly, even if there is no universal agreement about this topic, the reference radiation field is constituted by 150 kV X-rays or by gamma rays from the 60Co decay (Merle, Arthur, Eugene, & Donn, 1960).

In other words, the RBE is defined as the ratio of the doses required by two different radiation fields to generate the same biological effect. The RBE for proton is 1 in the proximal part of the Bragg peak, while it increases in the distal part where protons are characterized by higher linear energy transfer (LET) values.

Traditionally an RBE value of 1.1 is assigned to proton beam and applied to all tissues. Thus, protons have a slightly higher biological effectiveness than X-rays, meaning that the same biological effect is achieved with less dose than the one required by conventional radiotherapy. Heavy ions, like Carbon ions, are characterized by higher RBE values that vary from tissue to tissue: this is due to oxygen enhancement (the higher the oxygen content in the irradiated tissue is, the higher is its radio-sensitivity of that tissue) and higher average LET values.

It is important to highlight that radiation therapy is usually divided or "fractionated" over a treatment course. When the total dose of radiation is divided into smaller doses over a period of several days the destruction of malignant cells is maximised while the damage to healthy tissues is minimized.

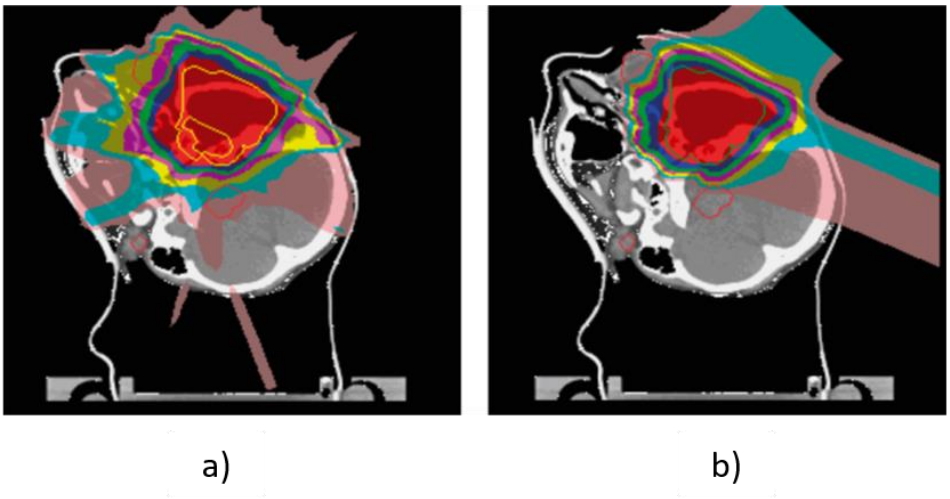

Figure 6-Lleft side (a) IMRT treatment plan simulation in which the dose bath is underlined with respect to the proton treatment plan, right side (b)

1.2 Ocular Tumors Overview

The first treatment of proton irradiation for ocular melanoma was performed at the Massachusetts Ear and Ear Infirmary (MEEI) in 1975.

Ocular tumors are rather uncommon but very aggressive malignancies that can lead to compromise vision and develop into metastases. Among intraocular tumors, the most common are ocular melanoma (OM) and retinoblastoma, for adults and children respectively.

According to a study by the American Cancer Society the ocular melanoma annual occurrence is expected to be between four and seven cases per million people in United States, Canada and Europe, whilst Data from the Third National Cancer Survey suggest an annual incidence between 9 and 11 cases per million for retinoblastoma.

In 82.5% of the cases, ocular melanomas arise in the uvea, i.e. a pigmented layer between sclera and cornea. The uvea consists of three bodies: iris, ciliary body and choroid. 90% of the uveal malignancies occur in the choroid, 5-10% in the ciliary body and only 3% affect the iris. (Damato, 2004). Less frequent site of origin of intraocular tumours is the conjunctiva comprising about 5% of all melanomas affecting the ocular region (Jovanovic, et al., 2013).

Incidence of ocular melanoma is increasing with age, with a peak in the seventh and eighth decade of life (McLaughlin, et al., 2005).

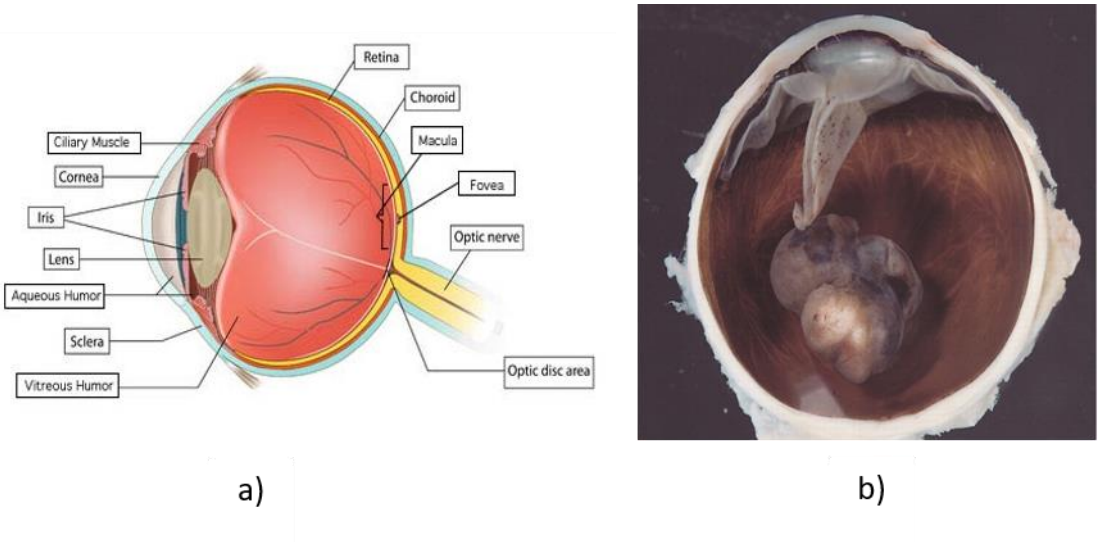

Figure 7- (a) Anatomy of the eye. (b) posterior malignant choroidal tumor.

Compared to uveal melanoma (UM), which incidence has remained constant over the last three decades, conjunctival melanoma has shown an increase in frequency, especially among white men, older than 60 (Yu, Hu, McCormick, & Finger, 2003). Survival rate is significantly lower when tumor diameter exceeds 15 mm at the time of diagnosis. Furthermore, the tumor extension to posterior ocular structures such as optic disc or fovea strongly compromises visual acuity preservation. So, the earlier diagnosed the greater the chances are to identify the lesion, before excessive growth in size or proliferation to critical structures for vision occurred (Damato B, 2001).

Diagnosis and management of intraocular tumor have been subjected to a significant change in the last decades: the conventional therapeutic choice was enucleation till 1960 (Tataru & Pop, 2012). The eye removal guaranteed the completely exclusion of the tumor, but the recurrence rate was quite high due to a non-complete removal of the optic disk or to the possible presence of metastasis spread in the body. Furthermore, this technique was wrongly applied in the 20% of the cases due to the lack of a proper diagnostic procedures. In the last decades, treatment modalities have improved moving toward a more conservative way to avoid eye enucleation and loss of sight, parallelly to improved tumour diagnosis, with optical coherence tomography (OCT), computed tomography (CT), eye ultrasounds, intraocular angiography considered as a standard of diagnostic imaging. Nowadays the percentage of diagnostic error for ocular melanoma is less than 1% as reported in a study that included 413

patients carried out by the Collaborative Ocular Melanoma Study (COMS) (C.O.M.S., 1990).

The results of a total of 7516 UM patients over the 40 years study period (1973 to 2012) have been published: a significant temporal change in UM treatment approaches has occurred over the last 40 years (Figure 8). The current study observed a 69.4% decrease in surgery or enucleation as primary treatment with a corresponding 62% increase in the use of eye-preserving primary radiotherapy.

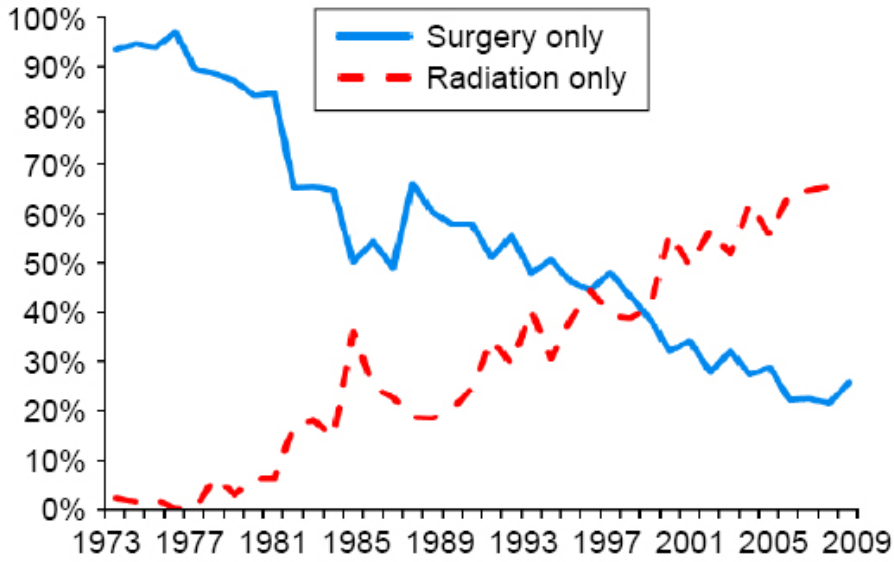

Figure 8-Temporal changes in the management of 7.516 uveal melanoma patients from the Surveillance, Epidemiology, and End Results (SEER) database, 1973-2012.

In addition to avoiding enucleation and preserving vision in up to 43% of patients undergoing primary radiotherapy for UM, a significant survival advantage in patients receiving radiotherapy compared to surgical treatment was also observed (15.4±0.4 years vs 13.6±0.3 years) (Mahendraraj, Lau, Lee, & Chamberlain, 2016).

Among different treatment modalities, primary radiation therapy has proved to be a valid alternative to enucleation: external beam radiation therapy, proton therapy and brachytherapy are nowadays considered the clinical standards (Sing, Turell, & BA, 2011). In all these cases, a treatment planning procedure, in which a patient-specific model is created relying on dedicated imaging modalities, is typically performed before treatment delivery. The following section delves into these different treatment modalities.

1.2.1 Stereotactic radiation therapy

Stereotactic radiation therapy (SRT) consists in delivering a high dose of ionizing radiation to the target volume with small doses to the surrounding tissues in a limited number of fractions (Dieckmann, et al., 2004). Treatment planning is based on a multimodal image registration of CT and MRI images. Gadolinium enhancement is employed during the MRI in order to distinguish the gross tumor volume (GTV) from the subretinal fluid. After the registration (i.e. fusion) of different image modalities, the target volume is identified through manual segmentation and a safety margin of 1-2mm is added in the threated volume. To avoid patient's movement during treatment, an immobilization procedure is typically performed with non-invasive rigid thermoplastic mask and bite block, which are personalized and prepared for each patient. The mask is fixed with screws to the couch. However, head fixation alone does not prevent eye movements that can affect the repeatability of the treatment during the different fractions. In order to solve this problem, active eye immobilization techniques are used: the patient is asked to look at a blinking fixation light with the diseased eye or the contralateral eye. The eye is monitored by an eye tracking device that follows the pupil movement. If the displacement exceeds the threshold, the beam delivery is automatically interrupted. SRT treatments of UM are performed by using a linear accelerator and the total dose of 50 Gy is usually delivered in five fractions over a period of 5 days (Muller, et al., 2005).

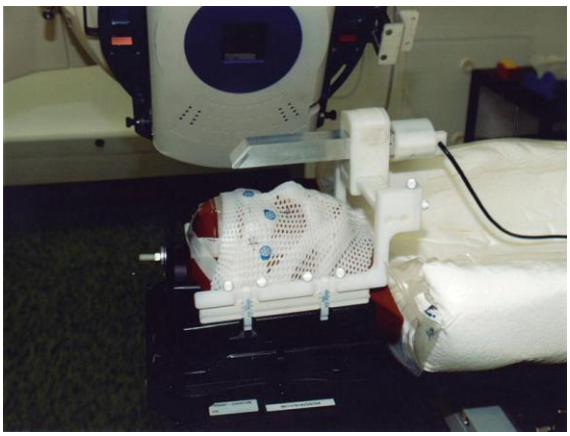

Figure 9-Stereotactic radiosurgery set up: ocular fixation system attached to the head mask and the rotating gantry in fractionated stereotactic radiotherapy.

1.2.2 Brachytherapy

Brachytherapy treatment consists in placing, close to the target volume, radioactive seeds that deliver a highly concentrated radiation dose (see Figure 10). The radiation sources used for brachytherapy come in the form of small "rice-sized" radioactive seeds. These seeds are attached within a gold or steel bowl called a plaque. Placement of the plaque is performed during a surgical procedure in which the surgeon attaches the plaque to the outer surface of the eye, covering the base of the intraocular tumor. The dose of radiation delivered to the target is determined by the type, number and strength of the seeds used and length of time of the implant. The first successful treatment of uveal melanoma with brachytherapy was performed by Deutschmann in Hamburg in 1915 using mesothorium (radium-218) capsules in fractionated doses (Bechrakis, Blatsios, & Hass, 2015).

Various types of eye plaques are available nowadays clinically e.g. iodine-125, palladium-103 and ruthenium-106 (Finger, Berson, & Szechter, 2002). The different radionuclides present different properties and dose distribution inside the eye. Thus, the choice of the radionuclide is driven by the tumor size and shape and the position in which the plaque can be sutured to the eye. A brief comparison between 125I and 106Ru dose distribution is depicted in Figure 10.

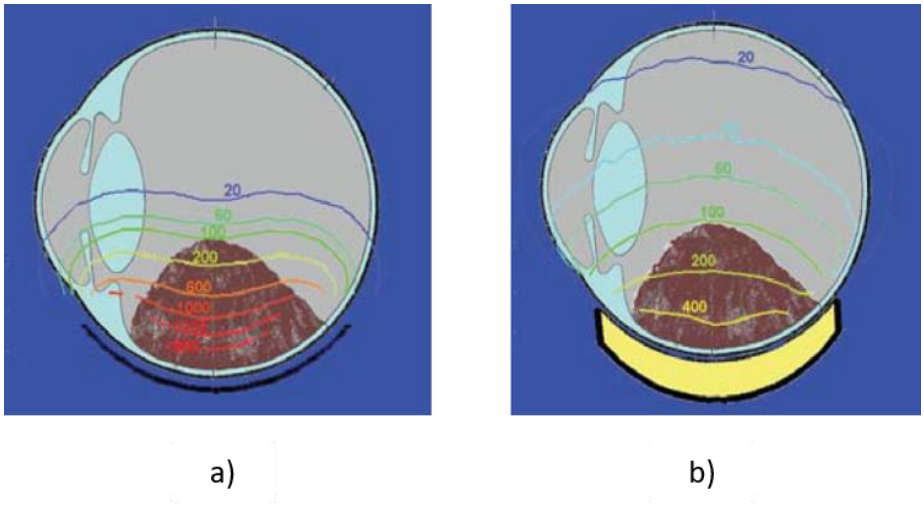

Figure 10- Dose distributions of Ruthenium-106 (a) and Iodine-125 (b) plaques for ocular brachytherapy.

106RU is beta emitter characterized by a very steep dose gradient and by a maximal energy of 3.53Mev. The peculiarity of 106RU is that the dose is concentrated to the tumor base and the effects on the contralateral structures are minimized and is therefore an appropriate choice for low thickness targets (up to 5 mm). The typical dose at the tumor apex is 120-160Gy. On the Contrary, 125I is a gamma emitter with mean energy 27-35KeV and present a more gradual dose fall-off. It is a proper choice for higher tumors, in the range of 8 to 12 mm with a prescribed dose of 85Gy at the apex (Laube, Fluhs, Kessler, Fiscia, & Bornfeld, 2007). The most common side-effect of brachytherapy is radiation-induced retinopathy which occurs in 21.5% to 62.8% of the cases according to different studies (Kellner, Bornfeld, & Foerster, 1993) (Gundzu & al., 1999).

1.2.3 Proton therapy

Proton therapy, thanks to its high geometrical selectivity and sharp dose fall-off, presents many advantages for eye treatment, especially for uveal melanomas which are often limited in size and in close proximity of organs pivotal for vision. The local tumor control, reported by several different institutions, is as high as 98% in combination with good outcomes in terms of vision preservation (Gragoudas E. , 2006). Due to its advantages ocular proton therapy has spread more than other treatment modalities in the last decades. Although studies have demonstrated generally better outcomes, ocular proton therapy can be difficult to access because is a quite expensive treatment compared to the others and due to the limited centers (Gragoudas E. , 2006).

Nowadays more than 20 centers worldwide are offering OPT (ocular proton therapy) treatment to patients affected by intraocular tumours, and other facilities are being under construction. In the following, the workflow of ocular proton therapy is presented.

1.3 Ocular Proton Therapy

The actual workflow for an ocular proton therapy treatment can be resumed with the following flowchart.

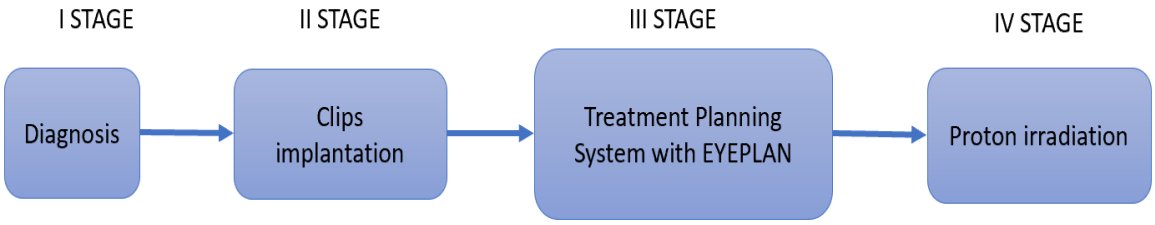

It can be divided into 4 stages: the first one corresponds to the diagnosis phase in which the presence of an eventual ocular tumor is evaluated by an ophthalmologist with different diagnostic exams (fundus photography, angiography, ultrasonography…). After the tumor identification, if the patient is referred to OPT, the second stage takes place. In this phase the patient undergoes a surgical intervention in which a number (3 to 6) of tantalum markers is implanted on the sclera surface around the tumor boundaries. The clips serve as a reference in the third stage, in which the treatment planning system EYEPLAN models the patient eye with a geometrical model. The tumor base is defined according to the clip-to-clip and clip-to-tumor distances and the tumor height and apex position are retrieved from A-mode ultrasound measurements. Embedded in this eye globe model, there are several organs such as the macula, optic disk and lens, whose positions and shape are predefined according to a standardized eye model. In this phase dose calculation between different plans is performed and compared by means of DVH (dose-volume histograms). The goal is to select the optimal gaze angle and the collimator aperture to guarantee robust target coverage and minimize the dose that each critical ocular structure will receive. The last stage is the irradiation: the patient is immobilized using a thermoplastic mask and bite block fixed to the chair and, by using the clips as a guidance, the patient is positioned correctly with respect to the isocenter of the treatment room. Once the patient is correctly positioned, is asked to look at a given gaze direction, as defined during treatment planning phase. Usually, a uveal melanoma requires 60 Gy delivered in four subsequent fractions.

1.3.1 Beamline characteristics

All OPT clinical facilities use accelerators constructed specifically for therapeutic purposes, typically isochronous cyclotrons. The maximum energies used for treating eyes are in the range 60-75MeV corresponding to depth of penetration in the eye tissue of 30 to 36mm. To exploit the physical properties of the proton beam extracted from the accelerator, conformity to the tumor volume is necessary and is typically achieved by passive or active system present along the beam line. For eyes treatment, a fixed beam line in combination to passive systems for beam shaping are used.

Firstly, the range shifter is used to decrease the energy of the beam thus avoiding exceeding the defined energy for the specific treatment. It consists of a number of fixed thickness stopping material or absorbers positioned in series along the beamline. By selecting a specific combination of range shifters, the total thickness is changed and, as a result, the distal position of the SOBP to lower or higher depths.

Secondly, the scatter foils are used to widen the beam (widened) through nuclear scattering. A thin lead foil (0.5 mm in thickness) is placed perpendicularly to the beam axis. The angular distribution of the scattered beam in the beam direction can be approximated by a Gaussian curve. A second scatter foil made of lead is used to guarantee uniformity of the beam shape on the trans axial plane.

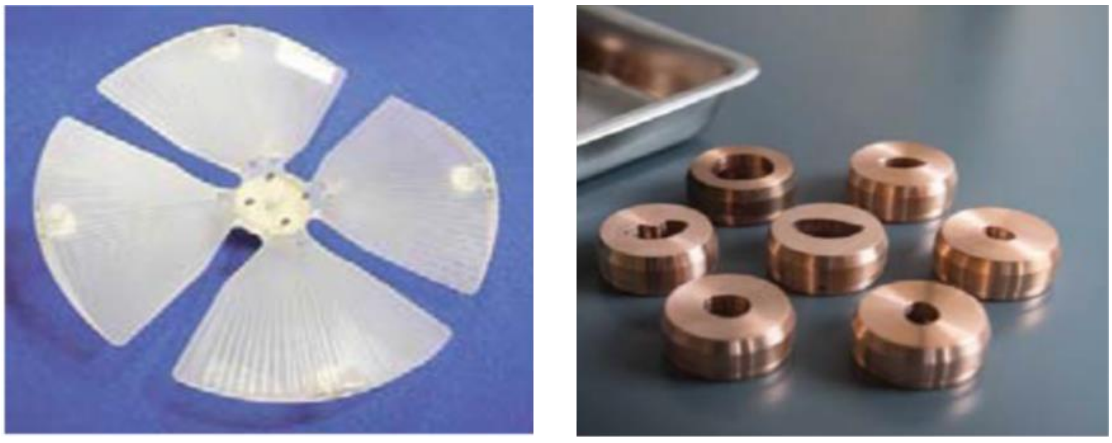

Figure 11-Panel (a) shows a modulator wheel: all steps of the wheel results in different dose deposition depths of protons. Panel (b) depicts a collimator. It is manufactured so that its aperture follows the tumor profile.

The second element is thicker on the beam axis to maximize nuclear scattering where the beam is more intense whereas the first is thinner, as it has to absorb a low amount of energy and to minimize the production of secondary neutrons.

The third element is the so-called modulator wheel or range modulator. The modulator wheel is a helix rotating device, whose blades have a different thickness. Hence by inserting the rotating blades to the beam stream, a variable amount of energy is absorbed depending on the thickness that the beam goes through at any moment thus obtaining a series of Bragg peaks placed at different depths whose sum gives rise to the Spread Out Bragg Peak. It should be noted that the dose in the proximal part of the SOBP increases, since also the proximal doses of the single Bragg peaks add. The last beam-shaping element is a patient-specific collimator that conforms the dose to the target volume shape in the trans axial plane. The collimator is made of brass and an aperture is carved out to the patient-specific shape of the target. As a result, protons are stopped wherever they encounter the collimator and are free to travel to the target volume through its aperture.

The main reason behind the use of passive beam scattering system is the limited dimensions of intraocular tumours and their proximity to functionally important structures in an organ of limited size such as the eye. Combining passive beam collimation and modulation allows to achieve sharper dose lateral dose gradient (penumbrae) and proximal and distal fall-off with respect to active system where the beam is driven magnetically. Ten OPT centers reported mean penumbrae fall-offs (80%-20%) and distal fall-offs (90%-10%) in water from 0.9 to 1.9 mm and 0.7 to 2.3 mm, for passive and active systems respectively (Kacperek A. , 2012). Due to the presence of radiosensitive structures in close proximity to the target, such as macula and optic disk, the steeper dose gradient possible is required in OPT.

1.3.2 Treatment Room

OPT centers typically feature fixed horizontal beam lines. Ocular proton therapy treatments are isocentric meaning that the position of the beam is fixed with respect to patient positioning device. The treatment isocenter is found along the beam axis at, typically, 70 mm from the surface of the aperture of the collimator. During treatment the patient is seated

on a treatment chair that can move translationally with a precision of ± 0.2mm along three directions relative to the isocenter: lateral, vertical and longitudinal. The patient is immobilized using a rigid thermoplastic mask and bite fixed to the chair frame. Treatment room for OPT are equipped with X-rays imaging system necessary for acquiring planning images and guidance prior irradiation. Depending on the facility, X-ray panels can be retracted laterally or vertically into a specific shielded housing in order to minimize neutron exposure during the treatment (Kacperek A. , 2012). A red-light emitting diode is mounted on a rotating stalk placed at the end of the beamline, just outside the collimator. This fixation light provides to the patient a reference to avoid movement during treatment and maintaining the gaze direction prescribed by the treatment plan. Treatment geometry is verified through an orthogonal x-ray imaging system. The panels are equipped with a cross-wire made of tungsten of 0.15mm diameter whose intersection coincides with the projection of the isocenter on the panel itself. The position of the cross-wire is calibrated as to maintain geometrical consistency. Eye movements during the irradiation are detected by a TV camera, whose position can be adjusted to provide clear images of the treated eye. The images are displayed on a monitor and if during the irradiation the eye, for any reasons, has deviated from the planned position, the beam is manually interrupted.

Figure 12-Ocular Treatment Room at PSI (Paul Sherrer Institute) in Switzerland.

1.3.3 Diagnosis

The presence of a possible tumor inside the eye is evaluated by different clinical examinations that the ophthalmologist requires after a first eye inspection with an ophthalmoscope. In order to confirm the diagnosis, imaging tests are required: fundus inspection, angiography and ultrasounds B-scan are the basis exams, but X-rays, Magnetic Resonance Imaging (MRI) can be also performed. Fundus photography, Figure 13 (a), consist in a photo of the patient's retina acquired by an optical camera through the aperture of the pupil. It is used to inspect and localize anomalies in relation to the principal structures of the internal eye surface such as optic disk, macula and retina. It can be used for diagnosis of the nature of the lesion, differentiate between different types of tumours and define the geometrical properties such as basal extension shape. The conventional machines can acquire images that cover 30 to 120 degree of the retinal area. However, in the last decade, ultra-wide field fundus photography has been introduced. These machines scan the retinal surface with red and green lasers that can achieve a coverage of approximately 200° of the retinal area in a single image (LD, Chong, & Au, 2015).
Ultrasound, Figure 13 (b), is a very common exam for diagnosis and definition of geometrical properties of the tumour: ultrasonography is typically used to measure the choroidal melanoma size, evaluate internal tumor reflectivity, and look for melanoma extension behind the eye into the orbit called extrascleral extension.

Another important exam is the Optical coherence tomography (OCT) (see Figure 13 (c)). OCT provides high-resolution images of the retina using a low-coherence light. The long wavelength light can penetrate into the scattering medium and generate images showing the cross-sectional part of layers of tissues with micrometer resolution. Ultrasonography (A-scan, B-scan) is the conventional imaging technique to measure the thickness of intraocular tumours. However, B-scan becomes inaccurate when the tumours are small and ineffective for lesion below a certain thickness. On the other hand, OCT features the necessary resolution for these small tumours being routinely used in such cases. In addition, OCT is particularly useful to detect the retinal detachment that might occur due to the tumor growth. Furthermore, most commercial OCT machines can perform also the Fluorescein Angiography exam. Fluorescein is a fluorescent dye that enhance the contrast of the inner

eye blood vessel allowing the clinical staff to evaluate the blood circulation inside the eye. Even though this test is not required to diagnose ocular melanomas, the exam is routinely used to exclude the presence of an eye tumor or detecting other eye pathologies.

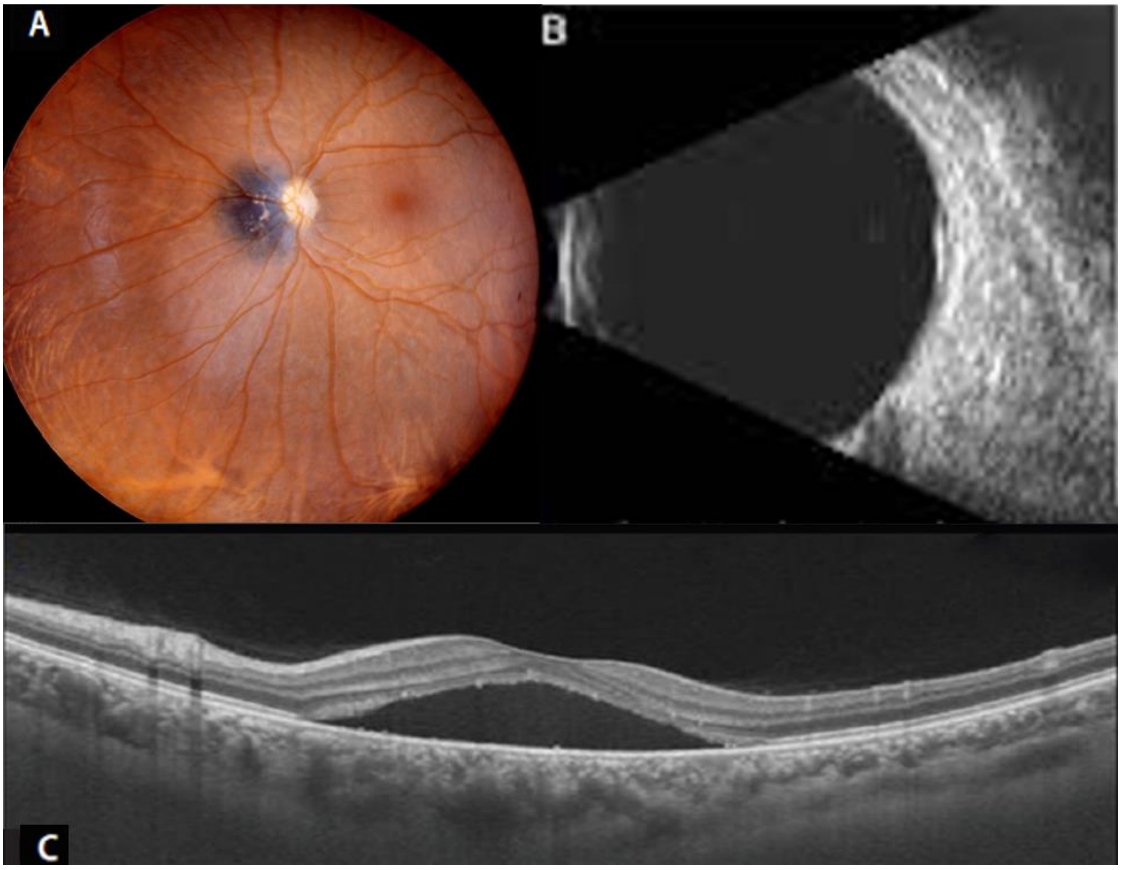

Figure 13- (A) Colour photograph of the left eye showing circumscribed choroidal melanoma very close to the optic disk. (B) Ultrasonography of the lesion was difficult because is a very small tumor and is barely appreciable. Optical coherence tomography is, however, useful in delineating the margins (C).

CT, MRI and PET-CT can all be used both for diagnosis purposes and to identify eventual spreading of the disease outside the eye. For instance, if the metastasis is in the liver, blood tests can easily detect it. Contrarily, patient presenting small pigmented tumors of less than 3mm thickness and 10mm diameter are not subjected to immediate treatment. However, regularly scheduled appointment are set to monitor the eventual growth and intervene in a timely fashion, if necessary (Char DH, 1978).

1.3.4 Clips implantation

After the diagnostic stage, if a malignancy is present and the patient is referred to OPT, a surgical intervention takes place. The aim of this procedure is to place a number (3 to 6, depending on the shape and position of the tumor) of tantalum markers to the external layer of the sclera at a known distance from the tumor and from other visible structures, Figure 14 (a). The markers or "clips" are button-shaped surgical fiducials with a 2.5mm diameter made of tantalum, a radio-opaque material. Clips serve as a radiographic fiducial point for treatment planning and for daily image guidance. The tantalum is also a non-magnetic material so, the patient can undergo MRI scans if needed. In the following a description of the surgical procedure is presented.

The conjunctiva is opened along the edge of the cornea and depending on the tumor position, a combination or all four of the principal ocular muscles are pulled out and used as a lever to adjust the eye position inside the ocular cavity and access the posterior part of the sclera as conveniently as possible. Then, the surgeon sutures clips relying as close as possible to the tumour and in a position pre-defined during surgery preparation. If the optic disk is present in the field of view of the fundus photography, it can be used as a reference to plan the positioning of the clips. During surgery, the tumor margin are detected using a transillumination probe. This probe is, quite simply, a light source that is positioned on the cornea of the patient's eye and illuminate the interior through the aperture of the pupil. As a result, the tumor produces a shadow that is visible from the outside on the surface of the eye. This shadow is used to infer the tumor margin and consequently placing clips in an appropriate position (see Figure 14 (b)). If the tumor is thick, the surgeon has to move up and down the probe to really differentiate the projection of the tumor apex from the base. Depending on the location of the tumor, the surgeon can decide which trans-illumination method adopt: transpupillary, when the probe is placed on the cornea, or trans ocular, when the illuminator is placed on the outer sclera surface. After a clip is implanted the distances to other clips, to the tumor margin and to the limbus margin are measured with a manual caliper. Also, the limbus diameter is measured.

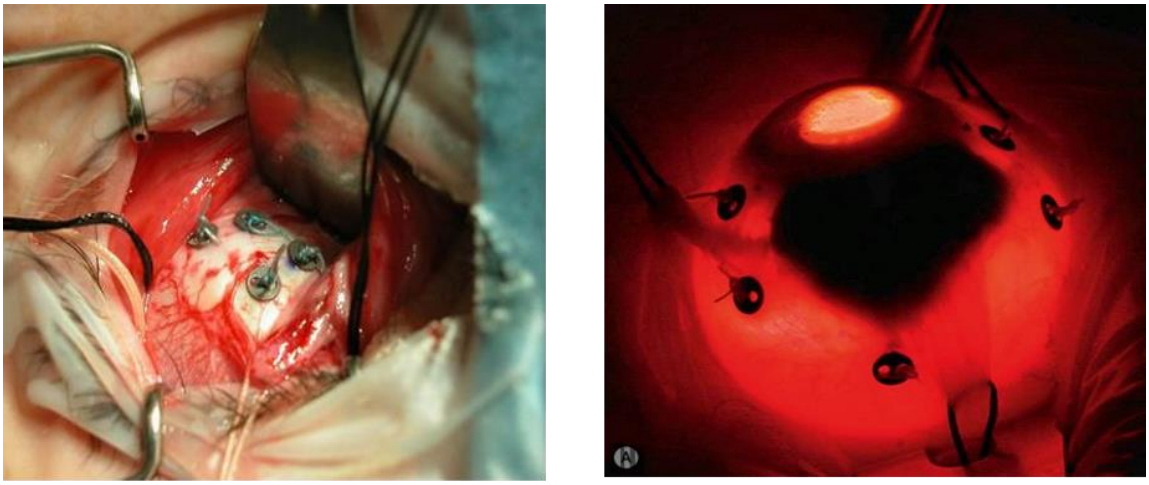

a) b)

Figure 14- (a) Four clips have been sutured on the retinal surface: they serve as a marker for tumor delineation and for the treatment planning phase. (b) Transillumination showing the base of a ciliochoroidal melanoma.

At the end of clips implantation, the muscles are released, and the eye returns to its normal position inside the orbit. Finally, the conjunctiva is closed using surgical stitches.

An optimal positioning of the clips and an accurate measurement of its position is essential to a successful radiation therapy. This method, although clinically successful, is highly invasive and operator dependent. A lot of factors could induce errors in the process: the presence of a retinal detachment can generate shadows through trans-illumination that are difficult to differentiate from the tumor's; the posteriority of the tumor can limit access and visibility; the colour of the tumor could affect the intensity of the shadow as it is the case for an amelanotic melanoma which generates a mild shadow that can be confused with physiologic pigmented lines; uncertainties in the distances measured with the manual caliber.

1.3.5 Treatment Planning

Generally, a few days after the clips' surgical implantation the patient undergoes the simulation phase of the treatment workflow at the OPT facility. Specifically, the patient is positioned in the treatment room, immobilized on the chair with a thermoplastic mask and a bite block and wears eyelid retractor. The chair is sent to a general position and then, while the patient is asked to fixate in a straightforward direction, the pupil is roughly aligned to the beam axis using, usually, the beam's eye view camera. The reflection through a passive mirror placed along the beamline allows image acquisitions of the patient's eye from the beam point of view. The goal of this procedure is to position the eye centroid to the isocenter of the treatment room, which is along the beam axis. When the eye position stabilised a couple of x-ray images are acquired with orthogonal X-ray imaging system installed in the treatment room.

Then, the treatment planning process begins. The most common treatment planning system (TPS) for ocular proton therapy is EYEPLAN.
This planning software was developed by Goitein and Miller (Goitein & Miller, 1983) at Massachusetts General Hospital (MGH) and latter modified at Paul Sherrer Institute, Switzerland and Clatterbridge, U.K. (Perret, 1988). Along with the images acquired during simulation, Eyeplan requires a few clinical measurement such as: eye length, lens thickness and sclera thickness obtained with ultrasonography, tumor shape, base dimensions and height obtained with B-scans, clinical measurement of tumor-to-clips, clips-to-clips and clips-to-limbus.
Starting from the three-dimensional position of the clips identified on X-ray images, the eye globe is generated and can be modelled as either a spheroid or an ellipsoid tangential to the clips and adapted, in length, to US measurement. This spherical eye model includes structures like macula, optic disk, lens. However, these organs' position within the model is defined according to a standardized eye model rather than a patient-specific personalization. Finally, the definition of the tumor volume completes the description of the model. The clinical target volume (CTV), that is defined as the volume that contains the gross tumor volume (GTV) and subclinical microscopic malignant lesions, has to be reconstructed from the fundus photography and from ultrasound measurements. Firstly, the base of the tumor is drawn on the unfolded EYEPLAN plane (the 'fundus-plane'). The

dimension and the shape of the tumor must satisfy the spatial constraints given by the clips-to-tumor distances and is, sometimes, verified using fundus photography that provides an important additional visual information about the base extension. Tumor height and apex coordinates are integrated into the model, and a series of base-apex envelopes are generated by EYEPLAN following different mathematical models. The one that best fits the patient-specific anatomy is selected among them.

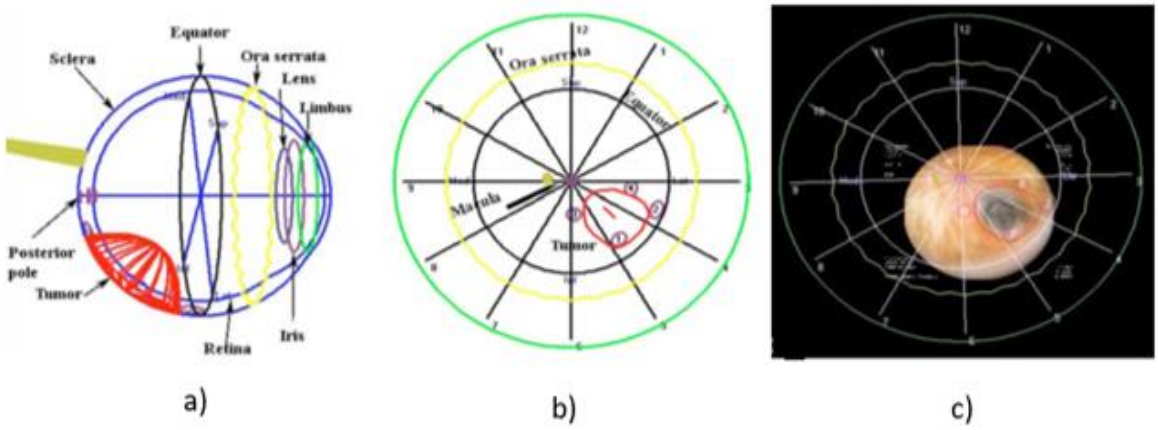

Figure 15-(a) The anatomy of the left eye in a transverse plane relative to (b) fundus view is clearly visible, how the arclength of the different structures is taken into account. The different structures are labelled in both views. (c) shows the superimposition with the fundus photograph after a 2 points registration.

Figure 15 (a) shows an EYEPLAN model: physical landmarks such as ora serrata, limbus and equator are also included in the model. To represent the inner eye surface as a plane, the model is unfolded using the macula, located at the posterior pole of the sphere, as the center of the projection (b). The generation of the 'fundus plane', by means of unfolding operations, allows the representation of the EYEPLAN model on a bidimensional plane, which can be compared with the fundus. The unfolding operation takes into account the arc length, i.e. the curvature of the globe and as a result the radial distances in the fundus-plane are directly proportional to the arch length along the retinal meridian. Although the distances are conserved along the radial directions, the distances circumferentially are corrupted by the unfolding procedure (Daftari, et al., 2010). EYPLAN allows the fundus superposition to the unfolded model through a registration based on two fiducial points, the optic disk and the macula. These organs are manually selected on the fundus photograph as Figure 15 (c)

depicts. If one of the two landmarks is not visible a rough estimation of the position is used. The registration allows the overlap between the unfolded model and the fundus photograph through an affine matrix, composed of a roto-translation and a scaling component.
By superimposing the tumor created in Eyeplan to the registered fundus photography, one can verify the extent of the tumor base and eventually include areas seen on the fundus image that were not fully detected. Daftari et al., reviewed and replanned, for a small subset of patients, ocular melanoma cases with superimposition of pre-treatment and post-treatment fundus imaging in the EYEPLAN software to determine patterns of local failure and evaluate the benefits of using fundus photography in the clinical routine. As reported, in one-third of the local treatment failure cases, the superposition of the fundus photograph to the treatment plan may have improved tumor localization (Daftari, et al., 2010).
Although the majority of centers (80%) uses EYPLAN as a TPS, other are available: at Charité Hospital Berlin, Germany the OCTOPUS have been used clinically since 2006 (Marnitz, 2006). This TPS allows the use of 3-D images dataset like MRI and CT for a more patient-specific eye model. The advantages in the introduction of the MRI information will be discussed further on.

After having generated the eye model, the TPS performs the dose calculation. For each treatment geometry, the target volume is centered to the isocenter and the resulting modulation and aperture of the collimator is calculated. Then, dose distribution is calculated and different plans for different gazing angles are compared by means of dose-based metrics, such as DVH (dose-volume histograms).
The goal is to select the optimal gaze angle to guarantee robust target coverage and minimize the dose that each critical ocular structure will receive. Safety margins are defined by clinical indications in the distal and proximal part along the beam axis and in the aperture of collimator (Kacperek A. , 2012). A 2.5mm margin is applied isotropically in the major part of the centers.

1.3.6 Irradiation

Once the treatment plan is approved and the irradiation can start. Uveal melanomas are usually treated with 60 Gy delivered in four subsequent fractions. A patient positioning procedure precedes the irradiation. The patient has to be positioned in such a way that the tumor centroid is located at the room isocenter and has to look at a given gaze direction, as defined during treatment planning. Patient's gaze direction is stabilized by the active fixation of a Light Emitting Diode placed in a predetermined position according to the polar and azimuthal angles provided by EYEPLAN. Treatment geometry verification is performed by acquiring orthogonal X-ray projections (Figure 16 (a)). The comparison between the clips positions identified in the X-rays images and the ones generated by the EYEPLAN, corresponding to optimal target-beam alignment, allows estimating the corrections parameters to be applied to the chair and to the fixation light position with respect to the beam axis. This procedure is repeated through a trial-and-error approach and usually requires three or four iteration (Via, et al., 2015). During treatment, the stream of images coming from a camera are displayed on a monitor inside the control room for monitoring eye movements. A manual rough segmentation of the iris and pupil is done on a touchscreen monitor to establish a reference. If during irradiation the eye moves outside the overlying boundaries the beam is manually stopped by the clinical personnel.

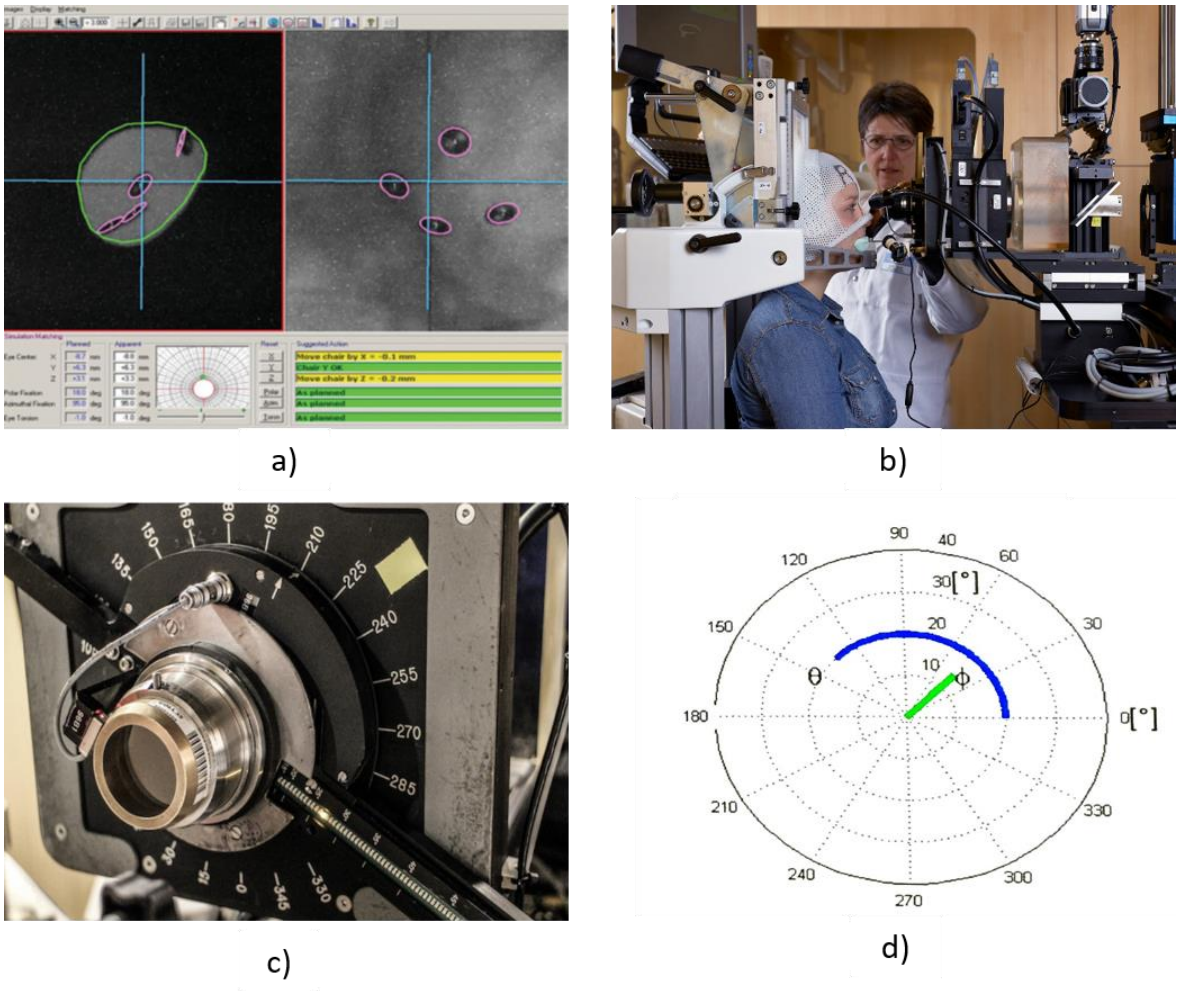

Figure 16- (a) Daily electronic portal imaging overlays the acquired X-ray with treatment plan to determine the necessary shifts in three-dimensional coordinates. (b) Patient on the treatment chair, immobilized by a mask and a bite block. (c) Position of the eye is defined through the fixation light- a small LED that can be placed to any point in the proximity of the nozzle. The coordinate system of the angle disk (d), visualizing the parametrization by the polar angle φ and the azimuth Θ

1.3.7 Clinical outcomes

An improved dose conformity providing an efficient sparing of surrounding organs at risk has made OPT a more favourable therapeutic alternative for conjunctival melanomas, resistant to conventional radiation therapy (Wuestermayer, 2006). Also, for juxta-papillary tumors and lesions thicker than 7 mm protons are preferred with respect to brachytherapy (Maschi, Thariat, Heault, & Caujolle J, 2015) (Mourtada & Koch, 2005).

In addition, comparison between PT and SRT treatment plans suggested increased homogeneity in the target and an improved sparing of healthy tissues in proton planning while showing no substantial changes in target dose conformation (Weber, 2005).

Five-year tumor local control and eye retention, reported by different institutions, ranged between 91%-96% and 75%-91%, respectively (Stefan, 2004) (Damato B, 2001) (Fuss, Loredo, Blacharski, Grove, & Slater, 2001) (Gragoudas, et al., 2002) (Sas-Korczyska, Markiewicz, Romanowska-Dixon, & Pluta, 2014) (Olsen, 2007). However, patient's visual acuity, due to proton radiation side effects, worsen in 33-47% of cases if the lesion is sited near the two structures engaged for vision: macula and optic disk (Fuss, Loredo, Blacharski, Grove, & Slater, 2001).

1.4 Uncertainties in the definition of the tumour volume

So far, the entire treatment workflow has been presented with a brief description of its principal steps. This section wants to focus on the uncertainties in the definition of the clinical target volume (CTV), i.e. the volume that will be targeted for irradiation in the treatment, that characterise the most used TPS (EYEPLAN). As mentioned above, the target in EYEPLAN is generated from a manual drawing based on fundus information and other clinical parameters. Even though the tumor delineation is done as precisely as possible, there are potentials for error which can lead to poor modelling and thus to problems for tumor control and/or late side effects.

The principal reasons for discrepancies are:

- Uncertainties in the eye length measurement performed using ultrasound;
- Irregular shape of the eye;
- Uncertainty in proton range calculation because of the approximation of the eye density;
- Uncertainties in surgical measurements of the clips position;
- Inaccurate initial fixation at time of simulation;

The first and second points relate to the EYEPLAN's eye model simplicity and its inability of capturing the correct anatomy for patient presenting non-spherical eyes. In most of the cases such discrepancies can result in improper modelling.

It is worth to stress out that the EYEPLAN model is generated through geometrical considerations and without any kind of patient specificity except for the eye length and the tumor thickness.

Uncertainties related to proton range calculation are due to the fact that EYEPLAN utilizes a uniform eye density of 1.05 leading to a slightly corrupted dose evaluation (Kacperek A. , 1995). Structures, such as lens, cornea and the vitreous humour absorb different amount of energy with respect to the one absorbed by a uniform density tissue, so that the delivered dose could be slightly different than the one calculated with the TPS. Of course improvements in the eye modelling and tumor delineation result in a more reliable and consistent dose estimation both for the target and for the organs at risk (Simiantonakis, Cordini, & Fuchs, 2005).

The discrepancies introduced by the clips measurements can affect the generation of the clinical target volume (CTV). The difficulties related to the clip implantation procedure, may lead to overestimation of the target volume. Tumor detection through transillumination, the possible presence of infiltrations in the nearby tissues and other uncertainties force the surgeons to adopt a rather conservative approach during such measurement. Clips are typically sutured around the tumor, particularly, and in the presence of uncertainties about clip-to-tumor distance, the measurement are performed in a more conservative way. As a result, the tumor based generated during treatment planning could be greater leading to an overestimation of the clinical target volume (CTV).

As already mentioned in the previous chapter, EYEPLAN allows the fundus photograph fusion: the fundus image registered to the EYEPLAN fundus-plane can confirm or suggest a replanning in case of marginal miss, thus leading to benefits in terms of more accurate tumor volume delineation (Daftari, et al., 2010). Despite this improved function, the clinical target volume (CTV) remains usually overestimated due to the choice of adopting a conservative approach that, however, guarantees a complete target coverage.

Therefore, a multimodal approach based on composite information from multiple imaging sources could minimize the previously cited issues, allowing the introduction of patient-specific parameters in the model definition.

CT and MRI are two 3D imaging techniques that are commonly used in radiation therapy and some attempts have been made to introduce these methods in the TPS. For example, the already mentioned OCTOPUS (Daftari, Aghaian, O'Brien, Dillon, & Phillips, 2005) provides the full integration of 3-D imaging obtained by MRI and CT. Because of the superior soft-tissue differentiation and spatial resolution on MRI compared with CT, a more accurate identification of the eye geometry and an improved personalization of the eye model could be achieved. It is important to mention that MRI provides some advantages with respect to CT. Firstly, clips produce artefacts on CT images, whereas these artefacts are not as prominent in MRI in which clips simply produce a lack of signal, i.e. a ‘dark’ zone. The scleral infiltration can be detected with MRI with a sensitivity of 100% and a specificity of 50%, whereas for extrascleral extensions, sensitivity is 100% and specificity is 89% (Recsan & Fodor, 2002). Finally, MRI allows the acquisition of volumetric images without delivering additional non-therapeutic dose to the patient.

1.5 MRI-based approaches

The introduction of the MR acquisition in the treatment planning has already been investigated. Due to a high contrast of soft tissue, a lot of different structures inside the eye are distinguishable, potentially enabling the creation of a patient specific model.

The first study in this direction was conducted by Daftari et al. in 2005. The aim was to evaluate the capability of 3D T2w fast spin echo MRI images in target delineation and to compare it to the conventional technique.
A subset of 60 cases of choroidal melanoma was considered in this study: tumors were firstly delineated by using EYEPLAN and then they were outlined on the MRI images by two different radiation oncologists. Although the tumor segmentation was performed manually, the interobserver reliability, such as the differences observed in the two delineations, was excellent, with a mean variation of −0.22±4%. Interestingly, the tumor lesion wasn't directly visible with the MR scans for 6 (10%) patients, for which the ultrasounds measurements confirmed a tumor height <3 mm; 7 patients (11.7%) were affected by small melanomas; 22 patients (36.7%) by medium size melanomas; large melanomas were found in 22 patients (36.7%), and extra-large tumors in 9 patients (15%). Figure 17 shows a comparison between the tumor volumes estimated by two observers and the ones derived from EYEPLAN. The distribution is divided into two parts a) for small and medium sized tumors and b) for large and extra-large tumors.

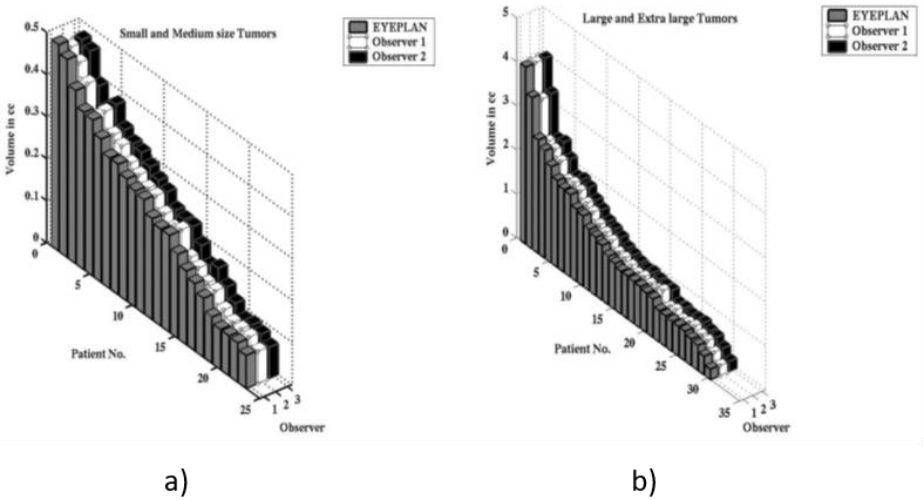

a) b)

Figure 17-The tumor volume identified by two observers (physicians) in comparison to the tumor volume obtained from EYEPLAN software. (a) For small and medium size tumors and (b) large and extra-large tumors. The differences among tumor volumes in comparison to EYEPLAN tumor volume were minimal.

The tumor volume difference varied between 6.3% and 1.1% for small size tumors, from −4.1% to 5% for medium size, from −5.7% to 6.2% for large, and from −2.4% to 5.8% for extra-large tumors. The volumetric data estimation shows sufficient agreement between EYEPLAN and 3D MRI imaging and a difference of ±6% was observed between the two approaches.

Overall, Daftari reported that the tumor volumes defined with the MR imaging shows a high degree of accuracy in term of shape and dimension. Furthermore, in some patients with extra-large tumors the additional information obtained from MRI images suggested a modification of base and shape. (Daftari, Aghaian, O'Brien, Dillon, & Phillips, 2005).

However, Daftari reported the presence of some drawbacks: firstly, in 6 patients the MRI couldn't identify the lesions in which the tumor heights were less that 3mm. Secondly, the possible presence of retinal detachment together with small or medium size tumors, could introduce additional complications during the tumor identification. Thirdly, the tumor identification could be affected by partial volume effects, i.e. the loss of contrast between two adjacent tissues in which more than one tissue type occupies the same voxel.

Although the presence of some problems, Daftari stated that the use of MRI could guarantee a high similarity in the volume identification with conventional methods.

In another publication, Marnitz in 2006 carried out a comparison between the MRI-based treatment planning OCTOPUS and the conventional EYEPLAN. OCTOPUS allows for the direct integration of the MRIs of the patient' eyes into the treatment planning software together with the conventional clinical dataset. The CTVs were calculated with OCTOPUS and compared to the EYEPLAN ones. The clinical target volumes computed by OCTOPUS show a reduction of the CTV in all the plans without compromising safety, with a mean reduction factor of 1.7 ± 0.4 % (T1w) and 2.2 ± 0.5% (T2w) (Marnitz, 2006).

Other study on this topic has been conducted by Via et al in 2019: 33 patients affected with uveal melanomas were subjected to MRI imaging. A manual target delineation by two radiation oncologists was performed and the resulting volumes were compared with the ones produced in EYEPLAN and applied clinically. The MRI protocol used in this study included 3D volumetric T1-w (Interpolated Breath-hold Examination -VIBE) and T2-w *SPACE (Sampling Perfection with Application optimized Contrast using different flip angle Evolution) sequences with an isotropic resolution of 0.5 mm.

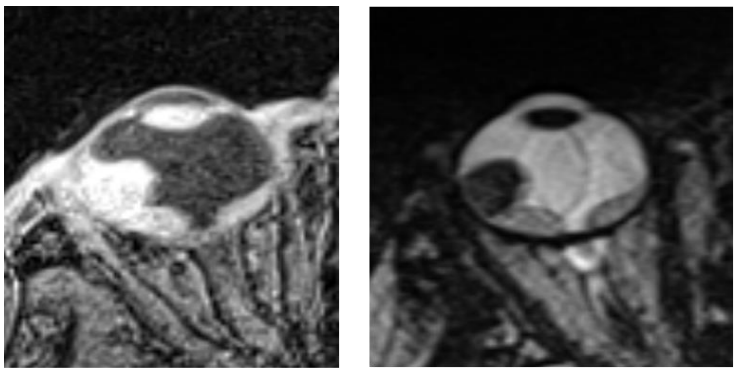

Figure 18- A T1-vibe and T2W-space MRI images of an exemplary uveal melanoma patient are shown on panel (a) and (b), respectively

T1 and T2 scans were registered for all patients to enable a more precise segmentation of the eye structures and tumor differentiation to retinal detachment: uveal melanomas are identifiable as high signal masses on T1w and as low signal masses on T2w scans.

Contrarily, the associated retinal detachment appears as a moderately high signal region on both T1w and T2w scans. This allows an easier discrimination between the lesion and retinal detachment on T2w scans. Targets were then compared considering not only the overall volume but its height and base (extension on the uvea) and by assessing their position with respect to the surrogate markers implanted during surgery.

Generally, they reported that the target volumes identified on MRI scans were on average smaller than the reference ones and in 2 out of 33 cases (6%), the tumor lesion was not directly visible on MRI images (Via, et al., 2020).

Overall, the previous studies highlighted that MR imaging could be a valid alternative to create a patient specific model of the eye and tumor. The comparisons between the tumor volumes obtained from the 3D MRI images and the ones generated by EYEPLAN show a high similarity between the two methods. On the other hand, when the lesion is too small the MR is unable to detect it: this is the principal limitation of MRI as a standalone tool for eye modelling in OPT, as Via stated (Via, et al., 2020).

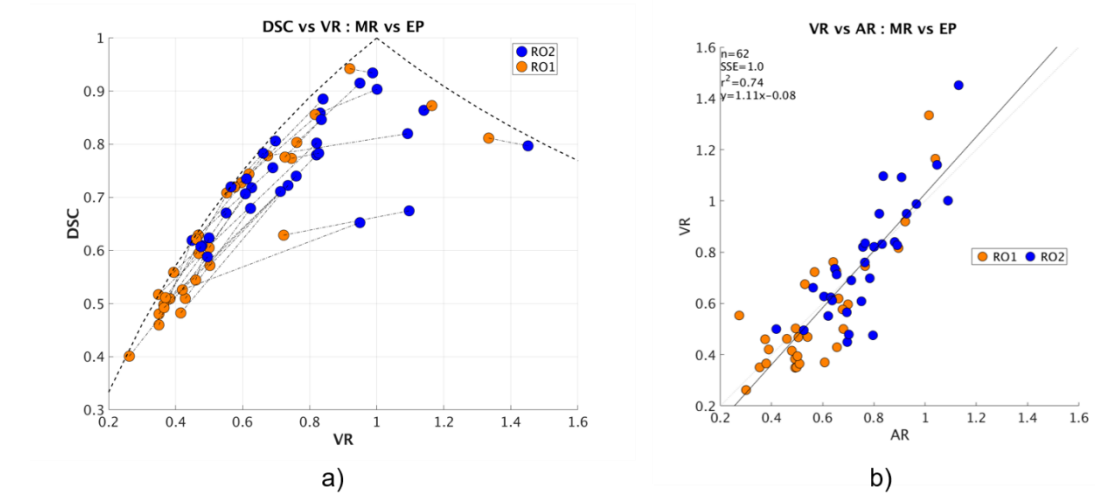

Figure 19 - Geometrical comparison of target volume definition for the whole subset. (a) orange and blue dots represent values of volume ratios and DSCs against the Eyeplan model for delineation performed by radiation oncologist one (RO1) and two (RO2), respectively. The black dash line represents DSC values as a function of volume ratio corresponding to complete inclusion of the smaller volume into the larger one. Target volumes delineated by RO1 clustered towards smaller volume ratios values than the corresponding volumes for RO2. On panel (b), correlation plot for volume and area ratio between lesions delineated by RO1 (orange) and RO2 (blue) and the Eyeplan Model shows significant positive correlation between areas and volume definition.

Despite the fact that MR provides the patient specificity that is missing in EYEPLAN, it is clear that it is necessary to integrate other image modalities to achieve a correct model and target definition, as MRI based eye modelling could not be sufficient for some patients.

1.5.1 Fundus and MRI registration

A first step towards a patient specific multimodal eye model through the fusion of MRI and fundus was reported by De Zanet et al. in 2010, in which the volumetric MRI images were integrated to the high-resolution fundus photograph.

The method proposed by De Zanet requires the identification of at least two common landmarks between MRI and fundus in order to perform the registration in a similar fashion as Eyeplan does.
However, the identification of two common landmarks both present in MRI and fundus results challenging. In MRI more prominent structures such as optic nerve, sclera, lens, and cornea are detectable whereas retinal blood vessels, optic disk, and macula (or fovea) are only visible in fundus photography. Therefore, the first common landmark was inferred on MRI by considering the optic disk as the conjunction point between the optic nerve and the sclera surface. The second landmark was instead derived according to the eye anatomy. Specifically, it is known from the literature that, in a typical human eye, the axis from the lens to the macula (the visual axis) and the optical axis (the symmetry axis of the human eye) present a deviation of 4◦ (Broehan, Rudolph, Amstutz, & Kowal, 2011) and that the distance between the macula and the optic disk is 4.4 ± 0.4 mm (De Silva, et al., 2006).
The combination of these two constraints allows for the definition of the macula position on MRI scans. Each constraint generates a "probability zone" and, by considering the constraint average values, the zones results in two intersecting circumferences, in which two possible macula positions are probable and the position closer to the optic axis incidence with the retina is chosen to be the macula.
In the final step, the found landmarks are used to fuse MRI and Fundus photography into one 3-D model. The fusion is performed in three steps.

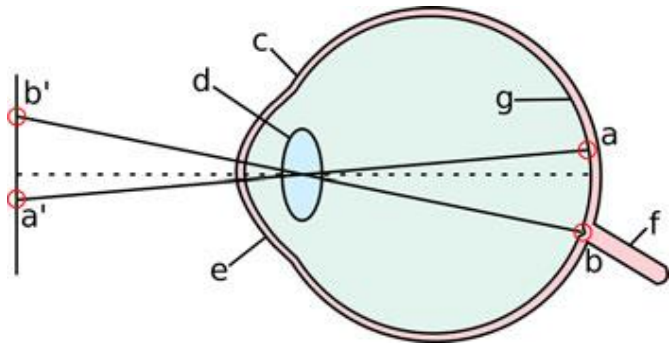

Figure 20- Schematic of the projection through the lens (d) of the fovea (a) and the optic disk (b) for the virtual image generation. The two points (a') and (b') are the images of the landmarks. Additional anatomical structures are indicated (c) sclera, (d)lens, (e) cornea, (f) optic nerve, and (g) retina.

First, a projection through the lens of the landmarks onto a perpendicular plane with respect to the optical axis in MRI is done. Through a two corresponding points registration, by using the projected macula and the projected optic disk as landmarks, the virtual image is registered with the fundus and then, the resulting image is back-projected, again through the lens, onto the retinal surface (see Figure 20).

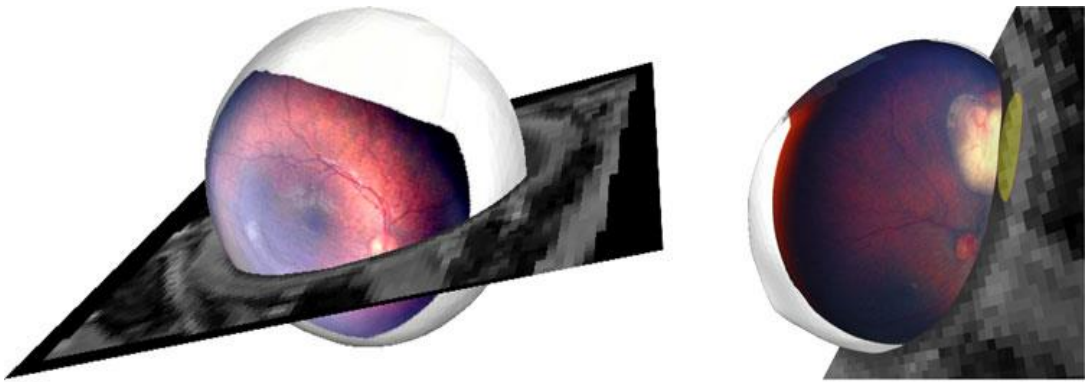

Figure 21- MRI and Fundus fusion from different perspectives, without (a) and with (b) a tumor. (a) Exterior view with the optic nerve entering in the place of the optic disk of the Fundus. (b) Mapping with an incidence of a Retinoblastoma (yellow).

An example of the fundus fusion is reported in Figure 21. Although a ground truth for the verification of the registration is not available, the left image clearly shows that the optic disk of the fundus is located in the position where the optic nerve enters the eye and so

through visual inspection a plausible result is shown. On the right side a retinoblastoma (in yellow) is visible. Thanks to the resolution of the fundus, the base of the tumor is better represented and the physician's diagnosis could be improved: by projecting the fundus photography in the correct location on the segmented retina more critical structures can be avoided for radiation treatment. Furthermore, tumours only visible in the fundus now can be potentially identified in the MRI-based model.

1.6 Aim of the project

The aim of this thesis is put forward to the realization of a patient specific multimodal eye model through the combination of different imaging modalities, which would potentially reduce the uncertainties in current Treatment Planning Systems (TPS) and could, for some types of ocular melanomas, avoid clips implantation.

This work is part of a project in collaboration with the Paul Scherrer Institute, a proton therapy center in Switzerland, which has played a key and a leading role in the treatment of ocular tumors. Over 7000 patients with ocular tumors, mainly uveal melanoma, have been treated with protons at PSI since 1984. The research program has the goal of upgrading and modernizing many aspects of ocular melanoma treatments by moving towards a workflow where the treatment is performed without the need of surgically implanted clips. By eliminating the need for surgery would represent a major improvement in patient comfort and treatment effectiveness. Indeed, the positional relationship between the clips and the tumor relies on the experience of the ophthalmologist performing the surgical intervention, and this is a contributory factor to the treatment success (Egger, et al., 2001). Additionally, due to its simplicity, the currently used eye model has limited accuracy, and the surgical implanted clips could introduce an additional source of inaccuracy (Newhauser, 2007) (Carnicer, 2013). Finally, moving to ocular irradiation without the need for pre-treatment surgery would have a substantial impact on the cost of the treatment. A clip-less approach would however require a more accurate definition of the eye model on which the treatment is planned.

Our aim is therefore two-fold. Firstly, we aim at improving the actual EYEPLAN unfolding method by including the fundus acquisition geometry for a more accurate fundus fusion. Since the fundus photography is acquired with a dedicated device that can be moved by the operator in order to guarantee, if possible, a complete tumor visibility, an unfolding method that takes into account the variations of the image acquisition geometry is presented, in order to reduce the tangential distortion that affects the unfolded structure boundaries.
Then, we proposed a methodological framework from MRI and fundus integration, which aims at avoiding anatomical constraints towards a patient-specific image-based approach. This would potentially provide a personalized model with respect to the current clinical

procedure, as implemented in the EYEPLAN TPS. Indeed, it is worth to highlight that the EYEPLAN model relies on a geometrical model of the eye in which the patient-specificity is provided only by the inclusion of ultrasound measurements used for establishing the eye dimension and the tumor thickness. Thus, the integration of a high-resolution image, as fundus photography, with a 3D acquisition as provided by MRI, allows deriving an improved and personalized model of the eye.

2 Patients' dataset

In this chapter we will discuss the diagnostic technique of fundus imaging (section 2.1) and the main characteristics of the machines used clinically. Also, in section 2.2 we will present the patient cohort and the acquired MRI data, highlighting the main requirements that have been necessary for the patient subset selection.

2.1 Fundus photography

Fundus photography is a widely used diagnostic technique aiming at the visualisation of the inner surface of the eye. The main structures that can be visualized on the fundus image are the optic disk, the macula, the vessel network and the possible presence of malignancies or other pathologies. It is typically used in ophthalmic oncology for the diagnosis of ocular melanomas and it can also be used for angiography exams. This exam allows the examination of the retina and choroid circulation by using a fluorescent dye (Abràmoff, Garvin, & Sonka, 2011).

In the conventional treatment workflow of ocular proton therapy this image can be used to better define the tumor base within the geometrical eye model built during treatment planning phase. To do this, the spherical/ellipsoidal eye model is unfolded into a two-dimensional plane, scaled and then registered to the fundus photograph by using the optic disk and the macula as landmarks.

Machines for fundus photography consist of two principal elements: an optical camera for image acquisition and a light source for eye illumination. For conventional optometrist fundus photography system, the illuminating light is projected to the interior of the eye through the pupil aperture. In order to avoid reflections produced by the cornea and the lens, the illumination is delivered using the peripheral area of the pupil (see Figure 22 (a)) . The optical camera collects the light reflected by the retina passing through the central part of the pupil to generate an image. However, conventional fundus cameras feature a quite limited field of view (FOV) and pupil dilation is required for evaluating the retinal periphery. One image captured by a conventional fundus camera can only cover a small portion of the whole

retina (about 30°- 45°). An example of the fundus field of view acquired with a conventional fundus camera is shown in Figure 23 (a). Many tumors and diseases can occur in more anterior parts of the retina (Arepalli, Kaliki, & L., 2015) , and a wide-field fundus devices are required for a better detection and treatment evaluation.

Other system for fundus photography, like the Panoret-1000, uses trans-scleral illumination of the retina. In this case, the light illuminates the eye interior from the outside, instead of passing through the pupil. As the light needs to be delivered from the sclera, a fiber that provides the light gets in contact with the sclera surface in the so called 'trans-sclera illumination' (Figure 22 (b)). Concurrently, an optical camera collects images through the pupil aperture. This system can achieve a wider field (100°) fundus images without the use of pharmacologically induced pupil dilation. The fundus images with the Panoret machine are acquired while the patient is lying on a couch. Two operators, handling the optical camera and the light source respectively, acquire several retinal images aiming at the complete tumor acquisition. The Panoret allows the operator to move and tilt the camera in order to include all the principal structures in the same photograph. To protect the outer surface of the eye and avoid distortions due to the air and cornea interface, a gel is applied on the patient eye.

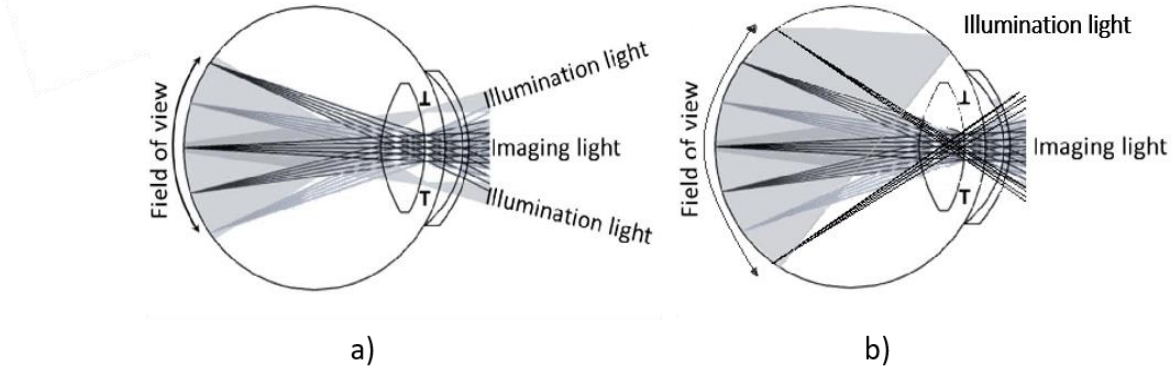

Figure 22-- Schematic illustration of different illumination schemes for retinal imaging. (a) shows illumination and imaging light paths of trans-pupillary illumination and (b) shows a trans-scleral illumination. The area between the T shapes represents the pupil aperture.

The Panoret FOV is visible in Figure 23 (b).

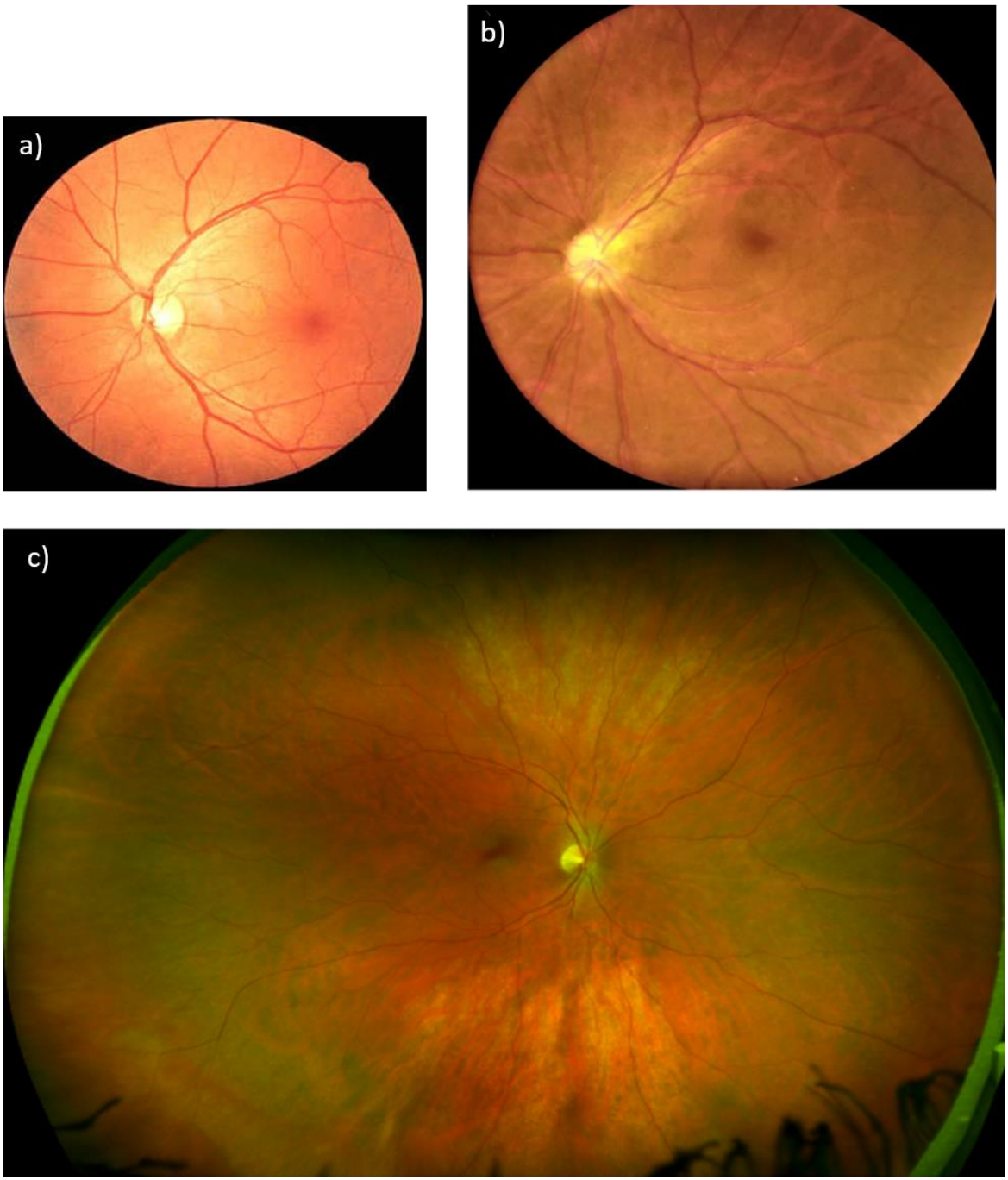

Figure 23- (a) the conventional fundus cameras are able to acquire a FOV of 35-40°. (b) the Panoret field of view reaches the 105°. (c) the ultra wide field machines, such as the Optos machine, can reach 200° and can cover the 85% of the whole retina.

Currently, new imaging technologies are available, and they have received the designation “ultra-widefield,” owing to the significantly increased viewing angle they provide, around 200° (see Figure 23 (c)). Unlike full spectrum white light used in conventional devices, Ultra-Wide Field (UWF) machines incorporate laser wavelengths that scan simultaneously the retina surface. The imaging system usually delivers dual frequency laser (523 nm green laser and 633 nm red laser), which are reflected by the retina surface and provide both green and red separation views. Each laser source is capable of providing specialized information, and the fusion of the two views generates a high-resolution image able to cover the 85% of the retina surface.

Despite the new technologies provide an ultra-wide retina field, the Panoret system is still used as a clinical standard for conventional fundus photography in ocular oncology. With respect to the other machines it presents many important advantages:

- Tumor visibility and contrast
- Lesion colour can be used for diagnostic purposes
- The possibility to control light source and camera position allows to better image

Because the retina is lighted up with a white light, the real colours are maintained with respect to the UWF machines, in which the retina is illuminated with the red and the green component of the light spectrum. The colour of the lesion is an important information that the ophthalmologist uses during the diagnosis.

The fundus images that have been used for this thesis work are a acquired at the Hospital Ophtalmique Jules-Gonin with a Panoret-1000 machine.

2.2 MRI data

Thirty-three patients referred to the PSI for ocular proton therapy underwent onto a diagnostic phase, in which the patients have been subjected to several diagnostic exams, including the fundus photography acquisition performed with the Panoret-1000 machine. Then, they underwent clips surgery and conventional treatment planning with EYEPLAN. In addition, the 33 patients underwent an MRI scans under ethical approval.

The MRI scans were performed with a 1.5T MAGNETOM AERA (Siemens, Erlangen, Germany) using a surface loop coil (diameter: 7cm) and half-head coil. Imaging included 3D volumetric T1-weigthed (Interpolated Breath-hold Examination -VIBE) and T2-weighted *SPACE (Sampling Perfection with Application optimized Contrasts using different flip angle Evolution) sequences with an isotropic resolution of 0.5 mm. The sequence parameters are showed in Figure 24(c).

During image acquisition, patients were asked to gaze a fixed point through its reflection on a mirror placed in front of the patient in order to maintain a stable gaze direction.

T1 and T2 volume registration (i.e. rigid alignment) was performed on the software Velocity (Varian Medical System, Palo Alto, CA, USA) and the structures identification done manually by a radiation oncologist. The eye globe volume, i.e. external surface of the eye, was delineated on the T2w scans by inclusion of the vitreous body, the anterior chamber and the tumor.

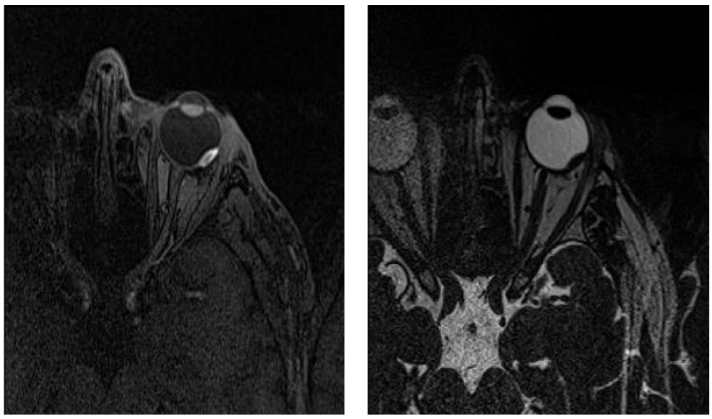

a) b)

	T1-VIBE	T2-SPACE
TR/TE [ms]	6.55 / 2.39	1400 / 185
SliceThickness [mm] / Gap [%]	0.5 / 20.0	0.5 / 0.0
Voxel size [mm]	0.5	0.5
Flip angle	12	150

c)

Figure 24- (a) T1-vibe and (b) T2W-space MRI images of an exemplary uveal melanoma patient. Panel (c) includes all information about sequences parameters.

An isotropic enlargement (1 mm) of the structure was added to consider the scleral and corneal layer thicknesses. Finally, the segmented volume was visually inspected for consistency on the T1w images.

Tumor delineation requires a more detailed integration of information coming from T1w and T2w scans. Usually, uveal melanomas are detectable as high signal masses on T1w and as low signal masses on T2w scans. Contrarily, the associated retinal detachment appears as a moderately high signal region on both T1w and T2w scans thus making it easier to distinguish between the lesion and retinal detachment on T2w scans. The target volume (TV_{MR}) delineation was therefore done on all three principal planes (coronal, axial and sagittal) and constantly crosschecked between the registered T1w and T2w scans.

The structures corresponding to clips and lens were segmented on the T1. Tantalum clips are not directly visible on MRI images but can be recognized as a lack of signal and segmented subsequentially. The delineated structures resulted in a patient specific MRI model which is illustred in Figure 27.

The key criterion for choosing the patient cohort was the complete visibility of the tumor, the optic disc and the macula in the fundus photography. Macula and optic disk serve as anatomical landmarks for the registration operation. If one of the two landmarks is not visible, the registration cannot take place and two are the cases that could happen: the first

is that the tumor grows under the two structures, making the identification impossible, and the second is that the tumor is located in the equatorial or in the anterior part of the eye.

Among the 33 patients, only 10 patients fulfilled the previous criterion and have been considered in this work. Six patients (60%) presented lesions extending to the eye equator, 2 small, 3 medium and 1 big. In the other 4 cases (40%), the tumors were posteriorly located, 1 medium and 3 big. The median volumes were 788 mm^3 (IQR: 330 mm^3), 426 mm^3 (IQR: 353 mm^3) and 118 mm^3 (IQR: 30 mm^3) respectively for big, medium and small tumors.

3. Methods – part I: conventional procedure

In sections 3.1 and 3.2 we will analyse the unfolding procedure and the registration process between the unfolded EYEPLAN model and the fundus image, as conventionally implemented. The novel contributions of our work will be described in Methods - part II.

Globally the conventional approach used by the actual TPS for fundus fusion can be resumed with the following flowchart:

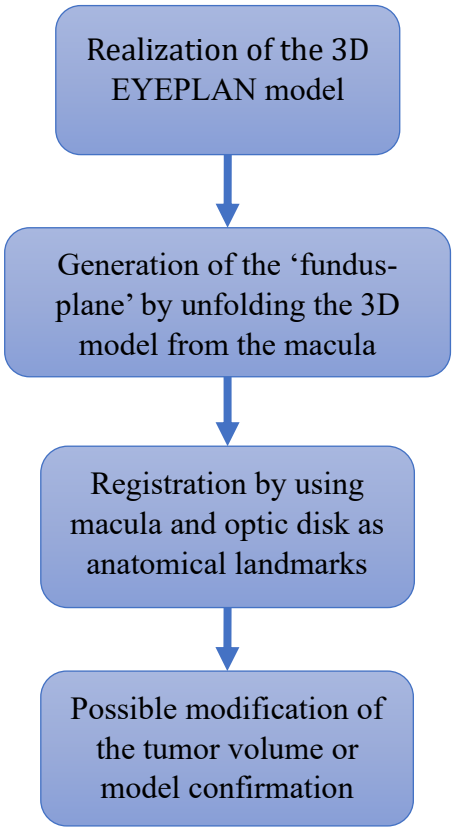

Flowchart 1- the whole process performed by EYEPLAN that allows the superposition between the EYEPLAN unfolded model and the fundus photography.

Each step will be widely explained in the two following sections.

3.1. Unfolding procedure

To perform the fundus fusion between a bi-dimensional image and a 3D model, that it can be the MRI model or the EYEPLAN model, it is necessary that the 3D model is unfolded onto a 2D plane, thus the fusion is done in a common dimensional space.

Of course, the unfolding method has to consider all the uncertainties that the fundus photography possesses and, in some way, has to try to compensate for them. Indeed, several uncertainties affect fundus photography which makes it a quite unconventional optical imaging technique.

The light provided by the trans-scleral probe reflects onto the retina surface and is conveyed towards the fundus camera aperture outside the eye. Before reaching the camera, the light passes through the lens which modifies the light behaviour and subsequently, it crosses the interface between the cornea and the previously applied gel. The change of the refraction index introduces another distortion that the fundus camera has to compensate. The use of a trans-scleral illumination when a big tumor is present could potentially generate shadow artefacts: in the fundus image, the tumor is lighted up and its apex shadows the posteriorly retina surface making more difficult the tumor segmentation. Other uncertainties are

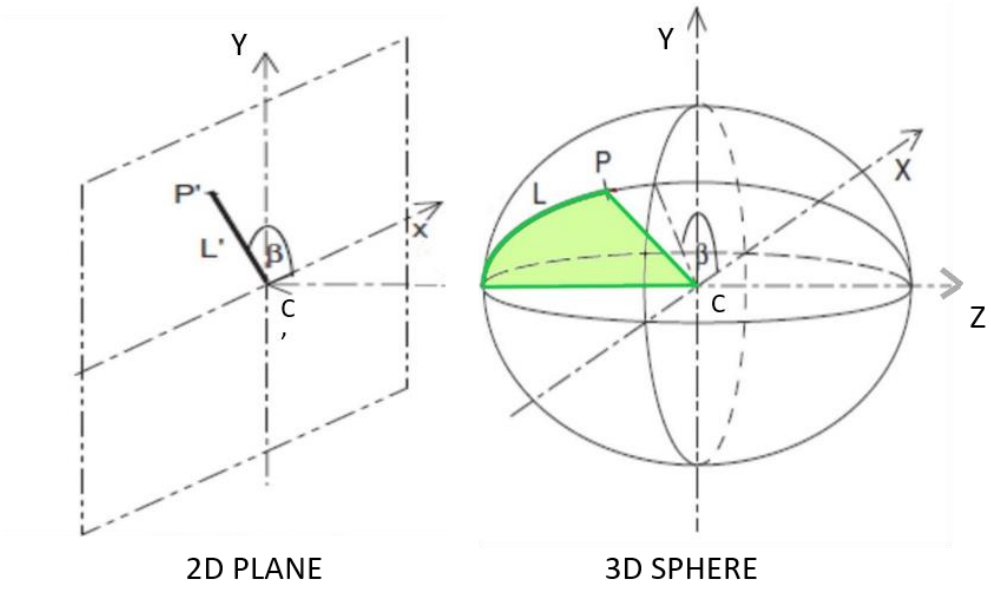

Figure 25- Unfolding procedure of the curved retinal surface onto a bi-dimensional plane, in with the arclength is maintained.

introduced by the fundus acquisition geometry that remains unknown once the image has been acquired.

Evans et al. in 2004 (Evans, Nestoridis, Papadopoulos, & Rimm, 2004) proposed a retinal unfolding method in which the macula is used as a projection center and the radial distances on the bi-dimensional map correspond to the arc lengths on the eye surface. This approach guarantees that, at least on the 2D plane, the relative distances between points are consisted to the spherical representation, at least in the radial direction. However, the further away from the center of projection, the more prominent tangential distortion might appear, thus making the 2D unfolded plane a non-Euclidean space. It is also noteworthy that using this method, the angle between the center of projection and points belonging to the plane is preserved from the corresponding points on the 3D object. Nevertheless, this method is considered the more appropriate to simulate the fundus photography image acquisition and has been adopted in this work.

Because the eye model in this case is a spheroid, the distances must be described as 'spherical integrals' representing line integrals on a spherical surface in which the first point of the line is the macula and the last point is any point on the eye surface.

The method is shown in Figure 25 . The point P on the sphere is mapped on the 2D plane as point P'. The distance O-P is equal to the distance O-P' calculated along the spherical surface, while the β angle between the x-axis and the vector CP remains unchanged. Length can be calculated by a line integral as follows. The length L of a curve $f: [0, t_0] \rightarrow \mathbf{R\text{^}2};\ t \rightarrow f\ (t)$ is given by:

$$L_{to} = \int_0^{to} || f'(t) ||\, dt$$

Where for the sphere

$$f(t) = (r \cos t\,, r\ sin\ t)$$

However, under the simplified assumption that the surface is a sphere, the arc length can be calculated more easily. Also, to simplify the mathematics, other assumptions are made:

- The sphere is centered in the origin of the three-dimensional Euclidean space: $C = [0 \quad 0 \quad 0]^T$.
- The point O from which the model is unfolded is $O = [0 \quad 0 \quad -r]^T$ where the z component is the sphere radius.
- The projection plane, UF: $a \cdot x + b \cdot y + c \cdot z = d$ is normal to the direction $\overrightarrow{CO}$ and therefore the components a,b are equal to zero while the component c is equal to 1. The center of this plane O_{UF} is defined as the projection of the point O upon it.

Knowing the coordinates of the arbitrary point P on the spherical surface, it is possible to calculate the angle $\widehat{PCO}$, that is the angle ϑ, using the following formula:

$$\vartheta = \cos^{-1}\left(\frac{\overrightarrow{CP} \cdot \overrightarrow{CO}}{||\overrightarrow{CP}|| \, ||\overrightarrow{CO}||}\right)$$

Where the operation $\overrightarrow{CP} \cdot \overrightarrow{CO}$ expresses the dot product:

$$\overrightarrow{CP} \cdot \overrightarrow{CO} = \left[CP_X \; CO_X \; + CP_Y \, CO_y \; + CP_Z \; CO_z \; \right]$$

Using the angle ϑ and the sphere radius, it is possible using the following mathematical relationship to obtain the length of the arc (L) connecting the center of projection to the point P.

$$L = radius \cdot \vartheta$$

Given the normal plane to the vector $\overrightarrow{CO}$, UF and the coordinate of the point P=(P_X , P_y , P_z), it is possible to calculate the orthogonal projection of this point on the 2D

plane to obtain the vector that connects this projection to the center of the plane (O_{UF}). This allows to estimate the angle β that defines the position of the point P on the sphere surface along with the arclength L, as follows:

$$P'=A\backslash B$$

$$\begin{bmatrix} x \\ y \\ z \\ t \end{bmatrix} = \begin{bmatrix} 1 & 0 & 0 & -a \\ 0 & 1 & 0 & -b \\ 0 & 0 & 1 & -c \\ a & b & c & 0 \end{bmatrix} \backslash \begin{bmatrix} P_X \\ P_y \\ P_z \\ d \end{bmatrix}$$

$$\beta = \tan^{-1}\frac{x}{y}$$

Now the length L and the angle β are known and is finally possible to calculate the coordinates of the point P', corresponding to the point P of the spherical surface and unfolded upon the bi-dimensional plane UF.

$$P' = \begin{bmatrix} L \cdot \cos\vartheta \\ L \cdot \sin\vartheta \\ d \end{bmatrix}$$

By performing these operations for all points belonging to the three-dimensional spherical model, the complete 2D projection is obtained. This is the mathematical base of the procedure defined as *unfolding*. Figure 26 illustrates the result of an unfolding process applied to the EYEPLAN model of one patient.

The model is centered in the origin of the three-dimensional plane and the symmetry axis of the eye is aligned to the z-axis of the coordinate system with the lens placed towards the positive direction. The macula, which is defined in EYEPLAN as the point on the posterior part of the sclera along the eye symmetry axis, i.e. the south pole of the spheroid modelling the eye globe, is selected as the center of the unfolding procedure. The plane UF on which the projection is generated, is orthogonal to the axis z, parallel to the symmetry axis of the

eye. As a result, all points belonging to the surface of the spheroid that models the eye globe can be unfolded on this projection plane. This is not limited to the point of the eye globe but includes also all anatomical and pathological structures that intersect with the eye globe. Thus, contours of structures such as the macula, optic disc, clips and tumor base are subject to the unfolding procedure (see Figure 26).

It is important to underline that, despite the EYEPLAN model being a geometric model adapted to the patient, the projection preserves the distances between the points only in a radial direction. Along the tangential one, the distances are compromised: this means that the distance between two points along a circumference with arbitrary radius on the projection, is not equal to the distance calculated on the model between the same points, thus making it a non-Euclidean space.

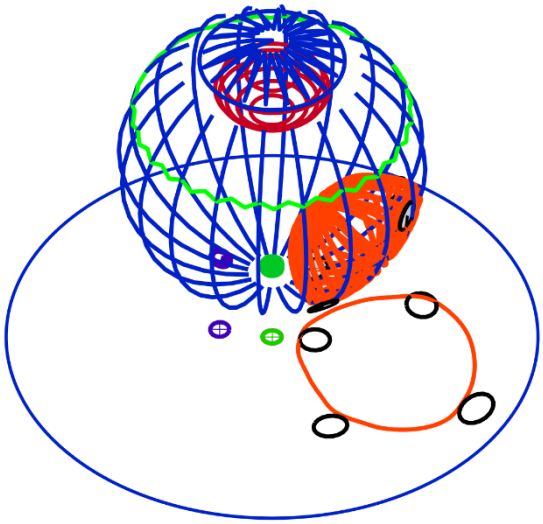

Figure 26- 3D EYEPLAN model and the respective unfolded model in which the macula has been considered as a fulcrum: the macula is represented in green, the optic disk in purple, the tumor is in red and the clips are represented in black.

The unfolding method can be applied also to the MRI model. Despite the EYEPLAN model that is a geometric model, the MRI model comes from the T1 and T2 information integration: as already mentioned, the structures come from the segmentation of the MR volumes performed by a radiation oncologist and the resulting patient-specific model is shown in Figure 27 (a).

In order to apply the mathematical unfolding operations to the MRI model it is necessary to introduce some assumptions that allow a simplified calculation of the arclength along the sclera surface. Despite the EYEPLAN treatment planning system that models the eyeglobe as a sphere, the MRI segmented eyeglobe has size and shape that varies from patient to patient.

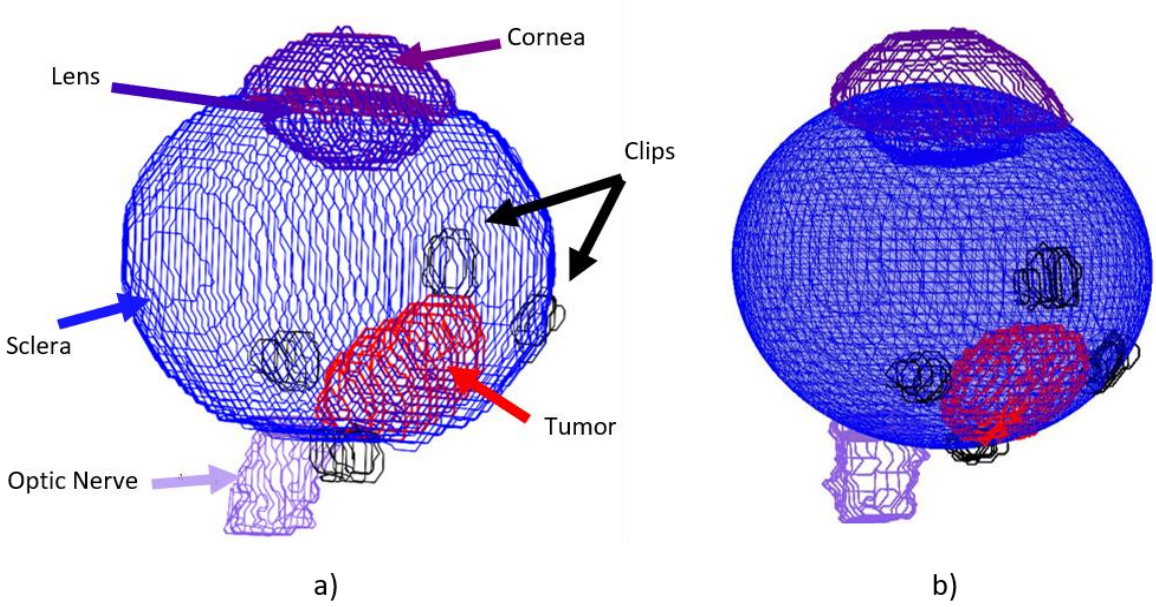

Figure 27- (a) 3D MRI model in which all the structures are highlighted. (b) the patient specific sclera surface is approximated with a spherical surface in order to allow the arclength calculation.

Although the geometrical shape of a human eye globe is more similar to an ellipsoid, for our purposes it has been modelled as a spherical object (see Figure 27 (b)). The surface of the sclera delineated on MRI images was approximated to the best-fit sphere and the resulting sphere center considered as the center of the eye.

When the unfolding algorithm is applied, only the points that are on the sclera surface are unfolded because, for these points, the radius is constant and the arclength can be easily calculated. In order to define the structure bases that is located on the modelled spherical sclera surface, only the points that are distant less than 0.5mm from the sclera have been

considered. These points are projected onto the sclera surface and subsequently unfolded. This operation must be done for the tumor, the clips and the optic nerve head (ONH).

As it will be explained later, the position of the macula cannot be identified in the MRI volumes and its position must be detected through the use of anatomical constraints.

For the sake of clarity and in order to show the output of the unfolding process, the MRI unfolded model is shown in Figure 28. In this model, the macula position is calculated in the same way as EYEPLAN does.

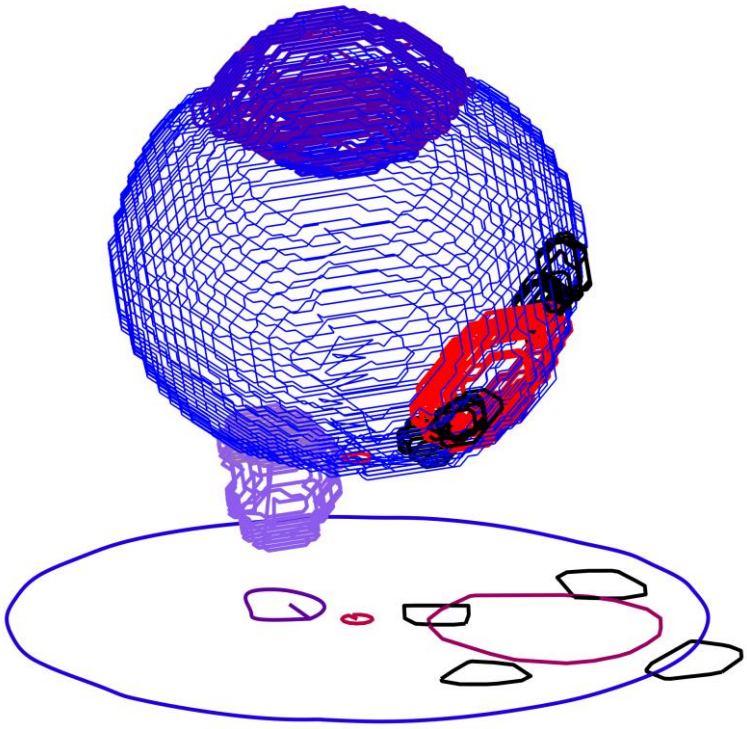

Figure 28- MRI model and the unfolded model on a bidimensional plane.

3.2 Registration of fundus images and eye model

Once the three-dimensional eye model, either the EYEPLAN or the MRI-based, is projected using the unfolding method on a bi-dimensional plane, the process of registration to the fundus photography can be done. The superimposition of the model structures to the fundus image is based on the identification of two common anatomical landmarks. It is necessary to identify two common points on the EYEPLAN/MRI projection and on the fundus. Typically, these points are the centroids of macula and optic disk as, along with the tumor, are the most visible features on the fundus photography. The EYEPLAN geometrical eye model embeds a representation of these two organs in the 3D model and therefore, after the unfolding procedure, their centroids are available in the unfolded plane as 2D points. The identification of the same points in the fundus photography can be done manually, through a visual analysis. The macula, i.e. the region with highest visual acuity and highest concentration of cells in the retina, is recognizable as a relatively small dark region, whereas the optic disk is a bright spot placed at the intersection of the choroid blood vessels (see Figure 29 (b)).

Obviously, the registration method relies on the visibility of these two organs on the fundus images and their representation on the eye 3D model. This is a fundamental requirement for a successful registration, and patients who have been selected for this study meet this prerequisite whereas if this were not the case, patients have been discarded. It is important to point out that the EYEPLAN model includes a representation of the macula and optic disk even though their positions are based on a pre-defined geometrical model that does not account for patient specificity. On the other hand, on MRI images neither organs are recognizable. The optic disk, however, can be modelled as the intersection point of the optic nerve to the sclera, because both structures are very well visible on eye MRI scans (Gala, 2015). The identification of the macula on the MRI volumes is based on anatomical considerations and represents the purpose of this study. The methods applied will be explained at length in the subsequent section of this thesis.

In principle, the relationship that allows to move from the 3D eye model domain to the fundus image domain and vice versa is based on the equivalence of the distance between the macula and optic disk in the fundus and the EYEPLAN/MRI projection. Assuming an

accurate representation of both organs in both domains, the distances can be considered as equal.

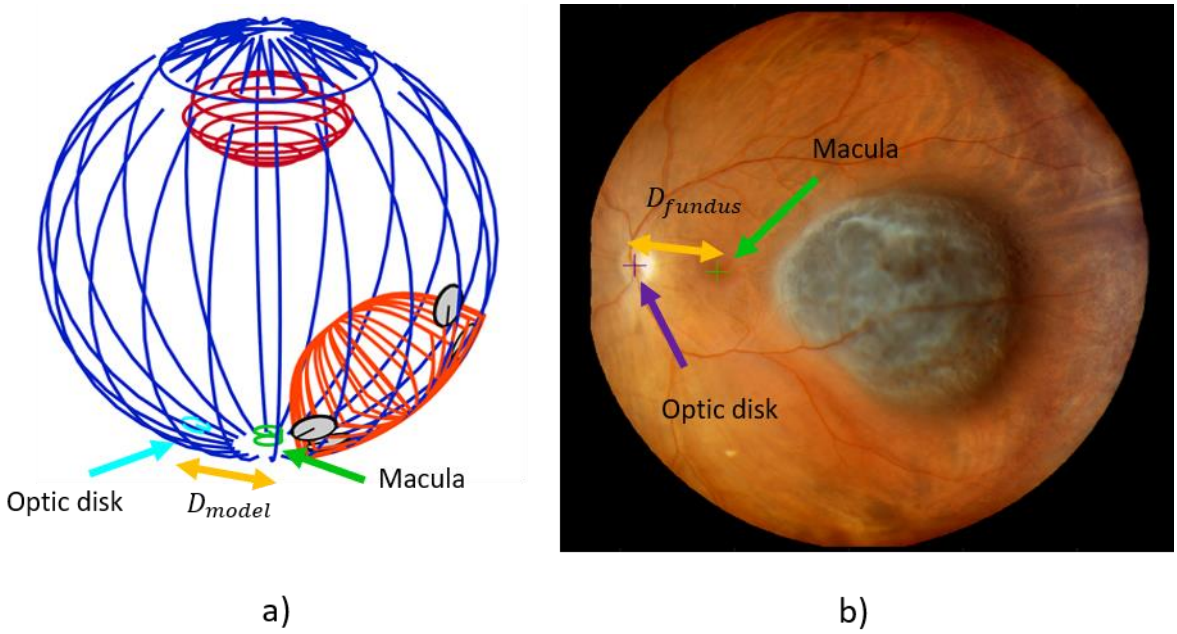

Figure 29-(a) EYEPLAN model and (b) fundus photography in which the structures that serve for the registration are highlighted. Also the distance between macula and optic disk is reported in both panels.

Specifically:

$$D_{fundus}[pixel] = \sqrt[2]{(x_{macula-fundus} - x_{optic\ disc-fundus})^2 - (y_{macula-fundus} - y_{optic\ disc-fundus})^2}$$

$$D_{model}[mm] = arclength(\overleftarrow{MAC_{model} - OD_{model}})$$

The two distances express the same anatomical information but in two different ways: D_{fundus} corresponds to the pixel distance of the two recognised features on the fundus image; D_{model} is the distance, calculated along the spherical surface of the eye model of the two anatomical landmarks.

As a result, a conversion factor K can be calculated as follows:

$$K_{\frac{pixel}{mm}} = \frac{D_{fundus}}{D_{proj}}$$

Thus, by multiplying the coordinates of the projection on the unfolded plane of the macula and optic disk centroids of the 3D model by the factor K it is possible to express them in the image domain, i.e. in pixel:

$$M_{proj-to-fundus} = K \cdot M_{proj} = K \cdot \begin{bmatrix} x_{macula-proj} \\ y_{macula-proj} \end{bmatrix}$$

$$OD_{proj-to-fundus} = K \cdot OD_{proj} = K \cdot \begin{bmatrix} x_{optic\ disk-proj} \\ y_{optic\ disk-proj} \end{bmatrix}$$

Then the registration based on corresponding points can be applied. The registration procedure is an optimization process which find the best transformation which minimizes the distance between corresponding points in the two images. The result of this operation is a 4x4 rigid roto-translation matrix which is defined by 6 independent parameters: Ω, Φ, K, X, Y, Z. The first three parameters represent the rotation component, each angle for each axis, and the last three represent the translation one.

$$\mathbf{\Gamma} = \left(\begin{array}{ccc:c} & \mathbf{R}(\Omega, \Phi, \mathrm{K}) & & \begin{matrix} \mathrm{X} \\ \mathrm{Y} \\ \mathrm{Z} \end{matrix} \\ \hdashline 0 & 0 & 0 & 1 \end{array}\right)$$

Because the 3D model is unfolded in a bidimensional plane and the rototranslation operation is performed with the 2D fundus photography, the rotation parameter K and the translational

parameter Z are equal to 0. Thus, to express the boundaries in the fundus domain, each point of the projection must be multiplied by the scaling factor K and then roto-translated with the matrix Γ.

The results are shown in the Figure 30:

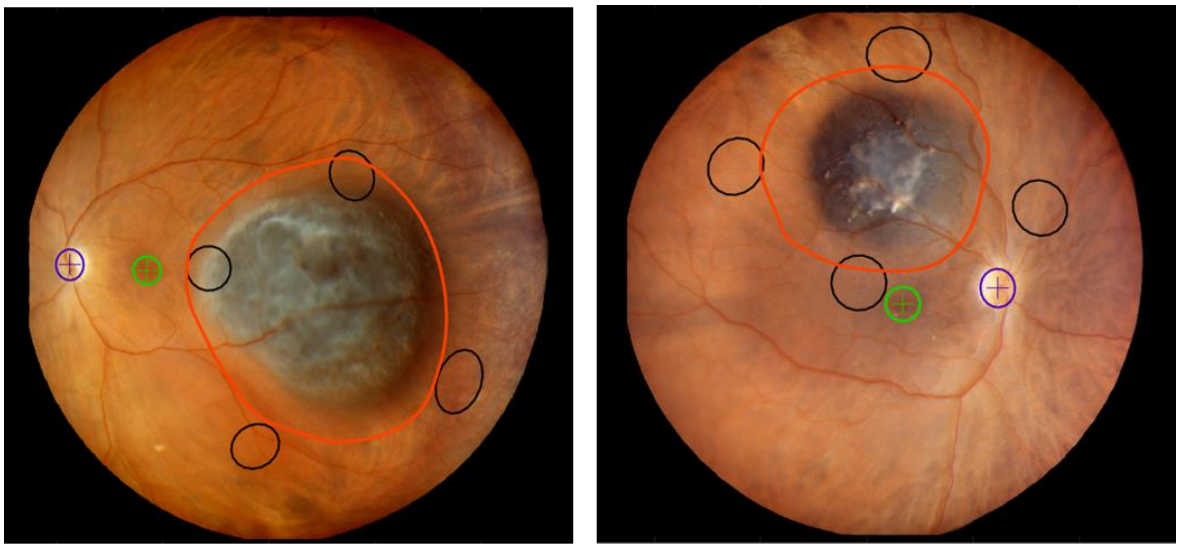

Figure 30- After the unfolding and the registration steps, the EYEPLAN structures can be represented on the fundus photography. Panels (a) and (b) shows the projections for two different patients. The tumor boundary is represented in red, the clips in black, macula and optic disk are represented in green and in purple, respectively.

This procedure is the one currently used in conventional treatment planning by the treatment planning system EYEPLAN. EYEPLAN features an interactive user interface that allows to manually align the model macula and optic disk superimposed to the fundus photography to their correspondent region on the underlying image. This is equivalent to manually changing the conversion factor K and the roto-translation matrix Γ and constantly moving the model until a good agreement, as evaluated visually by the clinical personnel, is found. This approach is highly user-dependent and therefore, in the context of this study, the selection of the macula and optic disk on the fundus photography is done once, and the roto-translation matrix Γ is univocally calculated using 2D point-based rigid registration upon the definition of the ocular landmarks in the three-dimensional eye model.

4 Methods – part II: improved and personalized approach

The following flowchart shows the changes that the proposed method will introduce compared to the conventional one. In the Flowchart 2, in blue are displayed the blocks that belong to the traditional way with which the registration is performed, already explained in Methods-part I. The following chapter aims at introducing novel approaches, displayed in the flowchart as orange blocks, that substitute the conventional ones. Firstly, we propose an unfolding method able to account for the variation of the fundus acquisition geometry in which the EYEPLAN/MRI model is no longer unfolded from the macula point, but is unfolded by having the fundus image center as a fulcrum (the blue block is replaced by two blocks). Secondly, we propose an innovative way for the macula definition inside the MRI model. As already said, the MRI model comes from the segmentation of the structures in the MR volumes. However, the macula is not directly visible in the MR scans, but its position can be defined in different ways: EYEPLAN (blue block) approximates its position according to a standardized eye model, whereas our method describes a probability area, according to some anatomical considerations, and uses an image-based approach for the identifying the position inside the afore-mentioned area (orange block). Finally, the registration with the fundus is performed, as usual, by using macula and optic disk as landmarks. It is worth to mention that EYEPLAN approximates also the optic disk position and in the MR model, as the optic disk is not directly discernible, it can be found the intersection between the optic nerve head (OHN) and the sclera surface.

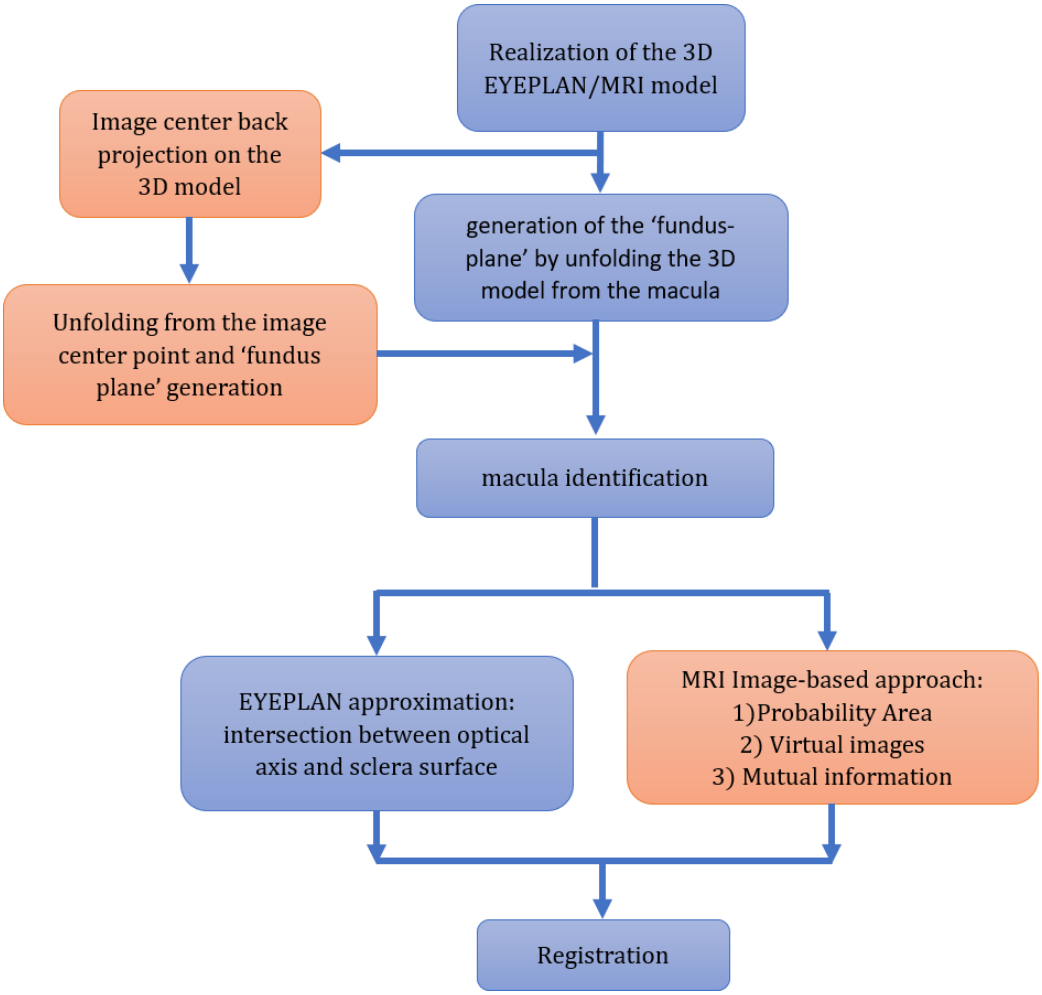

Flowchart 2- The modified flowchart according to the innovations that our work aims in introducing. First, 'image center' method and then, the introduction of the image-based approach for the macula identification (before the registration step).

4.1 Modelling fundus image acquisition – the *'Image center'* method

The conventional unfolding method has been replicated as Matlab code for the purpose of this study. We investigated the possibility of improving the geometrical consistency of the fundus image domain and the unfolded plane stemming from the eye model. This consists in the so-called 'image center' method that will be explained in following sections.

In particular, the section A will explain how the image center, identified in the fundus image, is folded back onto the 3D model, and the section B will explain how the new unfolding method, performed by the image center, will change the relationships between the segmented tumor and the projections that come from the conventional EYEPLAN-like and the center method, respectively.

A. Back-projection

Once the conversion factor K and the rototraslating matrix allowing to bring the 3D model features into the fundus image domain, are known, it is also possible to perform the inverse operation. Thus, any arbitrary segmented structure in the fundus photograph can be translated onto the 2D unfolded plane of the model and, subsequently, projected as points belonging to structures on the 3D model.

Suppose that P is a vector containing the points of a segmented structure on the fundus image: to bring it into the eye 3D model the following steps must be carried out:

1) From fundus image to bidimensional unfolded plane
2) From bi-dimensional unfolded plane to 3D eye model

As regards the first step the operation consists in the following equation:

$$P_{proj} = inv(\Gamma) \cdot \left[(P_{fundus}/K)\right]$$

Where Γ is the 4x4 roto-translation matrix that comes from the fundus-to-unfolded plane registration and K is the conversion factor.

The second point consists in a sort of back-projection of points from a plane to a sphere. Assuming the simplified geometry adopted in the unfolding process, the sphere center is aligned at the origin of our coordinate system and the plane is orthogonal to its symmetry axis (note that in case of an eye model, the symmetry axis is considered as the line connecting the center of the eye globe and the center of the lens) and that this symmetry axis is aligned to the axis Z. Therefore, one point of the structure that we want to back-project on the 3D model has coordinate $P_{proj} = [x \quad y \quad d]^T$, where d is point where the plane crosses the z-axis. In the same geometry, the south-pole of the sphere is aligned as previously explained and its coordinates are $M_{proj} = [0 \quad 0 \quad d]^T$.

The distance between macula and the point P_{proj} on the bidimensional plane corresponds to the distance along the spherical surface of this point and the macula.

$$D_{P_{proj}-M_{proj}} = \sqrt{(P_{proj})^2 - (M_{proj})^2}$$

Then, the angle θ is obtained using the sphere radius and the distance just calculated.

$$\theta = \frac{D_{P_{proj}-M_{proj}}}{radius}$$

This corresponds to the angle between two vectors: the first vector links the eye center and the posterior pole point (macula point) and the second vector connects the posterior pole and point P on the 3D model. Finally, the angle β is calculated on the 2D plane

$$\beta = \tan^{-1}\frac{P_{proj-X}}{P_{proj-Y}}$$

Where the numerator and the denominator are the x and y component of the vector that links the point P_{proj} and M_{proj}, respectively. The back projection of the point P_{proj} onto the 3D model is then obtained with the following formula

$$P_{3Dmodel} = \begin{bmatrix} sin\,\beta \cdot \sin(\pi - \theta) \cdot radius + M_{proj}(2) \\ cos\,\beta \cdot \sin(\pi - \theta) \cdot radius + M_{proj}(1) \\ cos(\pi - \theta) \cdot radius \end{bmatrix}$$

By repeating these steps for any points on the fundus photography, it is possible to retrieve their corresponding position on the 3D model. As such, the entire field of view (FOV) of the fundus image can be back projected on the three-dimensional model.

In the case of the EYEPLAN model, for construction, the macula lies exactly at the south-pole of the sphere modelling the eye globe. In our simplified geometry M_{proj} corresponds to the projection of the macula on the unfolded plane. Thus, by applying the previously explained back-projection procedure we obtain the FOV of the fundus image on the 3D eye model (see Figure 31).

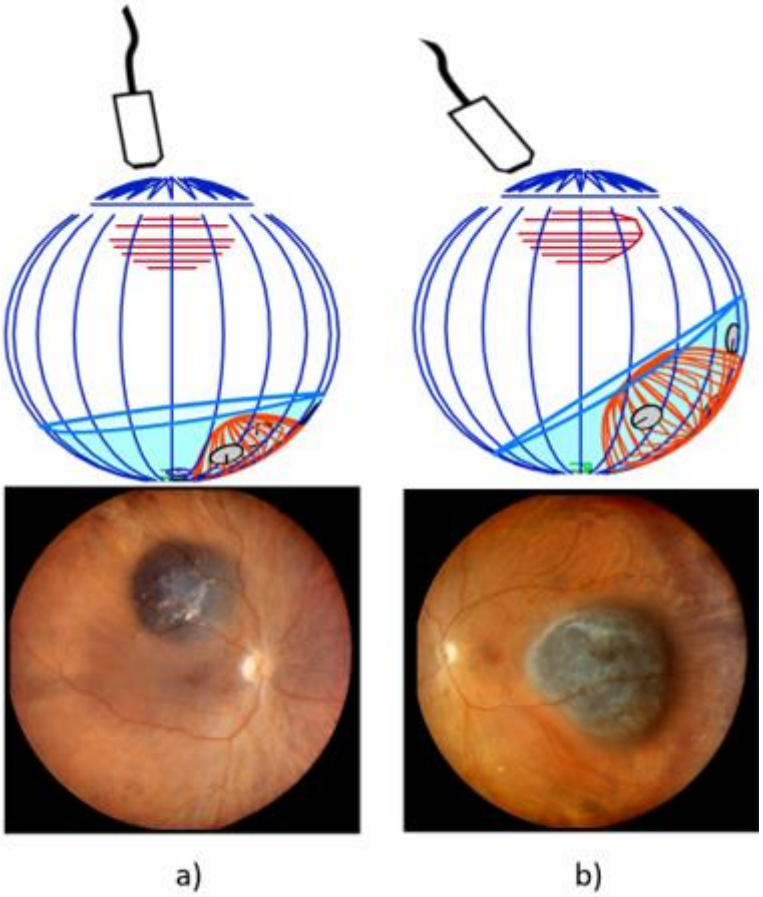

Figure 31- On the upper part of the figure illustrates the EYEPLAN models and the relative fundus FOV (in light blue). The boundaries of the fundus photos are folded back onto the 3D models.

In these two exemplary cases, the fundus photography field of view changes significantly according to where the tumor is located. Both lesions are posterior, but in case (b) the tumor is larger and in order to completely acquire it within the fundus image, it is necessary to adjust the camera position. For case (a), the tumor is posterior and with a limited volume and therefore only a slight movement of the camera was to achieve a proper tumor imaging with fundus. It is clear that the closer the tumor is to the equator, the more the fundus camera must be moved by the operator. By tilting the camera with respect to the pupil axis, the camera scans the surface of the retina, and consequently the field of view changes.

The unfolding procedure that was described previously has, for EYEPLAN, the macula as the center and generates a 2D image for which the distortion is in the proximity of the macula and increases tangentially as the radius increases. As such, it is clear that, if the fundus

photography has the macula close to the image center, the projection of EYEPLAN is able to properly describe the geometry of the fundus as, both in the fundus image and in the unfolded plane, the tangential distortions are minimal in the macula proximity and increase when moving to the periphery. However, if the macula is itself located in the fundus image periphery, the conventional EYEPLAN-like unfolding procedure may produce significant inconsistencies with the fundus.

B. Image center

To mitigate the distortion in the unfolded plane, the unfolding procedure should account for the variation in the image field of view. The routine implemented to back-project points from the fundus photography to the 3D model can be used for this purpose. The following explanation will directly reference to the exemplary case of a patient for the sake of clarity.

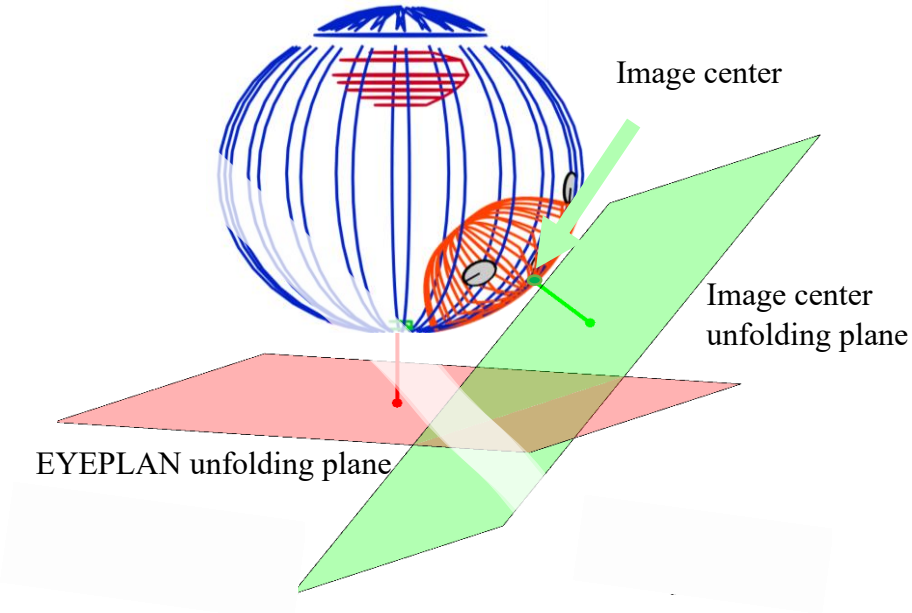

Figure 32-The model is unfolded, according to the EYEPLAN method on the red plane and by having the macula as fulcrum and, according to the Image center method, on the green plane and by having the image center as a fulcrum.

Starting from the fundus image of Figure 31 (b), the image center has been selected and back-projected onto the 3D model. Notably, the image center is located inside the tumor and distant from the macula. This suggests that for the conventional unfolding method, using the macula as the origin, the tangential distortion affecting the tumor contours will be higher. On the contrary, if the image center on the 3D model is used as the origin, on the region of the lesion, which is ultimately the region of interest, will be lower. To include the information on the image center, a slight variation of the simplified geometry adopted in the unfolding procedure is required. While the eye model (center of the sphere encompassing the eye globe) remains aligned to the origin of the 3D coordinate system and the eye symmetry axis is always parallel to the Z-axis, it is the position and orientation of the unfolded plane that changes. Figure 32 shows the plane on which the projection is generated with respect to the macula (in red) and with respect to the image center (in green). The plane on which contours are now projected is normal to the line connecting the eye center and the back-projected center of the fundus image. Thus, points on the three-dimensional eye model are now projected on this plane following the same geometrical principles outlined in the previous chapter. Then, the resulting projections can be registered with the fundus through the previously described operations.

The boundaries coming from the standard and the 'center of projection' methods are depicted in Figure 33 in red and green, respectively. It can be noted that there are no differences along the horizontal axis, that is, the axis defined by the intersection of the unfolded plane and the plane in which the macula, optical disc and image center on the 3D model lie. The radial distances along the maximum circumferences, i.e. all possible circumferences generated by the intersection of any plane passing through the eye center and dividing the sphere into two equivalent hemispheres, are preserved. On the other hand, the vertical distances, or the distances between points belonging to different maximum circumferences, undergo the so-called tangential distortion.

This distortion effect can be easily appreciated when we observe clips in both the cases depicted in Figure 33. In the EYEPLAN model clips are modelled as simple disks with a radius of 2.5 mm. The red clip number one is very close to the macula and its round geometry is preserved. Note now the clip number two: the effect of the tangential distortion tends to stretch shapes, in this case compromising the clip geometry. On the contrary, when using the image center as fulcrum, the distances between the clips and the image center are smaller,

resulting in a decrease in tangential distortion. Here also the clip number two preserves its circular geometry. It is reasonable to expect that the operator when acquiring fundus photography will try as much as he can to center the image to the lesion. Therefore, a method to mitigate image distortion in the tumor region should be beneficial.

In panel (b) the macula is at the edge of the FOV and the tumor is positioned in the center of the field of view. The more the macula is in the periphery, the more the tangential distortions are greater as the Figure 33 shows and the clearer it is that using the 'center projection' brings significant advantages.

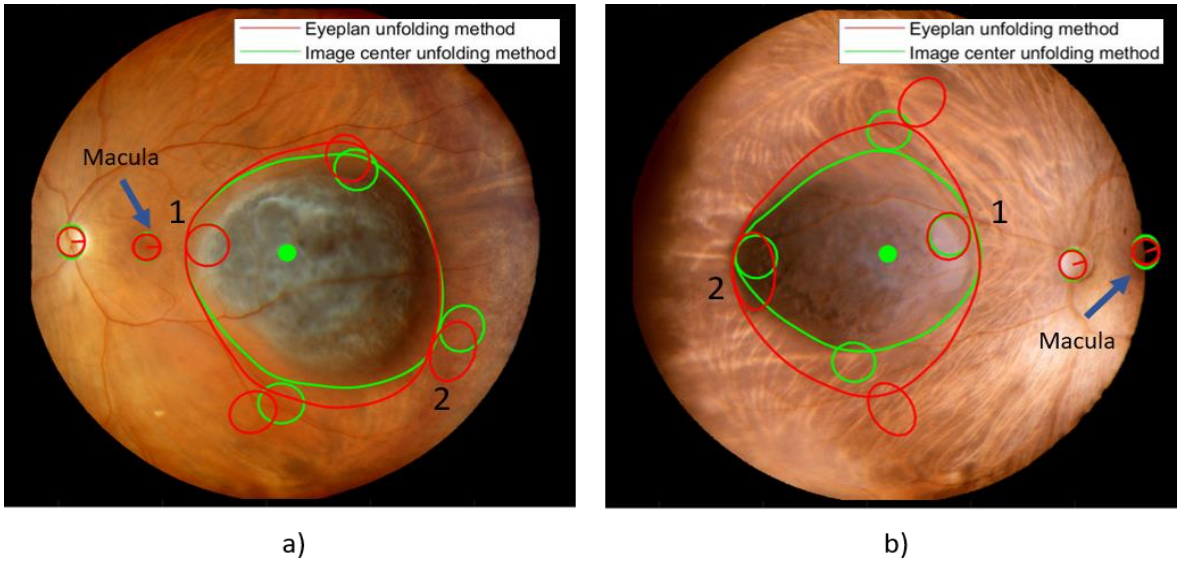

Figure 33- The projections of both methods are represented: the distortion that affects the clips is stronger in the fundus (b) with respect the fundus (a):the further is the macula from the image center, the more distorted are the structures.

4.2 MRI ocular imaging and registration with fundus photography

Building upon the implementation of the methods for model unfolding and modelling of the fundus imaging acquisition, the second part of this work of thesis focuses on the integration of fundus imaging information to a patient-specific model coming from MRI scans. Fusing the fundus with magnetic resonance imaging is an important step towards the creation of a more accurate eye model, combining the MRI information with the higher resolution provided by fundus photography. As already mentioned, MRI is probably insufficient as a standalone approach for eye modelling and tumor volume definition in ocular proton therapy. However, if moving towards a treatment workflow aiming at replacing clips implantation with non-invasive techniques, MRI is the starting point as already stated by Via and Daftari in their works (Via, et al., 2020) (Daftari, Aghaian, O'Brien, Dillon and Phillips, 2005). A proper integration of fundus photography is required especially for thin and flat tumors that are not visible in MRI scans. The fundus can provide important information about the tumor and, if present, the retinal detachment which could lead to a better tumor base definition.

4.2.1 Identifying ocular landmarks for fundus image registration on MRI images

In order to perform the registration between eye model and fundus, two common landmarks are necessary: in the previous chapter the optic disk and the macula have been used, because they are both visible in the fundus and because they are automatically generated as structures from EYEPLAN. As suggested by Zanet et al. (De Zanet, Ciller, Rudolph, & Maeder, 2010) the optic disk position can be reconstructed on MRI scans using the optic nerve structures: the intersection between the optic nerve head (ONH), i.e. the terminal part of the nerve attached to the eye globe, and the external scleral surface defines the optic disc. Then, the center-of-mass of this volumes is defined as the optic disc centroid. This approach has been

adopted in this work thus solving for one of the two necessary ocular landmarks on MRI scans.

On the contrary, the macula is not directly visible, but it can be located using other anatomical structures on MRI scan and its position can be analytically reconstructed using a priori-knowledge on the eye anatomy.

In the conventional approach for treatment planning in ocular proton therapy, the macula is located in the geometrical eye model at the intersection of the optical axis, i.e. the axis the passes through the lens and the eye center and the sclera surface. Then, the optic disk is defined as a point on the sclera surface on the equator plane passing through the macula position either on the left or right side according to which eye is modelled and at a fixed distance from the macula (4.4mm) (Jonas, et al., 2015). It is therefore fair to say that EYEPLAN approximates the position of both organs under quite generic assumptions on the eye anatomy that neglect any kind of patient specificity.

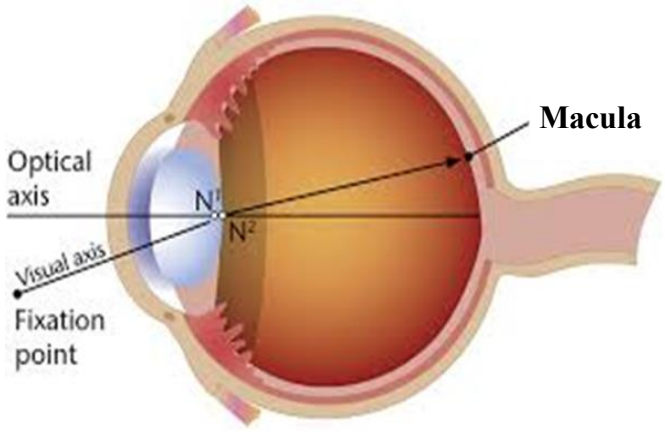

Figure 34- The real macula position is found at the intersection between the visual axis and the sclera surface.

There are several limitations in this approach: firstly, it is known from the literature that the visual axis, depicted in Figure 34, deviates from the optical axis by an angle alpha of about 3.93 ± 2.68◦ in the left eye and 3.91 ± 2.73◦ in the right eye (Schaeffel, 2002). It is also known that the macula to optic disk distance may vary between subjects between 4.0 and 4.8 mm.

In this work two approaches were investigated:

- The macula is generated on the MRI model using the 'EYEPLAN approximation', thus using the optical axis as a reference (in the Results section it will be called 'Geometric method')
- In the second one, an image-based method for macula identification that does not rely on strict assumption on population-based eye anatomy was developed, tested and compared to the previous one.

The first approach wants to evaluate the accuracy and the repeatability of the EYEPLAN approximation applied on the MR model. According to the EYEPLAN model, the macula in located at the intersection between the optical axis and the sclera surface. Once the macula position is defined, the unfolding (by using the 'image center' method) and the registration operations can be performed. This approach will be named 'Geometric method', as the macula definition accounts for the EYEPLAN approximations based on a geometric eye model.

The second approach aims to identify the invisible macula on MRI scans and to define an automatic and patient-specific method for MRI and fundus registration. This method, that will be explained in detail in the following sections, can be divided in three steps as illustrated in the Flowchart 3. Firstly, the macula position will be restricted in a limited retinal area (probability area). Secondly, a certain number of MR virtual images, each one for each macula candidate selected in the probability area, will be generated directly from the T1 and T2 MR volumes. Finally, the optimal macula is found by comparing each virtual image with the fundus photography through the Mutual Information metric.

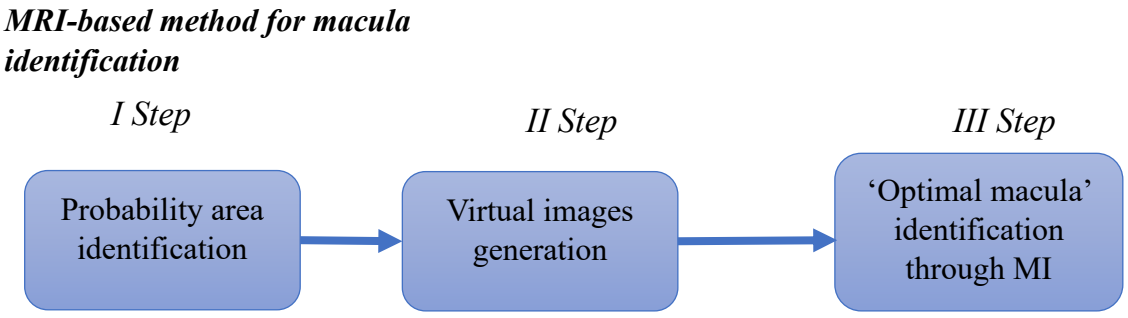

Flowchart 3- The Image based method for macula identification is composed by three blocks.

4.2.2 The macula probability area

As already mentioned, in order to find the macula in the eye model delineated on MRI scans, two anatomical constraints can be considered:

- Deviation between optical axis and visual axis by an angle α.
- Distance between macula and optic disk.

To minimise the reliance of the algorithm on predefined models unable to account for patient specificity in the first step of the proposed algorithm, only the first constraint will be considered. According to literature, the first constraint restricts the macula position to a ring-shape area on the internal eye surface given by its intersection to two cones. Both cones originate from the lens center and their axis is parallel to the optical axis. In the MRI model, the eye optical axis can be easily calculated as it passes through the center of the sclera and the lens center, which are structures easily recognizable on MRI images. The lens was modelled as an ellipsoid with a biconvex shape and its centroid estimated (see Figure 35 panel (a)). The angular aperture for the first is given by the minimum angle which is 3.93° - 2.68° for left eye or 3.91 - 2.73◦ for the right eye and for the second by the maximum angle 3.93° + 2.68° for left eye and 3.91° + 2.73° for right eye (see Figure 35 panel(b)).

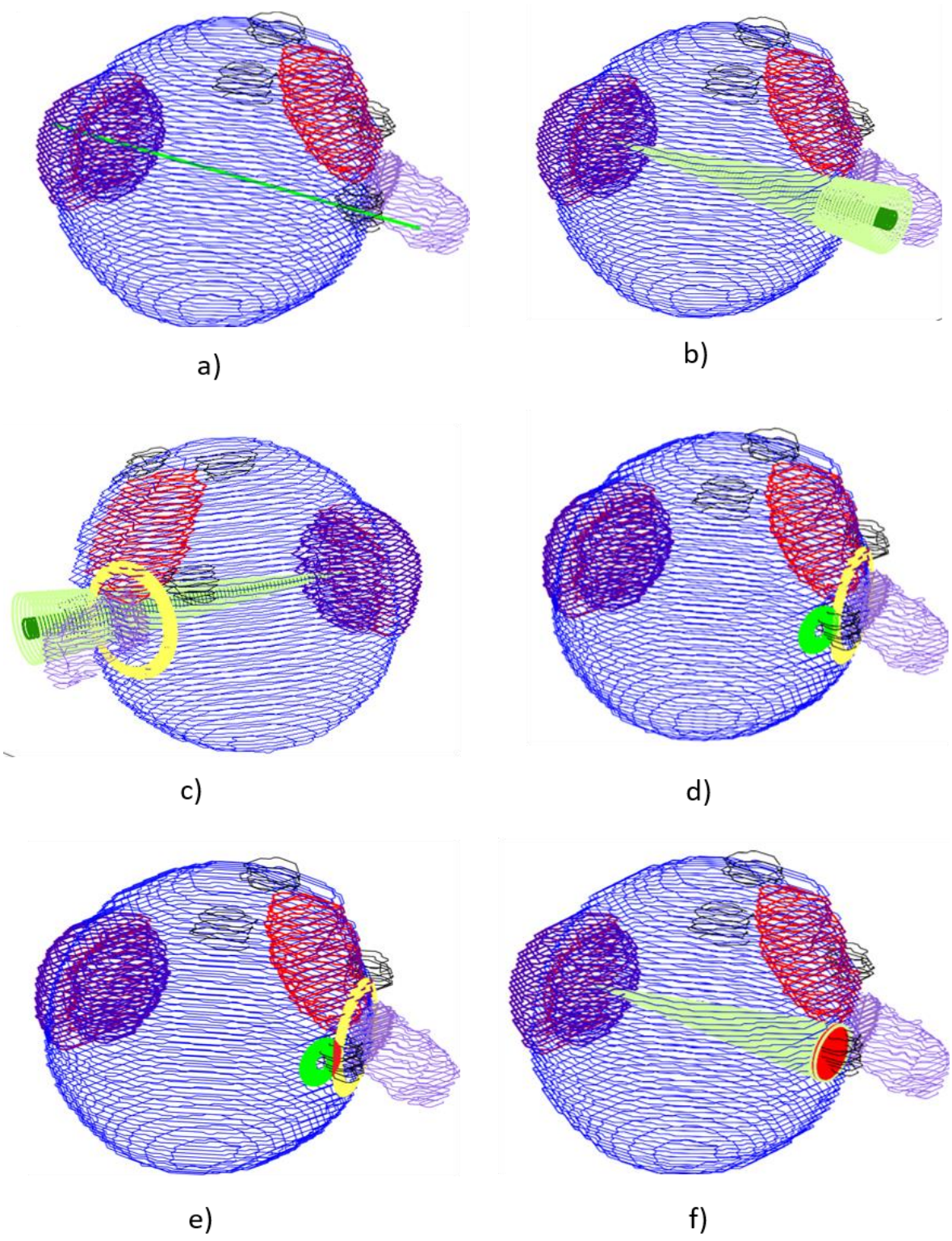

Figure 35- Macula probability area construction: (a) optical axis identification. (b) application of the first constraint: an inner (dark green) and an outer cone (light green) have been generated. (c) application of the second constraint: the ring shape yellow area has it center in the optic disk centroid. (d) this panel shows both the two ring-shape areas defined by the two previous constraints. (e) the intersection defines the real probability area. (f) the enlarged probability area.

Nevertheless, a second anatomical constrains based on optic disk to macula distance is available. This geometrically consists in the identification of another ring shape area defined by two concentric circumferences whose center is the optic disc centroid and whose radius is 4mm and 4.8mm, for the inner and outer one on the retina surface, respectively (panel (c) Figure 35). Finally, the intersection of the two ring shape areas defines the macula probability area (panel (e) Figure 35). It is important to point out that the resulting probability area has a constant probability distribution and each point has the same probability to be the optimal macula.

However, to rely as little as possible on assumption on the eye anatomy the probability area has been increased significantly with respect to what literature suggests. As such, the probability area is now defined by a single cone encompassing the optical axis and whose angle is 6.93 ° (3.93°+3°) visible in panel (f) of Figure 35. The resulting probability area dimension depends on the eye radius with increasing area value for greater eyes. In the Figure 36 the values of radius and area for the ten patients included in this study are shown.

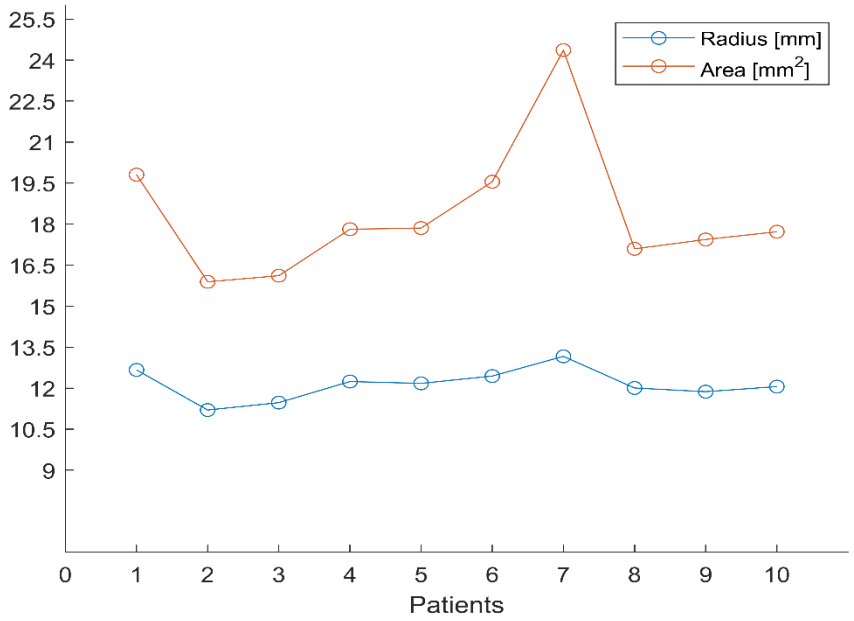

Figure 36- Relationship between the patient eye radius and the dimension of the macula probability area. The bigger the radius, the bigger the probability area.

As a result, 200 equally spaced potential maculas are identified in this area. It is important to underline that the area presents a uniform distribution: each point possesses the same probability value and the macula could be everywhere inside this area.

As already mentioned, it has been decided to consider as the 'effective probability area' the area given by only the first constraint, and for the moment to ignore the limitations introduced by the second. The second constraint will be used as validation of the process of image-based identification of the best macula amongst those belonging to the ‘effective probability area’: since an image-based metrics will be used to select the optimal macula within the probability area, the second constraint will serve as a figure of merit to evaluate the robustness of the algorithm.

4.2.3 MRI virtual fundus image generation

After having identified a probability area on the sclera surface where the macula can lie, it is necessary to establish its real position. This section wants two analyse the second step present in the Flowchart 3: The virtual images generation. In turn, this step can be divided in 3 blocks displayed in Flowchart 4.

After a pre-processing step (I block), a series of bi-dimensional images will be generated by considering the gray levels information content directly from the MRI volumes through a technique similar to ray tracing (II block). The ‘virtual images’ will be then compared according to the MI algorithm (III block), and the one that presents the highest similarity with the fundus identified the ‘optimal macula’.

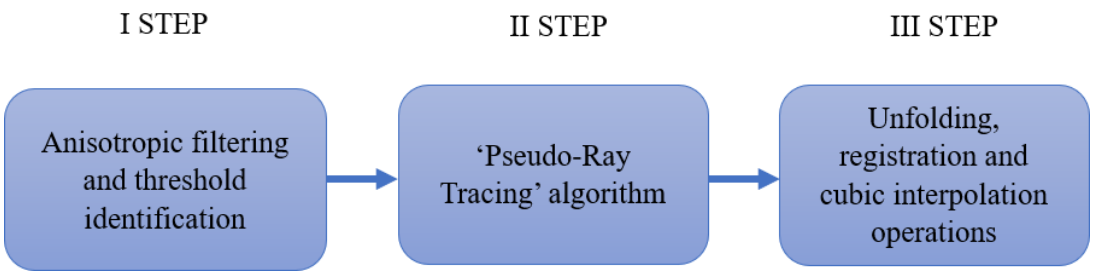

Flowchart 4- The virtual Images generation step can be divided into three sub-blocks.

The method will be comprehensibly presented only for the T1 weighted 3D MRI volume and in the last section will be described T2 volume.

4.2.4 Pre-processing

A. T1-weighted MRI pre-processing

As a pre-processing step, anisotropic filtering is applied to the image to remove noise. The noise in the vitreous humour is for most of removed, while preserving the edge between the retinal surface, the tumor and the vitreous humour. Figure 37 shows the same MRI slice before and after the anisotropic filtering.

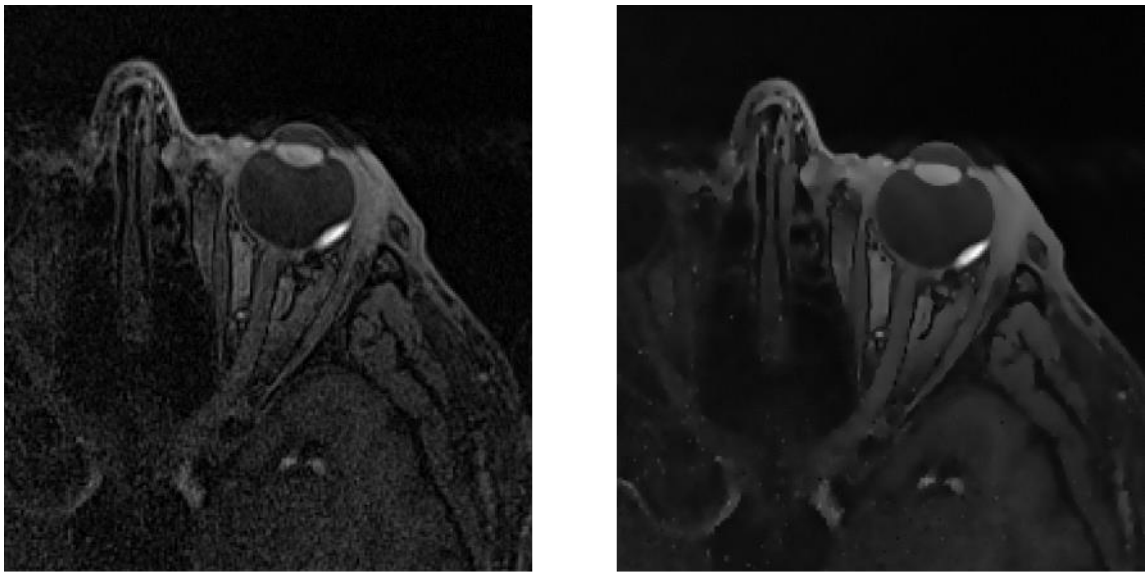

Figure 37- T1 MRI slice(a) at which an anisotropic filter has been applied (b).

To maximise the quality of the MRI virtual fundus images, a thresholding operation was designed aiming at filtering out the contribution coming from pixel that belongs to the humour vitreous and maximise those belonging to the lesion. Therefore, for each light ray only voxels in the tumor areas will play a role on the gray level assigned to the specific point on the retina. The threshold is defined considering the values of all voxels in the eye region

and excluding the information present in the entire volume of MRI. The histogram of the gray levels of this area is represented for two exemplary cases in Figure 38: the left and right panel respectively, represent two histograms for a medium-size tumor and a smaller tumor. In the first case (left panel) the histogram presents a specific distribution allowing to distinguish two main areas: the first correspond to low intensity voxels belonging to the vitreous humour, whereas the second, formed by the points that belong to the tumor, have a high signal intensity. The voxels belonging to the lens are responsible for a slight deflection of the curve in the intermediate bins of the distribution (gray level 100 to 125). In the second case (b), it is appreciable how the number of high intensity voxels is lower with respect to the first case. This is a clear consequence of the tumor volume being smaller. Nevertheless, it is still possible to recognise the signal generated by the lens, always in the medium bins, and the one that comes from the vitreous humour.

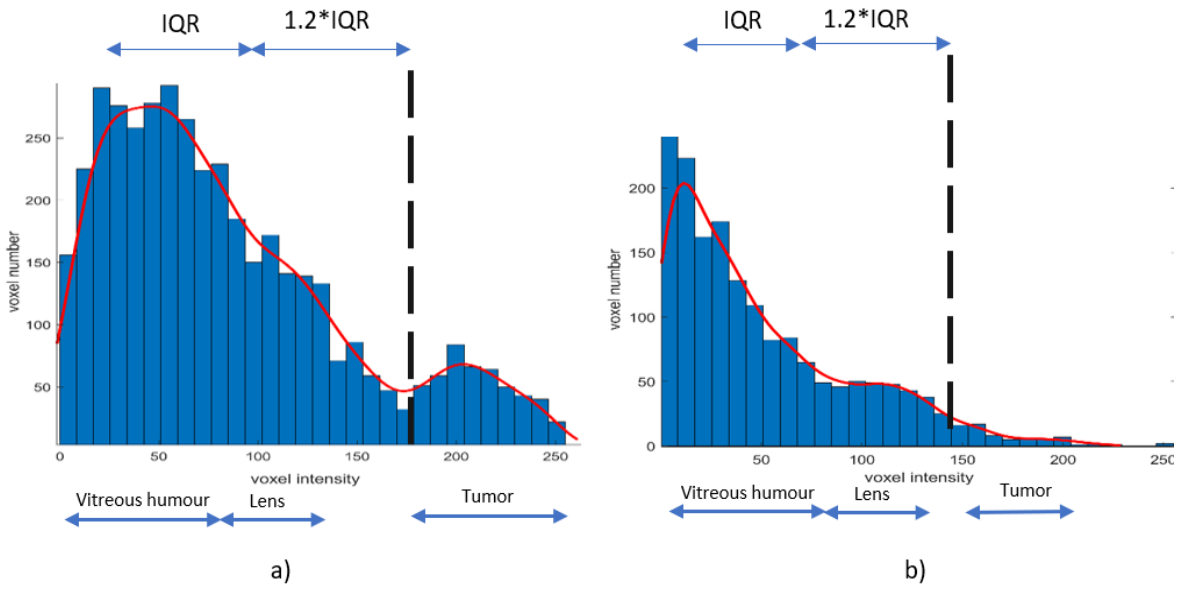

Figure 38-The gray level histogram for two different T1 MR volumes. In the case (a) the tumor is a medium size-one and its signal can be appreciated in the intensity histogram. In the case (b), the tumor is a small one and it can be hardly detected in the histogram.

To discriminate the voxels belonging to the tumor with respect to the others, it is necessary to define a threshold value by analysing the histograms. Median, 25th-percentice, 75th-percentile and interquartile range (IQR) are calculated. The median of a distribution is obtained by taking the [(n + 1) ÷ 2]th value, where n is the number of values in a set of data

that has been previously ranked (sorted in ascending order). The lower and the upper quartile are the elements in the position defined by the following formulas:

$$I_{25-th} = [0.25 \ + \ (n+1)]^{th}$$

$$I_{75-th} = [0.75 \ + \ (n+1)]^{th}$$

$$\text{IQR} = I_{75-th} - I_{25-th}$$

The following quantities are reported on the histograms. The optimal threshold was found empirically after several attempts. The one that has been adopted is given by the sum of the median value with the interquartile range multiplied by a factor z = 1.2:

$$T_{threshold} = Median \ + \ 1.2 \cdot IQR$$

This value is shown inside the previous histograms with a black dotted line. This empirical value allows a good distinction between the voxels belonging to the tumor and the ones belonging to other structures. It is important to specify that the signal intensity recorded by the MRI might vary from patient to patient and it is conditioned by other factors including the MRI sequence used and artefacts related to movements. It is therefore impossible to establish a single threshold that is valid for all cases and consequently consideration on the distribution of the gray levels in each case must be applied.

B. T2-weighted pre-processing

The same operations were also performed on the T2 weighted scans which were available for all patients included in the study. It should be noted that T1 and T2 volumes are rigidly registered using the Velocity software (Varian, USA). Once the Velocity roto-translation matrix applied in the registration is retrieved, it can be applied on contours on the T1 image (the reference) to obtain the corresponding structure contours on the T2 volume. Then, the process of generating virtual images can be re repeated using T2 volumes. It is important to point out, however, that the intensity level of the same organ vary from T1 and T2 scans and therefore slight adaptations on the algorithm were required. The main difference is in the definition of the voxel threshold value based on analysis of the intensity level histogram of the eye region. Before identifying the threshold on T2 images, an anisotropic filter is applied to the volume to remove most of the noise present in the vitreous humour. Figure 39 shows a slice of the T2 volume before (a) and after (b) the application of the anisotropic filter. Figure 39(c) is a magnification of the eye region identified on the complete volume (orange area) and shows the retina points and the lens center from where the rays originate, in the same fashion as previously explained. The histogram in Figure 39 (d) illustrates the voxel values distribution for T2 scans. It is evident that the distribution differs greatly from that of volume T1. However, it is possible, also in this case, to recognize two main areas: the first one, with a low intensity signal, corresponds to the tumor and the lens (lens and tumor have similar intensity values on T2 scans Figure 39 (c)) and the second one, characterized by a high intensity signal, is produced by the vitreous humour.

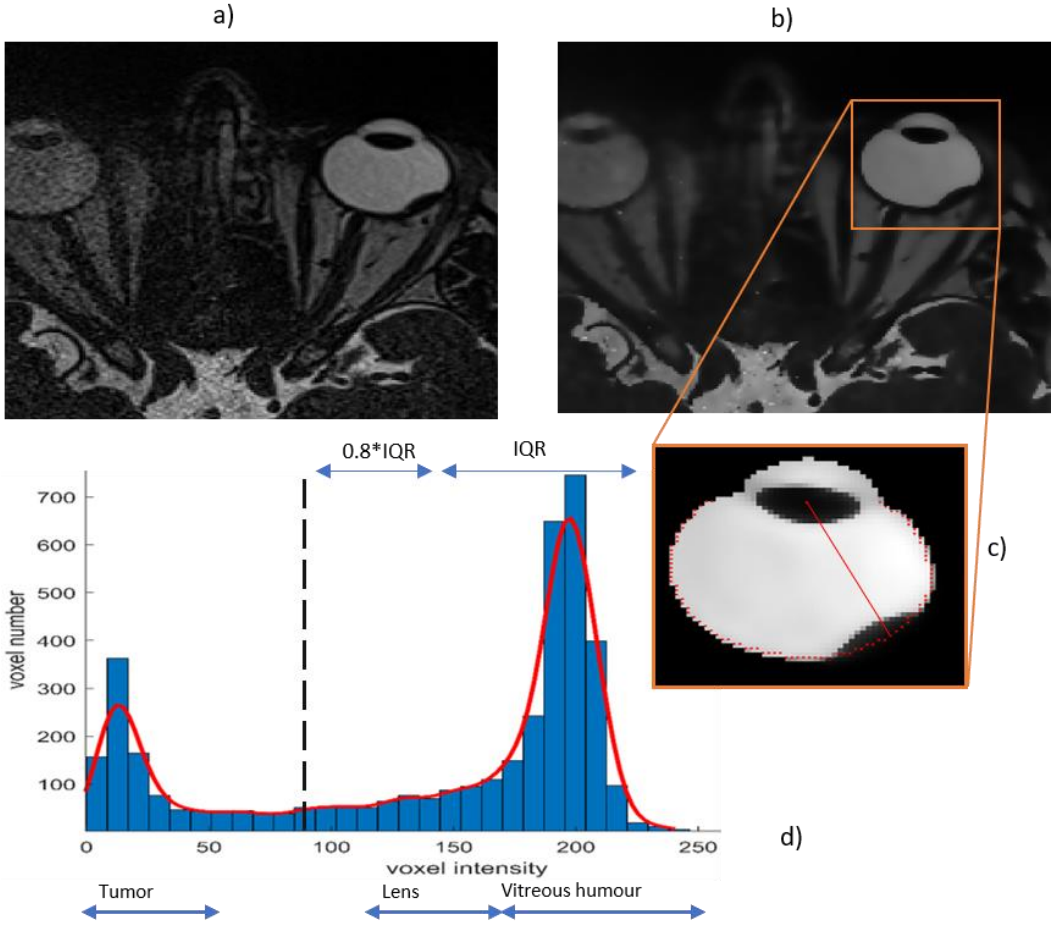

Figure 39- T2 MRI slice before (a) and after (b) the application of an anisotropic filter. A zoom on the eye (c) on which the intensity histogram (d) is calculated. The tumor signal is highly visible.

Median, 25th percentile, 75th percentile and IQR are calculated and the $T_{threshold}$ for T2 scans and virtual image generation is defined as follows:

$$T_{threshold} = Median - 0.8 \cdot IQR$$

This value is show in Figure 39 (d)) as a black dashed line. Several attempts have been made to detect the T2 $T_{threshold}$ and it is noteworthy to highlight that also for T2 it is impossible to establish a single threshold valid for all the cases.

4.2.5 MRI-based ray tracing algorithm

After having explained the first block present in Flowchart 4, let's come to the second one. The operation that will assign to each point belonging to the retina a given gray level value is performed by a technique similar to ray tracing algorithm. In computer graphics, ray tracing is a rendering technique for generating an image by tracing the path of light as pixels in an image plane and simulating the effects of its encounters with virtual objects. Applying this to volumetric medical images such as MRI scans of the eye requires some slight variations. In order to extract the information from the MRI volume, it is necessary to use the gray level values of the voxel that are intersected by the ray of light. The light rays that allows the acquisition of the fundus pass through the patient's eye lens, reflect on the retina and return to the camera through the lens again. To be as faithful as possible on how the fundus is acquired, the center of the lens is taken as the origin point of all rays pointing in the direction of the retina. Although the algorithm is performed in the same way for the T1 and T2 volumes, it is necessary to consider the differences in term of gray levels between T1 and T2, as in T1 the desired information is brought by high signal whereas in T2 is brought by low signal.

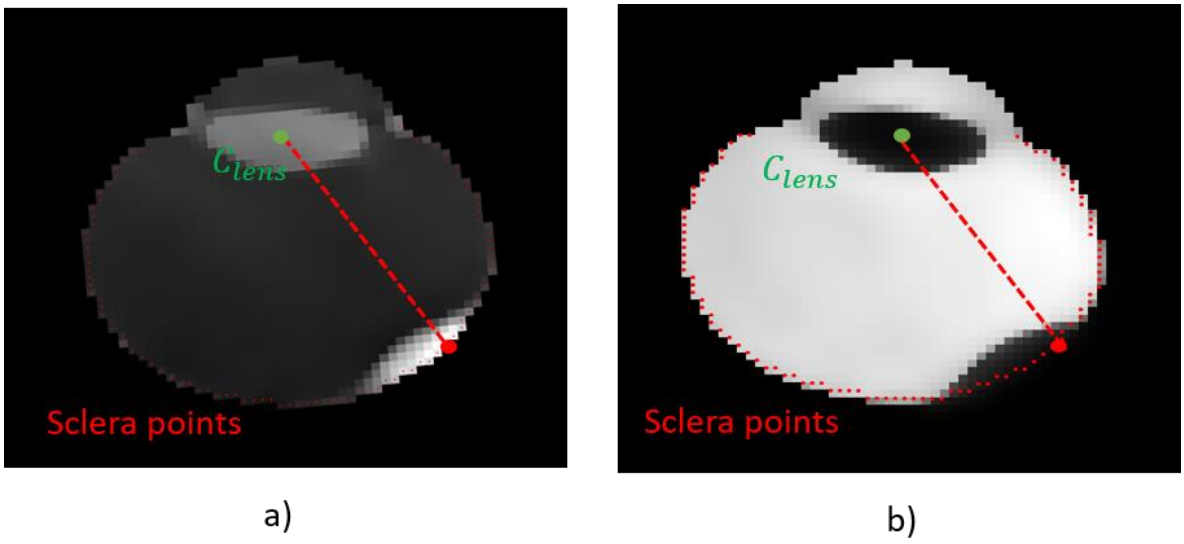

Figure 40-Schematic representation of one ray that connects the lens center with one arbitrary sclera point for T1 (a) and for T2 (b). This line crosses several voxels and in order to attribute a given gray level to the sclera point, each voxel is evaluated.

For each point belonging to the sclera surface, a line connecting it to the center of the lens C_{lens} is drawn and each voxel crossed is evaluated, as depicted in Figure 40: if its gray value is greater or lower than the threshold $T_{threshold-T1}$ or $T_{threshold-T2}$, respectively, the voxel will contribute to the final gray intensity value of the retina point. The sum of all the intensities above (for T1-w) or under (for T2-w) the respective threshold is attributed to the point P_{retina} on the retina.
Let's consider:

$$C_{lens} = [C_x \quad C_y \quad C_z]^T$$

$$P_{retina} = [P_x \quad P_y \quad P_z]^T$$

The direction versor and the voxel distance between these two points are calculated:

$$V_{ray} = \frac{C_{lens} - P_{retina}}{||C_{lens} - P_{retina}||}$$

N_voxels= $||C_{lens} - P_{retina}||$

This distance represents how many voxels are encountered by the single ray of light crossing the retinal surface and the following equation allows to move along the line:

$$P_i = C_{lens} + V_{ray} \cdot i \qquad\qquad i = 0,1, \dots, N\_Voxels$$

Where i is therefore a one voxel step along the ray of light. However, the point P_i, located along the line, will not, in most cases, precisely correspond to the center of a single voxel but will lie in a certain position inside it. Supposing that the point P_i falls as depicted in Figure 41, it is clear that, as it is not precisely located in the voxel center Ci, assigning to this point the intensity value of voxel Ci would be erroneous. As such, a simple neighbouring technique is applied. The intensity of the point P_i is established by evaluating the three

closest voxels intensity, that in this case are the centers C_i, C_c and C_f. A weight, inversely proportional to the distance to point P_i is assigned to each of the three voxel. Specifically, the distances $P_i - C_i$, $P_i - C_c$ *and* $P_i - C_f$ are calculated, inverted and assigned to a vector S which, once normalized, represents the weights.

$$S=\left[\frac{1}{||P_i-C_i||} \quad \frac{1}{||P_i-C_c||} \quad \frac{1}{||P_i-C_f||}\right]^T$$

$$S_{norm} = \frac{S}{||S||}$$

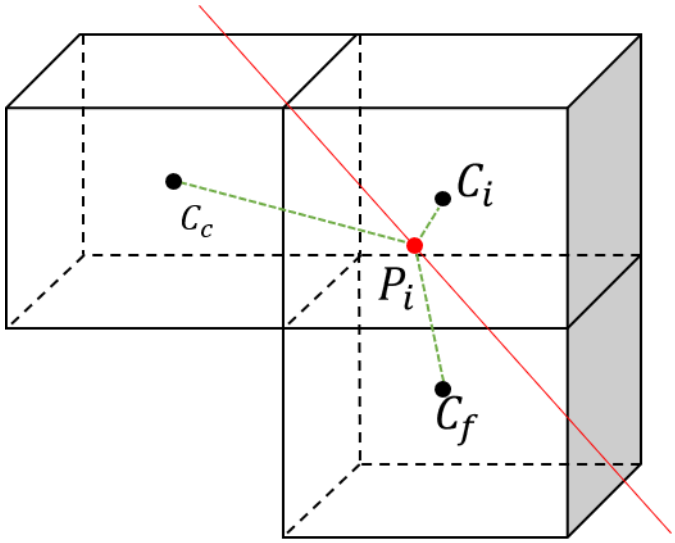

Figure 41- schematic representation on how the three closest voxels contribute in the gray level evaluation. The light ray is represented by the red line.

In summary, the intensity value given to P_i is given by the weighted sum of the values of the three closest voxels multiplied by the weight vector. If this value is greater (T1-w) or lower (T2-w) than the respective threshold, it will contribute to the overall value assigned to the point on the retinal surface. Iteratively, the procedure is repeated along the ray of light until the counter i reaches the value of N_voxels. If any voxel along the ray of light hasn't contributed for the assignation of the gray level value, the median value is set for the P_{retina}.

The algorithm repeats the following operations for all points belonging to the retina and lastly, the gray levels are normalized in the range [0.1].

Since the evaluation of the intensity is performed starting from the lens and since, in T1, the lens has a higher signal than the humour vitreous, it is necessary to ignore its volume as it might result in unwanted features on the resulting virtual image. Also in T2 the nullification of the lens signal is performed as this structure is detected as a low signal. The elimination of the lens is achieved by assigning to every voxel belonging to this structure the median intensity value over the entire eye region.

Once the execution of the algorithm is done, each point of the sclera possesses a given gray level value that ranges in the interval [0,1]. The results for both T1 and T2 MR models are shown in Figure 42.

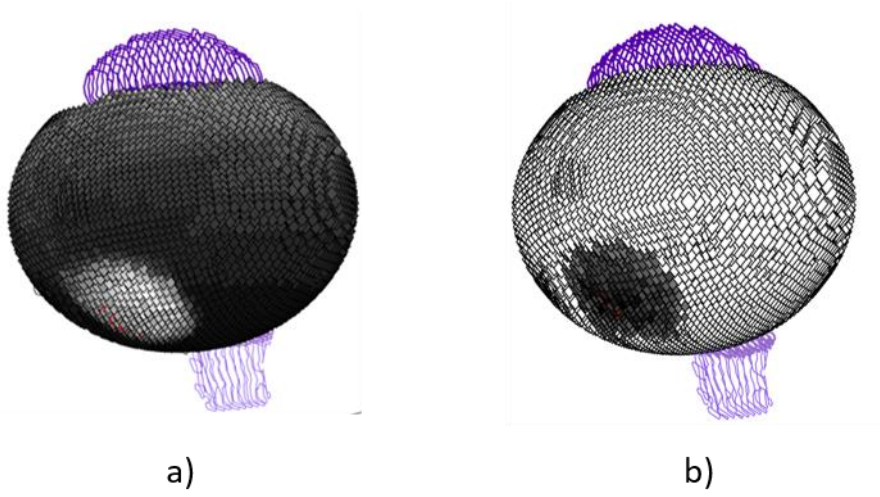

Figure 42- To each point belonging to the sclera, a gray level value is assigned. Panel (a) shows the result of the operations for T1 volume while panel (b) for T2 volumes.

4.2.6 MRI virtual images unfolding, registration and interpolation

The points of the retina will be added to the MRI model and during the unfolding operations they will be projected, in the same way as any other structures on the eye model, and registered with the fundus using any combination of macula and optic disk. For this part of the study, the unfolding procedure uses the 'projection center' method, explained in previous chapter. This results in a distribution of points and corresponding gray levels superimposed to the fundus photography. At this point it is necessary to create a gray-level image that will be compared with the fundus using an image-based metric.

To proceed with the generation of the n-virtual images, one for each macula belonging to the probability area, it is necessary to transform a discrete distribution of points to a bi-dimensional image with the same resolution of the underlying fundus photography. The Figure 43 (a) shows the retinal points (in purple) distribution upon the fundus photography after the unfolding and the registration step for a randomly selected macula.

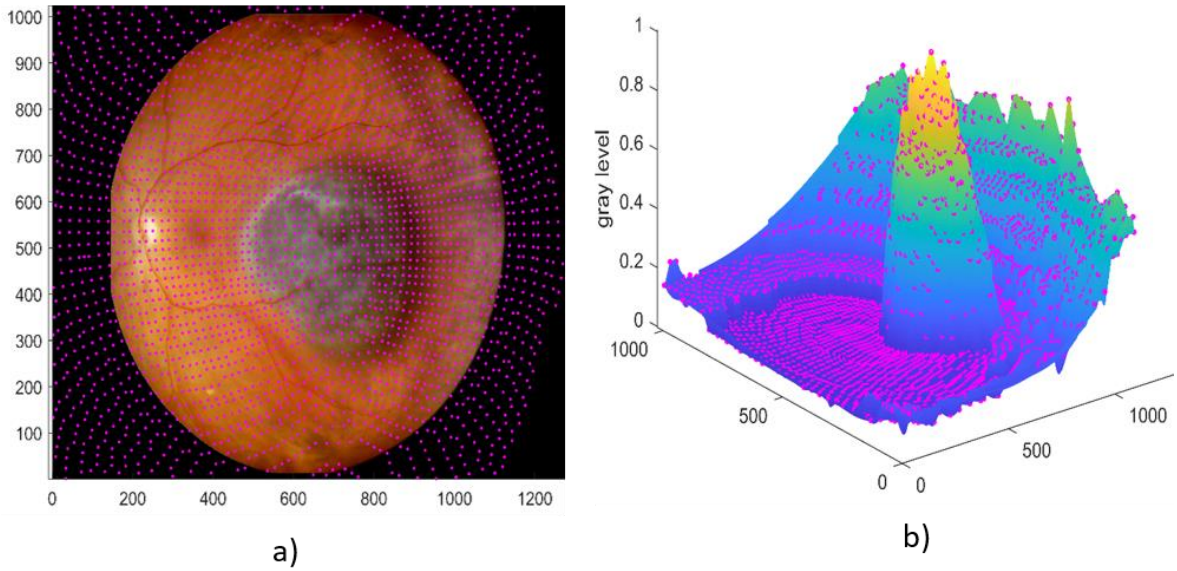

Figure 43- (a) The sclera points belonging to a random macula unfolded model are registered with the fundus. (b) the generation of an image in the same size of the fundus photograph is obtained after a cubic interpolation step.

The generation of a virtual image having the same dimensions as the fundus is achieved by means of cubic interpolation. This requires as input the gray levels and coordinates

associated with each point. Figure 43 (b) shows the same points of the figure (a) with the third dimension corresponding to intensity values. The interpolation allows assigning a level to all 1024x1280 pixels and obtain the virtual image. The Figure 44 shows two exemplary virtual fundus images generated on T1 scans on one patient using two different maculas inside the probability area. It can be seen how the position and size of the feature on the image can vary: the choice of the macula influences the conversion factor K and the roto-translation matrix R thus producing significantly different virtual images.

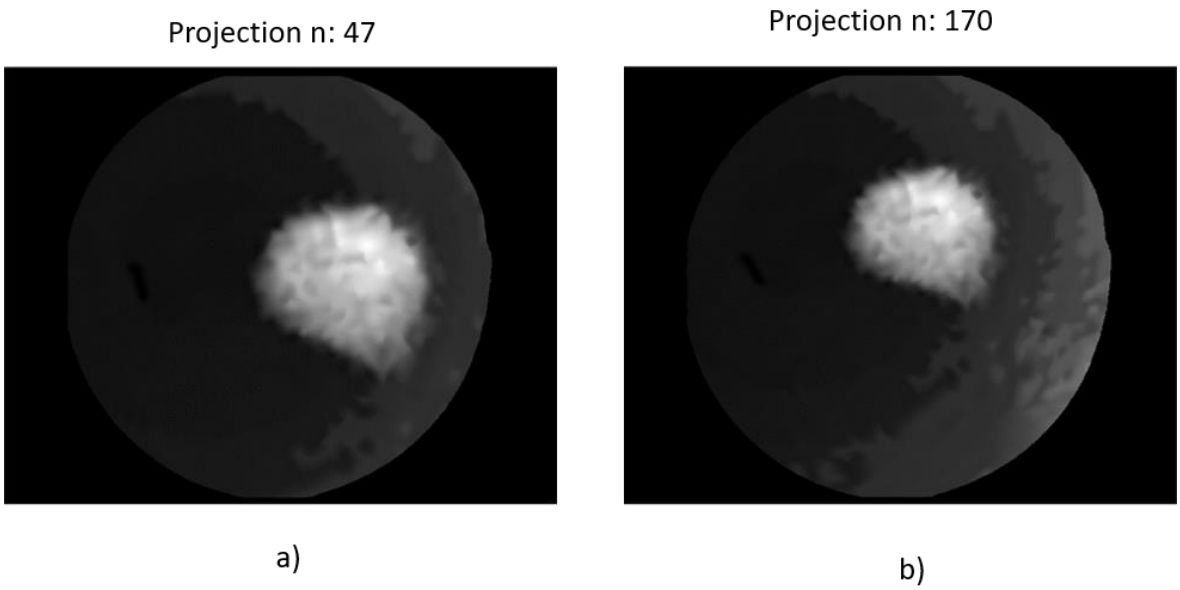

Figure 44-Among the 200 virtual images, the projection n°: 47 (a) and n°:170 (b) are shown. Tumor size and position varies according to the relative position of the macula with the other structures in the 3D model.

The virtual images generation for T2 scans follows the same steps outlined for T1 scans. Examples of virtual T2 images are represented in Figure 45 below.

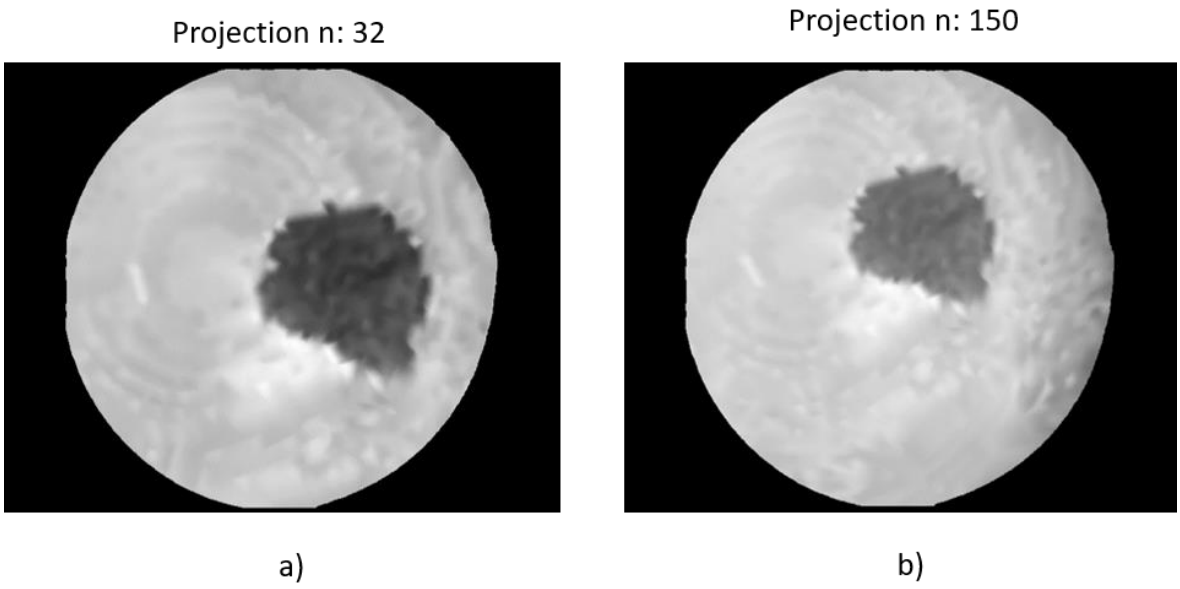

Figure 45- Examples of T2 fundus virtual images. The tumor is perceived as a low signal area.

4.2.7 Optimal macula identification through mutual information

The next step of the algorithm (III step of Flowchart 4) is the selection of the optimal macula amongst the two hundred candidates in the probability area. The approach that has been evaluated uses mutual information (MI) as a measure of image similarity between the Panoret fundus image and the registered virtual fundus image generated from the intensity levels in the MRI volume. Mutual information is a metric widely used in the biomedical field to register images of the same anatomical structures acquired using different modalities that therefore present different properties but similar information content. In this specific case, the common information shared by fundus photography and virtual MRI based retinal imaging is the retina surface and the tumor. Amongst all 200 macula candidates, each corresponding to one specific virtual image, one will present the highest MI coefficient. Thus, this macula can be selected as the optimal macula.

Once the set of virtual images has been generated it is possible to proceed with the evaluation of the mutual information. The Mutual Information between two images essentially measures the amount of information that one image shares with the other. The Mutual information (MI) coefficient is given by the difference between the sum of the entropies of

individual overlapping images and the joint entropy of the combination of those. In other words, it is a measure of the reduction in uncertainty about one image due to the knowledge of the other. No prior functional relationship between the images is assumed however MI relies on the capability to capture a statistical relationship between images through the analysis of the images' joint entropy.

In the following paragraph, a brief definition of the mutual information coefficient is provided.

The entropy H(X) for a discrete random variable X, is defined as

$$H(X) = -\sum_{x} p_X(x) \cdot log\ p_X(x)$$

where p(x) is the probability density function of the variable. Entropy is always a finite, positive number for discrete random variables and has a maximum value in the case of a uniformly distributed variable. In the case of an image, entropy describes the total amount of information. The joint entropy H(X,Y) for a pair of random variables X,Y with joint distribution p(x,y) is defined as

$$H(X,Y) = -\sum_{x,y} p_{XY}(x,y) \cdot log\ p_{XY}(x,y)$$

In addition, the conditional entropy of a random variable X given the random variable Y is expressed as

$$H(X|Y) = -\sum_{x,y} p_{XY}(x,y) \cdot log\ p_{XY}(x|y)$$

The chain rule for two variables is expressed as

$$H(X,Y) = H(X) + H(Y|X)$$

The common information shared between two random variables X,Y is expressed by the mutual information that is defined as

$$MI = H(X) + H(Y) - H(X,Y)$$

Mutual Information can be interpreted as a measure of the statistical dependence between X and Y. The above quantities are schematically illustrated by the Venn diagram of the Figure 46.

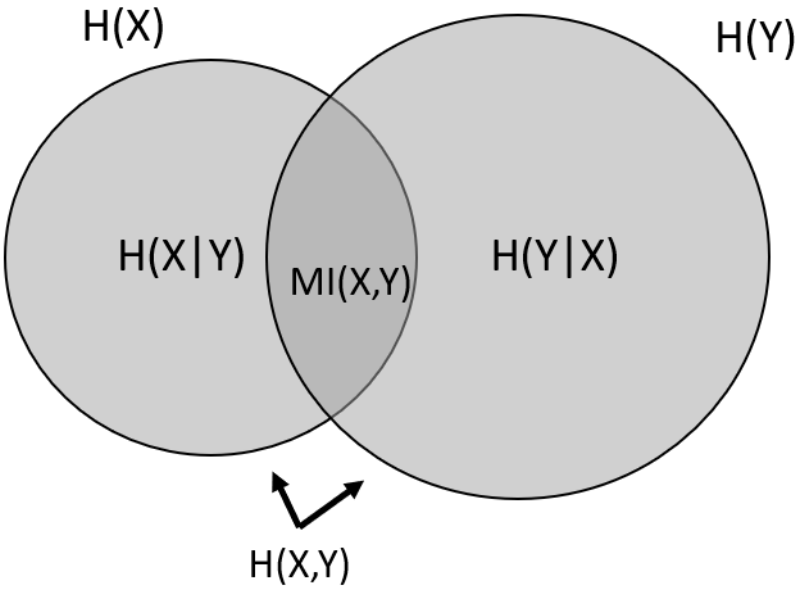

Figure 46- Venn diagram of the relationship between entropy and mutual information. The mutual information MI (X, Y) corresponds to the intersection of the information in X with the information in Y.

The mutual information coefficient is calculated for each of the virtual images created using different macula candidate. The goal is to establish which of the n-virtual images maximises the mutual information by minimizing the joint entropy. However, before calculating the MI, some pre-processing must be performed on both fundus image, virtual and original.

Several attempts, resumed in Table 1, have been done to establish which was the best pre-processing to be applied to the fundus in order to obtain, during the MI, the most consistent and robust output possible.

Attempts	*Colour Domain*	*Channel Selected*	*Pre-Processing Operations*
1	RGB	Gray level	Complement
2	HSV	'S'	Complement
3	LAB	'A'	Closing + Median filter + Cropping + Thresholding + complement

Table 1-The principal pre-processing operations are resumed for each attempt that have been tested.

Because the virtual images are expressed in gray level values, in the first attempt we converted the RGB fundus image in a gray level image and we computed the complement. The first fundus used in as input for the MI calculation is shown in the Figure 47 (b).

The second attempt wanted to explore the HSV colour domain. The HSV colour domain is composed by three channels: hue, saturation, and value:

- Hue (H) is the colour channel, in which each colour is represented in represented
- Saturation (S) describes the amount of gray in a particular colour, from 0 to 100 percent
- Value (V) works in conjunction with saturation and describes the brightness or intensity of the colour, from 0 to 100 percent

For the second fundus pre-processing attempt, the saturation channel has been selected and its complement has been computed. The resulting image is shown in Figure 47 (c).

It is visible in the images (b) and (c) that in the pre-processed fundus images, structures such as the blood vessels irrorating the retina, for instance, are still highly visible and they possess a high information content. On the other hand, these same vessels are not recognizable on MRI scans because of their dimensions being much smaller than the resolution achievable with MRI. Thus, the procedure adopted in the third attempt for pre-processing the fundus photography aimed at the elimination of the vessel network.

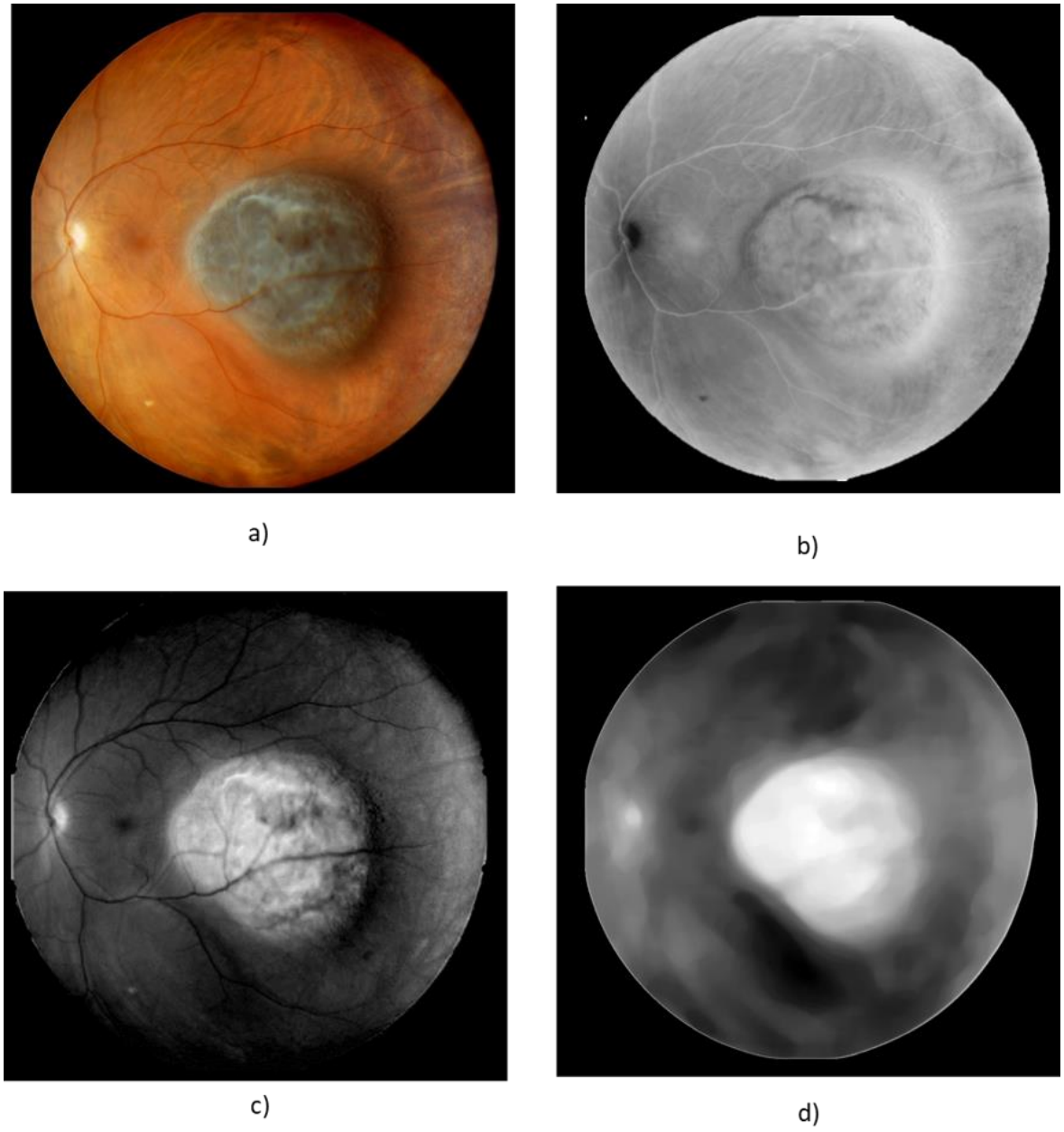

Figure 47- (a) The original fundus image. (b) complement of the gray fundus image. (c) complement of the channel S (HSV colour domain) of the fundus image. (d) complement of the channel a (LAB colour domain) of the original fundus image with the application of a closing procedure.

Additionally to the blood vessels removal, another image domain has been explored: the CIELAB domain. The CIELAB colour space, also known as CIE L*A*B*, is a colour space designed to approximate human vision in which colours are expressed as three values:

- L channel expresses the lightness: it goes from 0, which expresses the darkest black, to 100, which represents the brightest white
- A channel represents colours from green (−) to red (+): it ranges from -100 to +100
- B channel represents colours from blue (−) to yellow (+):it ranges from -128 to +127

For the last fundus image pre-processing, the channel 'A' is selected and a morphological closing procedure is applied using a flat disk-shaped structuring element with a radius R=5. The closing operation dilates an image and then erodes the dilated image, using the same structuring element for both operations. Morphological closing is typically used for filling small discontinuities in an image while preserving the shape and size of the objects in the image. Then, on the resulting image, a median filtering of dimension (50x50) is used to reduce the noise. Finally, the complement of the image is computed (see Figure 47 (d)).
To speed up and make the algorithm more precise a cropping operation has been applied to the fundus image and the to all the virtual images. Because the common information is brought by the tumor in terms of dimension, size and position, in both the fundus photography and all the virtual images, the tumor information is extrapolated by setting some empirical thresholds (see Figure 48 (c) and (d)). Of course, the thresholds for the T1 and T2 images are different. The mutual information inputs are the images shown in (c) and (d): all the background information is removed in both the images and the similarity between the resulting images is evaluated by comparing only the tumor information content. In this way the structures like macula, optic disk, and possibly some vessel network residual, cannot affect the MI analysis.

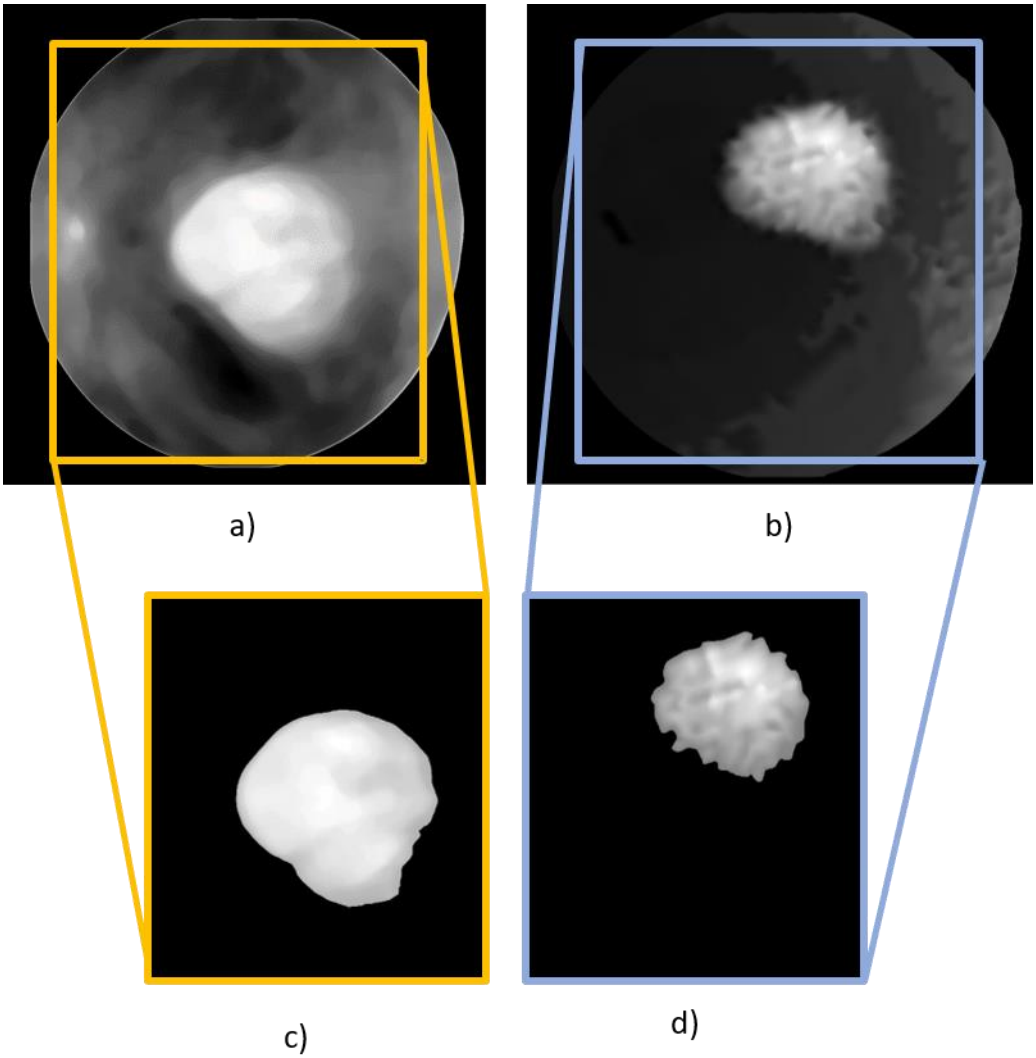

Figure 48- (a) Pre-processed fundus in which: the channel 'a' is selected, a morphological closing procedure and a median filter (50x50) is done. (b) one out 200 virtual images. Selection of a Region Of Interest (ROI) by a cropping and a thresholding operations for the fundus (c) and the virtual image (d) respectively.

4.2.8 Evaluation of the macula selection

After having identified the probability area and having selected a certain number of macula candidates, the virtual images have been generated. The optimal macula is identified by comparing the pre-processed fundus with each pre-processed virtual image through the MI. a typical MI output is shown in Figure 49:

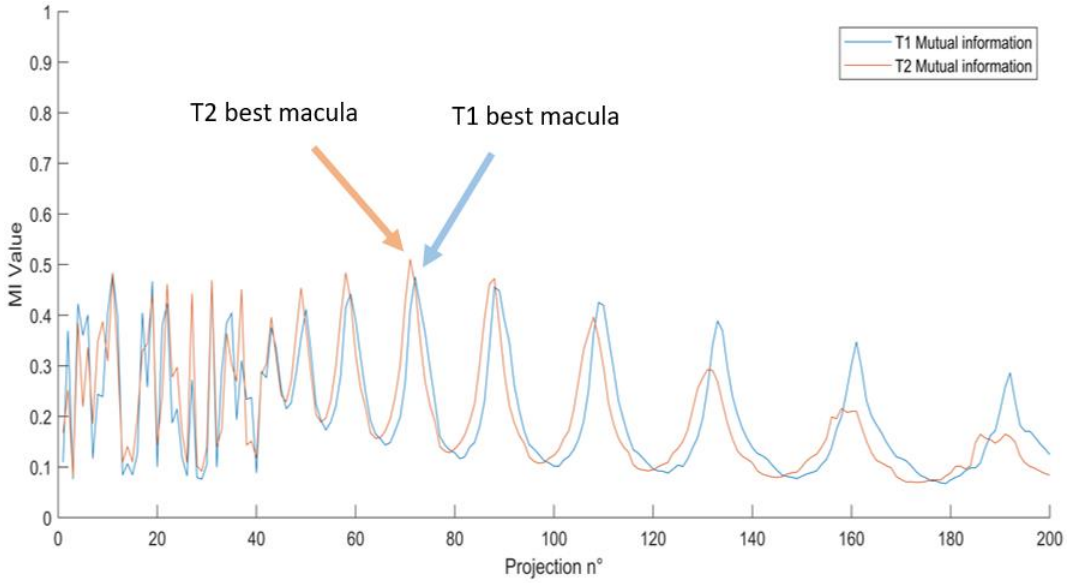

Figure 49- Each virtual image possesses a given MI coefficient according to the common information between the fundus photography and the considered virtual image.

The virtual image that presents the highest mutual information coefficient, belongs to a given projection which has been generated by a certain macula. However, the selection of this macula is dependent on the performance of the mutual information coefficient in determining which virtual image better matches the original acquired with the Panoret system. Thus, the definition of a metric to evaluate the performance of the MI was required. This metric is the distance between the macula and the optic disk.

According to literature, in an average human eye, the distance between these two ocular organs should be between 4.0 and 4.8 mm. Each macula candidate is a specific point on the retinal surface of the MRI based 3D eye model and therefore as a different distance with respect to other candidate with the optic disk which, on the contrary, is fixed. Thus, the

proposed algorithm evaluates whether the macula identified as the optimal one using MI satisfies the constraint of optic disc-macula distance. If this is not the case, that virtual image is discarded and the one presenting the second highest MI is selected. This procedure is iteratively repeated until the macula with the highest value of MI that satisfies the anatomical requirement of distance to the optic disk is found. In Figure 50 all the projected base contours for all the macula candidate are presented for an exemplary patient. It is possible to distinguish 2 different trends which occur in the contour projections: size variation and position variation. The conversion factor K is responsible for the first behaviour: it is defined as the ratio between macula-optic disc distance in fundus and macula-optic disc distance in MRI projection. The numerator is fixed because the distances in the fundus do not change but the denominator changes according to the selected macula. If, during the n-projection, the n-macula is closer to the optic disc, the optic disc-macula distance is lower and the K factor is bigger resulting in a larger boundaries. If the n-macula is further from the optic disc, the distance is bigger, the ratio is lower, and the boundaries are smaller. The second trend depends on the relative position between macula and optic disk and the orientation of the vector connecting the two.

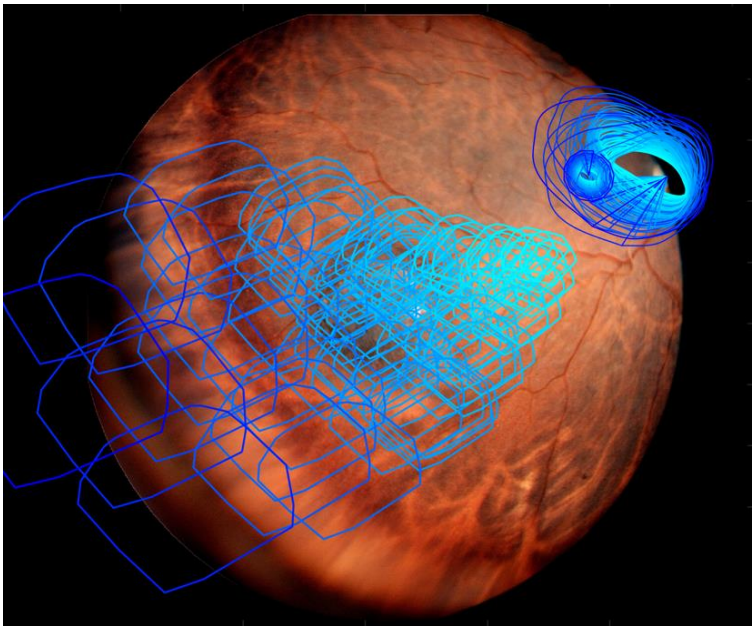

Figure 50- All the projected tumor base for each macula. Position and dimension vary according to the relative position between the macula and the other structures in the 3D model.

5 Quantitative evaluations

The definition of a macula and an optic disk on the three-dimensional eye model enables the application of the unfolding and back projection procedures. As a result, any structure included in the eye model can be projected on the unfolded plane and consequently registered to the fundus images. The introduction of the 'image center' method slightly varies the procedure but maintains the overall rationale: fusing a three- dimensional eye model and a fundus image requires a definition of a macula and an optic disk.

As a result of this, any structure on the 3D eye model can be compared to structure delineated on the fundus photography. All novel methodologies introduced in this work of thesis has been evaluated using this procedure. In particular, the structure corresponding to the base of the tumor in the EYEPLAN or MRI model has been evaluated, to the manual delineation of the lesion base performed by a radiation oncologist on the fundus photography. In particular:

- The 'image center' method was evaluated by comparison with the traditional unfolding procedure embedded in EYEPLAN using the contours of the base in the geometrical eye model of EYEPLAN
- The image-based method of fundus registration with MRI has been compared to a replica of the EYEPLAN definition of the macula that places the macula along the optical axis on the MRI model that we have previously called 'Geometric projection'

The resulting projection of the tumor base, either coming from EYEPLAN with or without the 'image center' or MRI with or without image-based macula selection was compared with the manual delineation. This was performed using several metrics for bi-dimensional feature comparison:

Firstly, the Dice Similarity Coefficient (DSC) was used. The DSC is a spatial overlap index and a reproducibility validation metric. The value of a DSC ranges from 0, indicating no spatial overlap between two sets of binary segmentation results, to 1, indicating complete overlap and is defined as

$$\mathrm{DSC} = \frac{2 * (|X \cap Y|)}{|X| + |Y|}$$

where |X| and |Y| are the cardinalities of the two sets (i.e. the number of pixels in the two images). The DSC equals twice the number of elements common to both sets divided by the sum of the number of elements in each set. For example, let's consider the case shown in the Figure 51:

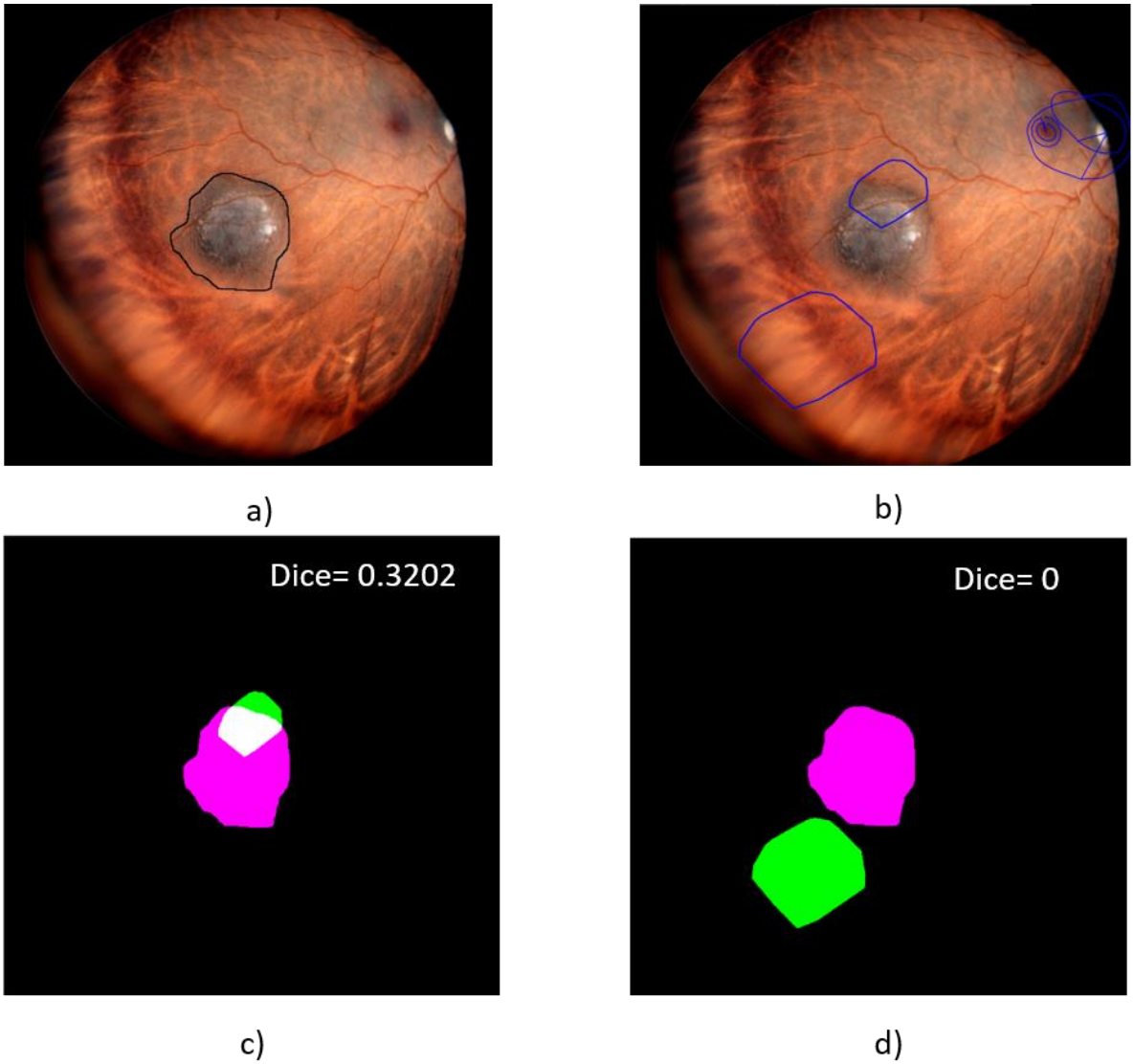

Figure 51- (a) Tumor segmentation performed by a radiation oncologist. (b) Two random projections. (c) DSC calculation for the first projection: the DSC value is greater than 0 because the tumor delineation and the projection are superimposed. (d) There is no superposition and the DSC=0.

Figure 51 (a) depicts the tumor segmentation and Figure 51 (b) shows two random projections. One is slightly superimposed on the tumor and the other is at a very different location. In the first case the DSC value is greater than zero whereas in the second case, given that there is no superimposition between the two areas, the DICE value is equal to zero.

The second index that has been used is the JACCARD index. It measures similarity between two sets and is defined as the size of the intersection divided by the size of the union of the sample sets. It ranges, as the DSC, from 0 to 1.

$$J = \frac{|X \cap Y|}{|X \cup Y|} = \frac{|X \cap Y|}{|X| + |Y| - |X \cap Y|}$$

Then, the Overlapping Coefficient (OVL) or Szymkiewicz–Simpson coefficient, is a similarity measure that measures the overlap between two finite sets and is defined as the size of the intersection divided by the smaller of the size of the two sets.

$$OVL = \frac{|X \cap Y|}{\min(|X|, |Y|)}$$

and the centroid distance (CD) are used. The Hausdorff distance metric measures how far two subsets are from each other: two sets are close in the Hausdorff distance if every point of either set is close to some point of the other set. The Hausdorff distance is the greatest of all the distances from a point in one set to the closest point in the other set.

Let X and Y be two non-empty subsets, the Hausdorff distance $d_H(X, Y)$ by

$$d_H(X, Y) = \max\{\sup_{x \in X} \inf_{y \in Y} d(x, y), \sup_{y \in Y} \inf_{x \in X} d(x, y)\}$$

Where sup represents the supremum and inf the infimum. Because it is a distance, it can be greater than 1 and can range to infinite if the two subsets are not bounded.

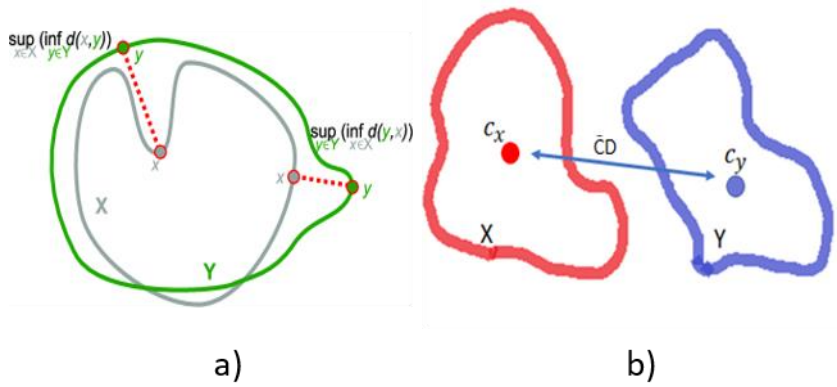

Figure 52- Hausdorff distance (a) and Centroid distance (b) between two subset X, Y.

The last parameter is the centroid distance and it calculates the distance between the centroids of the two subsets X, Y.

$$CD = d\left(\frac{\sum^{n} x_{x\in X}}{n}, \frac{\sum^{k} y_{y\in Y}}{k}\right)$$

Finally, the results obtained with the coefficients just introduced have been analysed through a statistical test. Firstly, the one-sample Kolmogorov–Smirnov test (alpha=5%) was applied to evaluate if the data followed a normal distribution. Then, the paired two-sided Wilcoxon sign rank test (alpha=5%) was applied between the conventional and improved approaches to evaluate if a statistically significant different was present. This is used to test differences of paired data without the normal distribution assumption.

6 Results

The results of this work will be presented in two sections:

- The new unfolding method, able to consider the fundus photography acquisition geometry, is compared with the conventional EYEPLAN unfolding method.
- Then, the fundus and MRI registration is evaluated by comparing the image based method developed in this work of thesis with the simplistic eye modelling that place the macula on the eye optical axis.

The evaluation metric that is used, has been already presented in the previous chapter and is applied for all the 10 patients. The evaluation of the 'image center method' is performed against the EYEPLAN model and then, once the new method's performance has been confirmed, it has been adopted as a standard unfolding method for the MRI part. As data didn't follow a normal distribution (Kolmogorov–Smirnov test, alpha=5%), the results will be presented hereafter using median and interquartile range. The statistical difference introduced by the methods proposed in this work will be evaluated using a paired two-sided Wilcoxon sign rank test (alpha=5%).

6. 1 'Image center' method evaluation

In Figure 53, the results of the comparison between the conventional and the novel unfolding method are graphically represented. For each patient, the values of the five evaluation metrics are reported: all the parameters are calculated by comparing the tumor delineations and the tumor contours that results from the unfolding operations. The red and blue points correspond to the EYEPLAN unfolding method and to the image center unfolding method, respectively.

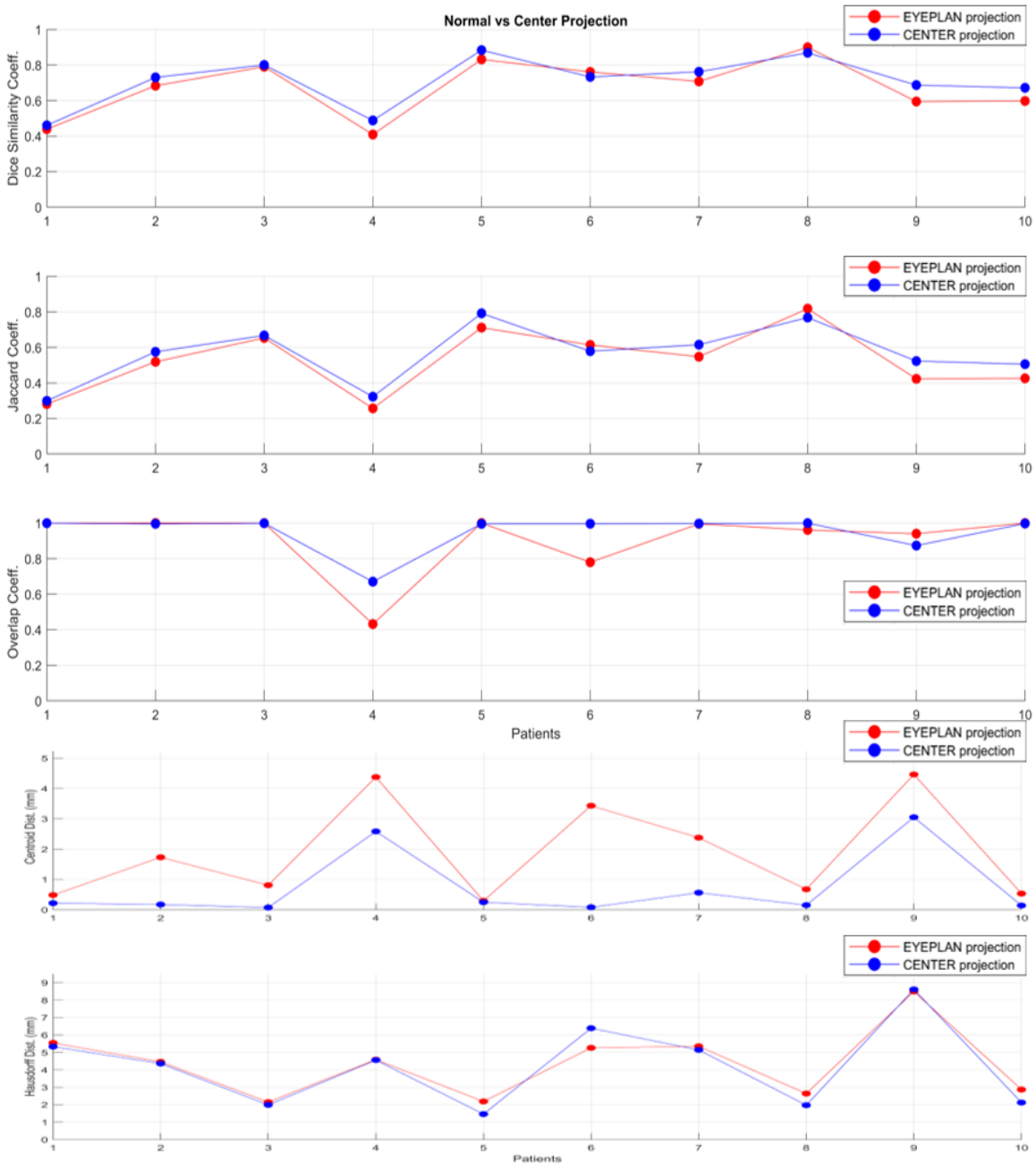

Figure 53- The behaviour of the following parameters is shown for each patient: Centroid distance, Hausdorff Distance, DSC, Jaccard, Overlapped Area.

The same results are summarised in Table 2.

Metric	*Eyeplan unfolding method*	*Image center unfolding method*	*Median difference*
DSC [a.u.]	0.69 ± 0.20	0.73 ± 0.13	+0.04
JACCARD [a.u.]	0.53 ± 0.23	0.58 ± 0.16	+0.05
OVL [a.u.]	0.96 ± 0.06	0.99 ± 0.01	+0.03
CENTROID DIST. (CD) [mm]	1.27 ± 2.89	0.19 ± 0.42	-1.08
HAUSDORFF DIST. (HD) [mm]	4.51 ± 2.70	4.40 ± 3.34	-0.11

Table 2- Comparison between the EYEPLAN unfolding method and the 'image center' method.

Dice similarity coefficient (DSC) varied from 0.41 (patient n. 1) to 0.92 (patient n. 8) and from 0.45 (patient n. 1) to 0.91 (patient n. 5), for the Image center and Eyeplan unfolding method, respectively. Jaccard and overlap coefficient (OVL) followed a similar distribution. For the conventional EYEPLAN method the first metric ranges from 0.24 to 0.81 and the second one from 0.42 to 1. The same metrics are slightly improved for the new method and go from 0.26 to 0.80 and from 0.69 to 1, respectively.

The comparison between the two methods showed significant improvement for the image center unfolding method with respect to the conventional one. On average, centroid distance (CD) decreased by 1.08 mm, while Hausdorff distance (HD) decreased by 0.11 mm. However, patients n° 6 and 9 presented worse HD with the novel method with an increase of 0.8mm and 0.05 mm, respectively. Nevertheless, the CD for the new method decreased for all the cases.

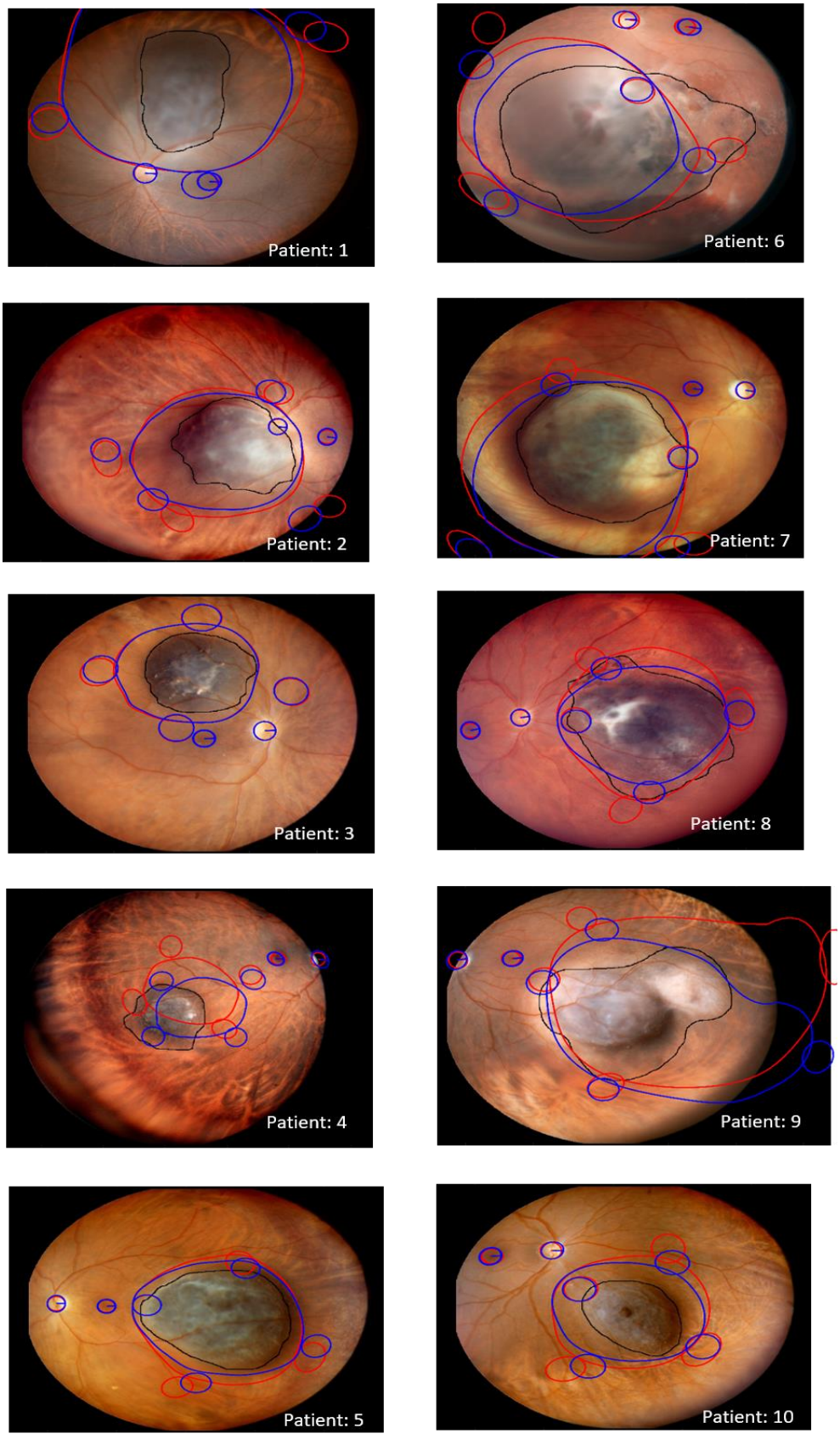

Figure 54- All the 10 patients are shown in this figure: the red contours are obtained with the conventional EYEPLAN method whereas the blue ones are generated according to the 'image center' method.

Fundus photography with superimposed tumour base contours produced using the two unfolding methods are depicted in Figure 54. In patient number 6, although macula and optic disk are fully visible and the registration process is successful, as the macula is located at the periphery of the fundus FOV, the application of our new unfolding method shows variations in the projected structures with respect to the EYEPLAN method, leading to a decrease in DSC and Jaccard index of 0.03 and 0.04, respectively, and an increase in the Hausdorff distance of 1.12 mm. The reason why the coefficients deteriorated is mainly due to the generosity with which the tumor delineation has been performed: in the segmentation process the radiation oncologist included also retinal area near the tumor where some satellites tumoral tissues could be present. Even if the projected structures generated with the 'image center method' show a reduction in the tangential distortion, the red tumor contour, obtained with the traditional EYEPLAN method, describes better the segmentation goodness.

As regards patient number 8, the macula is located at the fundus photography periphery similarly as patient 6. The same effect on results can be appreciated with DSC and Jaccard being worse, in comparison with the conventional EYEPLAN unfolding method, by 0.03 and 0.04, respectively. Nevertheless, for this patient CD and HD are lower in the proposed method than in the conventional one.

It is worth to highlight that our method is comparable with respect to the EYEPLAN's one when the macula (in the fundus) is located exactly at the image center or nearby. In this case, if the image center is folded back onto the 3D model, its position coincides with the macula's one. Patient 3 is an example of this situation: all the overlapping metrics are similar with discrepancies of about ±0.01.

Also, we would like to point out an additional benefit that our method would bring: the reduction of the distortion that affects the unfolded structures, as visible in Figure 2 for the projected clips.

Wilcoxon paired signed-rank test indicated that the comparison of tumor delineation on fundus photography and tumor base contour projection, using the EYEPLAN unfolding method and the novel proposed image center unfolding method, resulted significantly different (alpha= 0.05), attesting the effectiveness of our procedure.

6.2 MRI ‘image-based’ method Evaluation

Since it has been shown using EYEPLAN that the 'center method' is able to better overlap the tumour contour delineated in the model with the one on the fundus, this new method has been adopted for the implementation of the MRI and fundus fusion. The image-based method implemented in this work to register the fundus and MRI have been quantitatively evaluated against the adoption of the simplified eye model equal to EYEPLAN, that assumes the macula as located along the optical axis (geometrical projection). As a result, the comparison was implemented following these steps.

- Firstly, tumor contour coming from the conventional geometric projection based on the two anatomical constraints was compared to manual tumor delineation on fundus photography
- The tumor contour coming from the optimal macula selected with the T1 or T2 image-based method without the introduction of the second constraint was compared to the tumor delineation
- The tumor contour coming from the optimal macula selected with the T1 or T2 image-based method with the introduction of the second constraint was compared to the tumor delineation

By applying the one-sample Kolmogorov–Smirnov test, the data do not belong to a normal distribution, thus results will be presented using median and interquartile range.

In addition, the effect of the pre-processing algorithm on the original fundus photography before calculation of the MRI with virtual images has proven to affect the MI output. We will therefore present the result obtained based on the adoption of the pre-processing algorithm which provided the better performance. Then we will present the same results for the two other methods described in the previous section to demonstrate the significant impact that fundus image pre-processing has on the proposed method success.

6.2.3 Geometric projection vs 'image-based' method

For obtaining the pre-processed fundus that led to the best outcomes among the other pre-processing approaches, the LAB colour domain has been explored and the 'A' channel has been used. Subsequentially, a closing operation has been applied in order to reduce the information content that belongs to the blood vessel network. Furthermore, we tried to extrapolate only the tumor information, the one in which we are interested. This has been achieved by applying thresholding operations to both the fundus and the virtual images. In the following part the results belonging to T1 and T2 will be presented separately.

6.2.3.1 Geometric projection vs T1 image-based method

The results shown in Figure 55 and summarized in the second column of Table 3 are obtained by considering T1-weighted MRI and without the application of the second constraint for the optimal macula identification. The red and blue points correspond to the geometric projection method and to the image-based method, respectively.

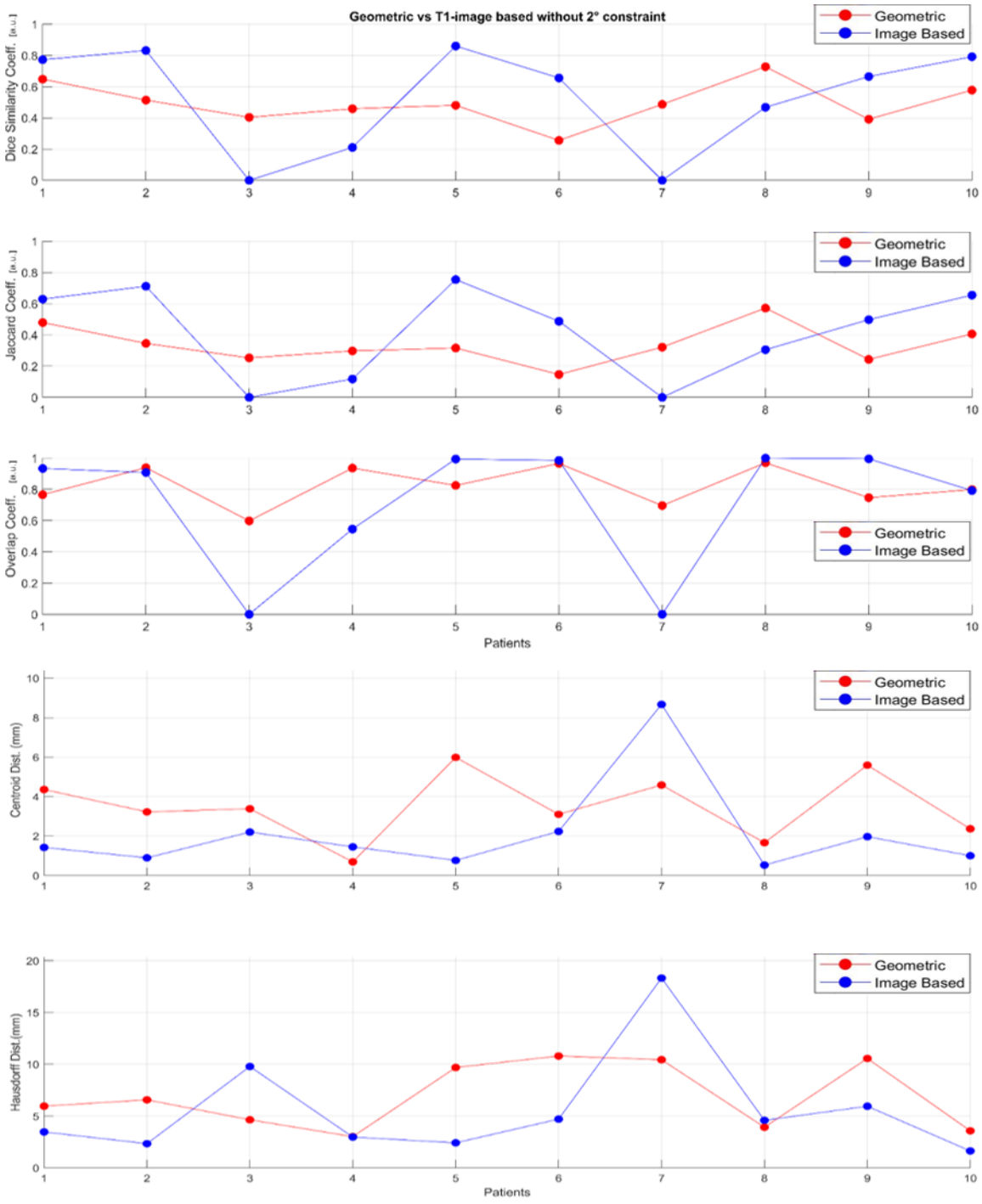

Figure 55- DSC, Jaccard, Overlapped Area, Centroid distance and Hausdorff Distance behaviour for each patient: the virtual images come from the T1 volume and the second constraint is not applied.

Figure 4 shows results relevant to the image-based approach with the additional contribution of the second anatomical constraint for the optimal macula identification (grouped analysis in Table 2).

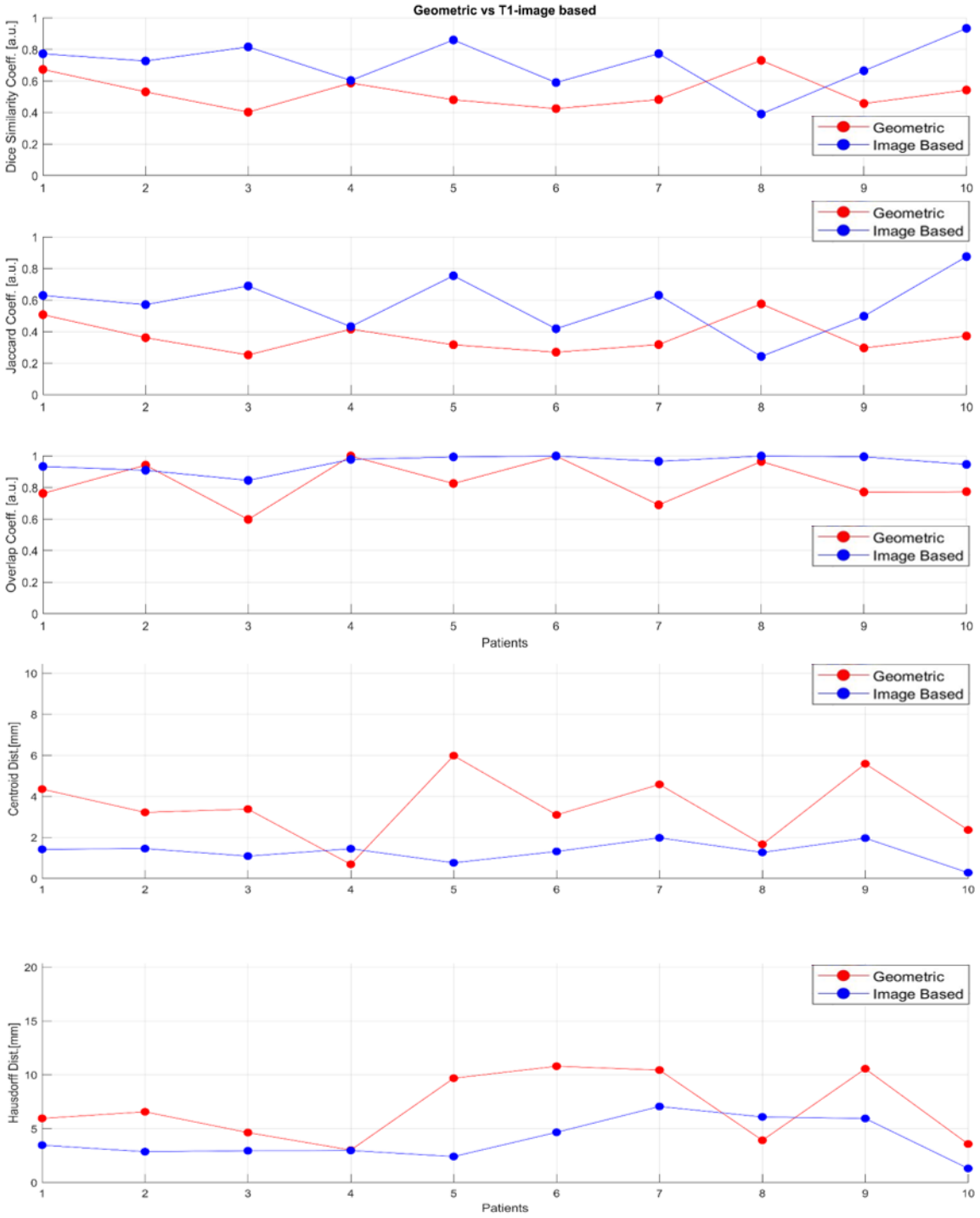

Figure 56- DSC, Jaccard, Overlapped Area, Centroid distance and Hausdorff Distance behaviour for each patient: the virtual images come from the T1 volume and the second constraint is now applied.

Metric	*Geometric approach*	*T1-weighted image-based approach without 2° constraint*	*T1-weighted image-based approach with 2° constraint*
DSC [a.u]	0.51 ± 0.13	0.66 ± 0.32	0.75 ± 0.21
JACCARD [a.u]	0.34 ± 0.12	0.49 ± 0.34	0.60 ± 0.26
OVL [a.u]	0.80 ± 0.20	0.95 ± 0.20	0.97 ± 0.06
CENTROID DIST. (CD) [mm]	3.30 ± 2.22	1.44 ± 1.31	1.37 ± 0.36
HAUSDORFF DIST. (HD) [mm]	6.25 ± 6.52	4.03 ± 3.53	3.21 ± 3.08

Table 3- Median and interquartile range of the Geometric projection and the T1 image-based method: both the cases have been analysed, without and with the introduction of the second constraint, respectively.

The results calculated without the introduction of the second constraint were promising for T1 compared to those obtained with the geometric approach.

DSC, Jaccard and OVL median values increased by 0.15, and CD and HD decreased of 1.56mm and 2.22mm, respectively. Moreover, the introduction of the second constraint for the macula identification led to a further improvement: compared to the geometric approach, DSC, Jaccard and OVL increased of 0.24, 0.26 and 0.17, respectively. The best outcomes were quantified in terms of the centroid distance (CD) and Hausdorff distance (HD): on average, CD decreased of 1.93mm, while HD decreased of 3.04mm. Also, the image-based method benefits from the inclusion of the second constraint: DSC, Jaccard and OVL increased of 0.09, 0.11 and 0.02, respectively. CD decreased of 0.07mm and HD of 0.82mm.

Furthermore, the application of the Wilcoxon paired signed-rank test suggested the effectiveness of the T1 image-based method against the geometric approach with significant differences (alpha= 0.05).

The contours generated for all the ten patients are depicted in Figure 57.

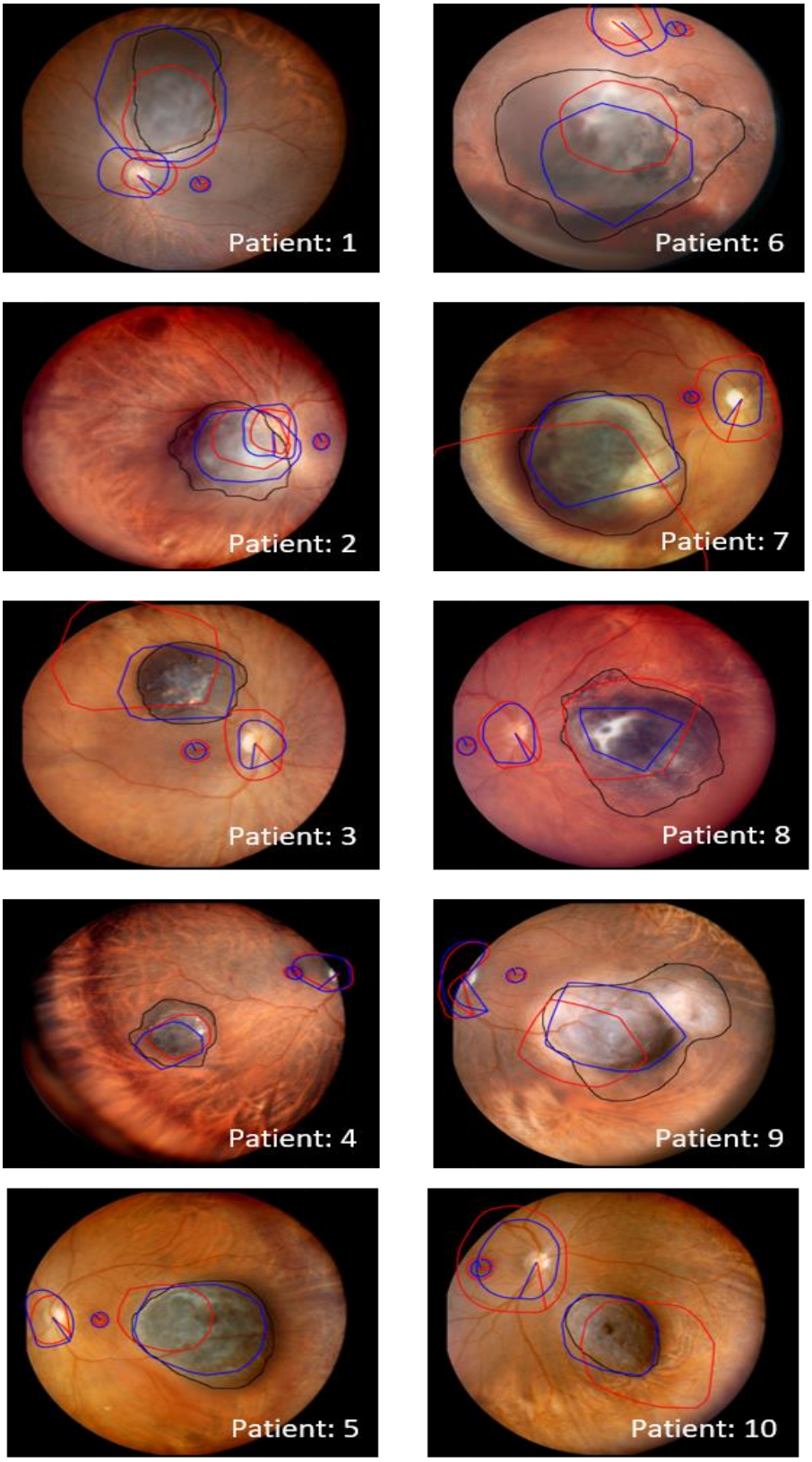

Figure 57- Comparison between the geometric projection (in red) and the image-based method without the introduction of the second constraint applied with the T1 volumes (in blue) for all the ten patients.

6.2.3.2 Geometric projection vs T2 image-based method

The results for the method, without and with the application of the second constraint for T2-weighted MRI are shown in Figure 58 and in Figure 59, respectively. The red points correspond to the geometric projection method and the blue ones to the image-based method.

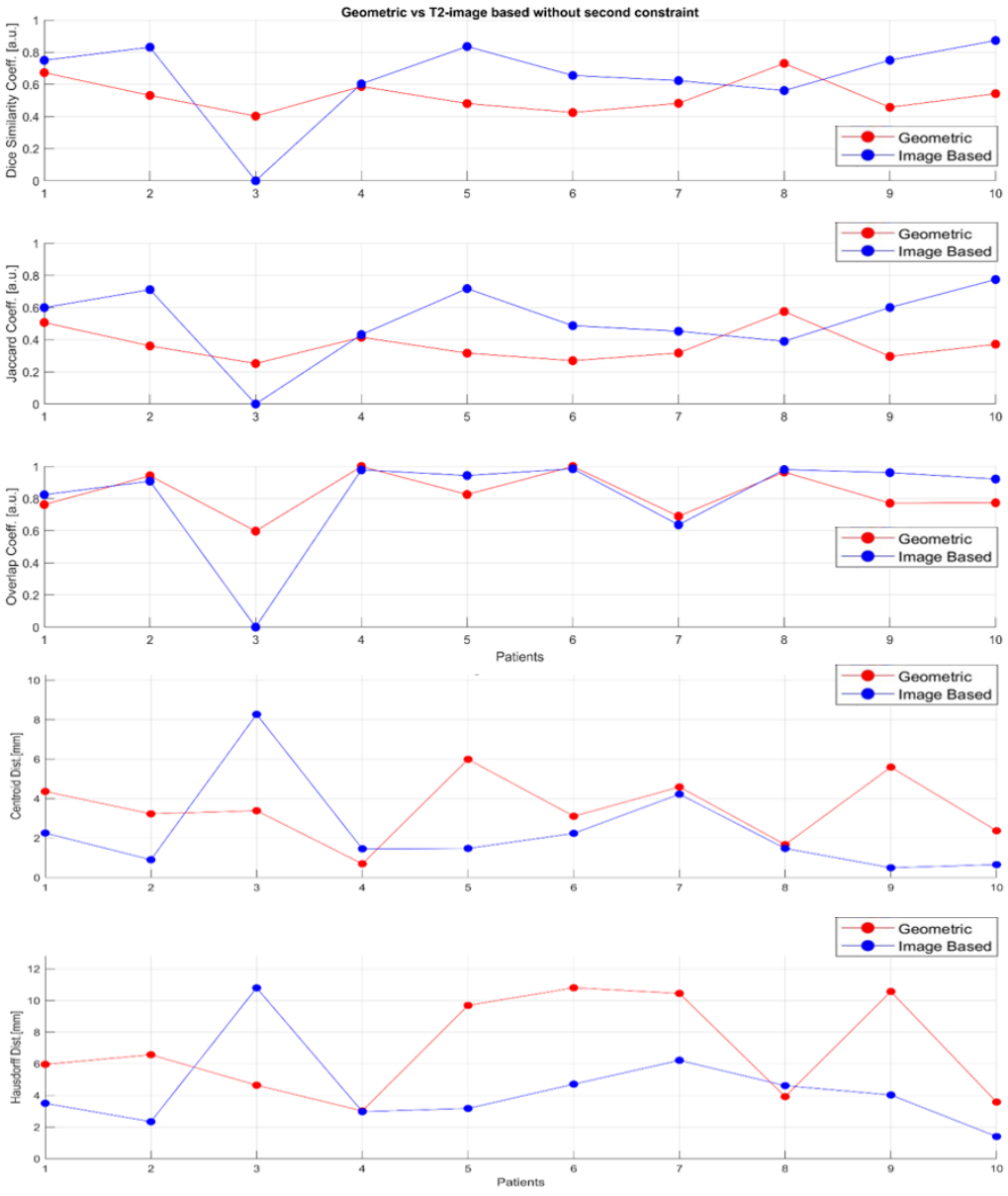

Figure 58-DSC, Jaccard, Overlapped Area, Centroid distance and Hausdorff Distance behaviour for each patient: the virtual images come from the T2 volume and the second constraint is not applied.

Figure 7 shows results with the introduction of the second constraint. Overall quantifications are reported in Table 4.

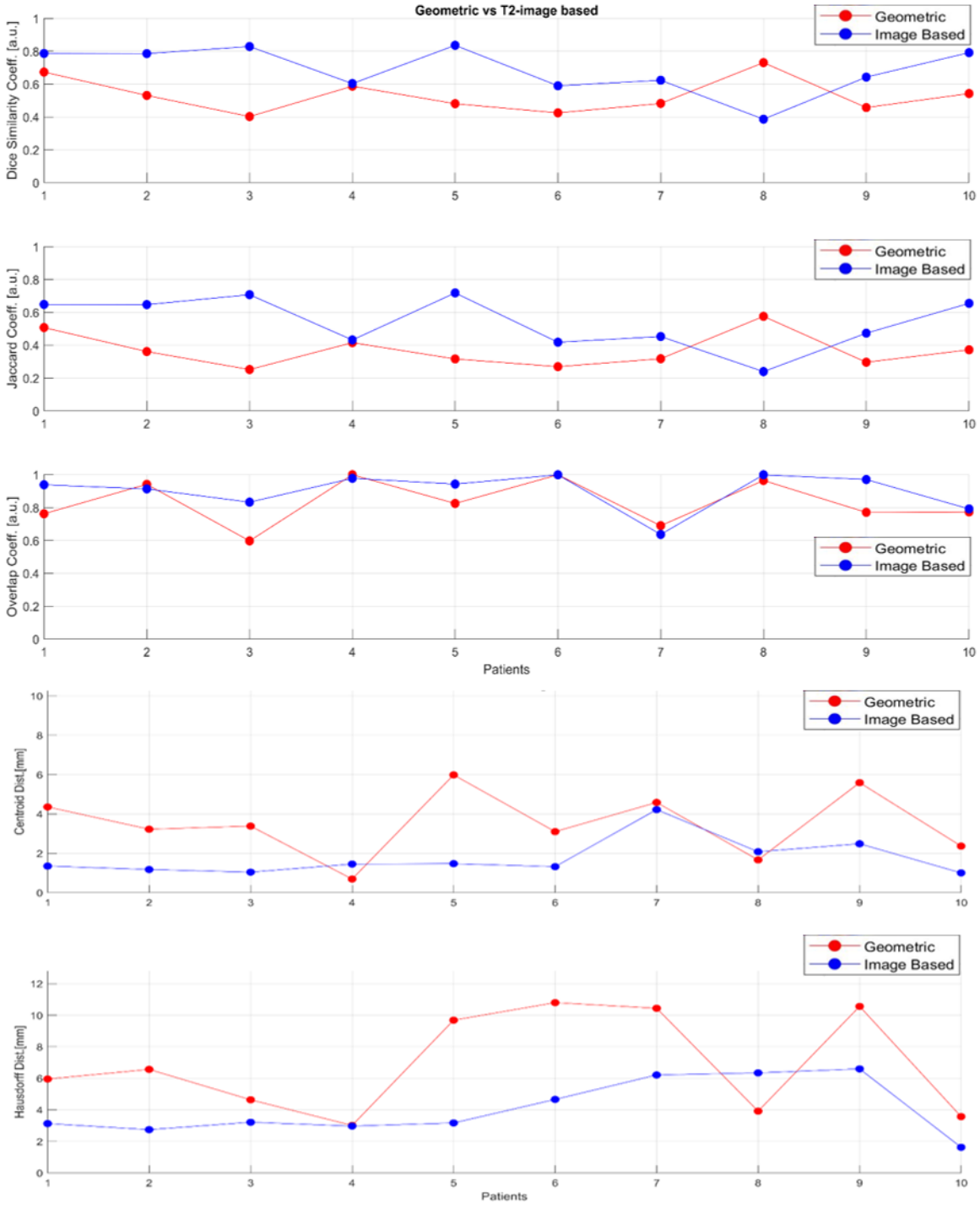

Figure 59- DSC, Jaccard, Overlapped Area, Centroid distance and Hausdorff Distance behaviour for each patient: the virtual images come from the T2 volume and the second constraint is introduced.

Metric	*Geometric approach*	*T2-weighted image-based approach without 2° constraint*	*T2-weighted image-based approach with 2° constraint*
DSC [a.u]	0.51 ± 0.13	0.70 ± 0.23	0.71 ± 0.19
JACCARD [a.u]	0.34 ± 0.12	0.54 ± 0.22	0.56 ± 0.22
OVL [a.u]	0.80 ± 0.20	0.93 ± 0.15	0.94 ± 0.15
CENTROID DIST. (CD) [mm]	3.30 ± 2.22	1.47 ± 1.35	1.41 ± 0.90
HAUSDORFF DIST. (HD) [mm]	6.25 ± 6.52	3.78± 1.73	3.20 ± 3.24

Table 4- Median and interquartile range of the Geometric projection and the T2 image-based method: both the cases have been analysed, without and with the introduction of the second constraint, respectively.

Also, by using the virtual images generated by the T2 volume, the metrics presented better values than those obtained with the geometric macula. All the median values calculated without the introduction of the second constraint improved: DSC, Jaccard and OVL increased by 0.19, 0.20 and 0.13, CD and HD decreased by 1.83mm and 2.47mm, respectively.

A slight improvement was obtained by introducing the second constraint. In this case the metrics increased with respect to the geometric approach by 0.20 for the DSC, 0.22 for Jaccard and for 0.14 for the OVL; at the same time Centroid distance (CD) and Hausdorff distance (HD) decreased by 1.89mm and 3.05mm, respectively. Before and after the introduction of the second constraint the metrics varied according to the following quantities: DSC and OVL increased of 0.01, Jaccard of 0.02, CD decreased of 0.6mm and HD of 0.58mm.

Fundus photography with superimposed tumour base contours produced using the geometrical approach (in red) and the T2 image-based method (in blue) are depicted in Figure 60. In order to provide a clear understanding, the boundaries generated before the introduction of the second constraint are omitted and only the one generated after the introduction are reported. The application of the Wilcoxon paired signed-rank test showed the differences (alpha=0.05) between the T2 image-based method and the geometric approach to be significant: the statistic test proved the superiority of the proposed procedure.

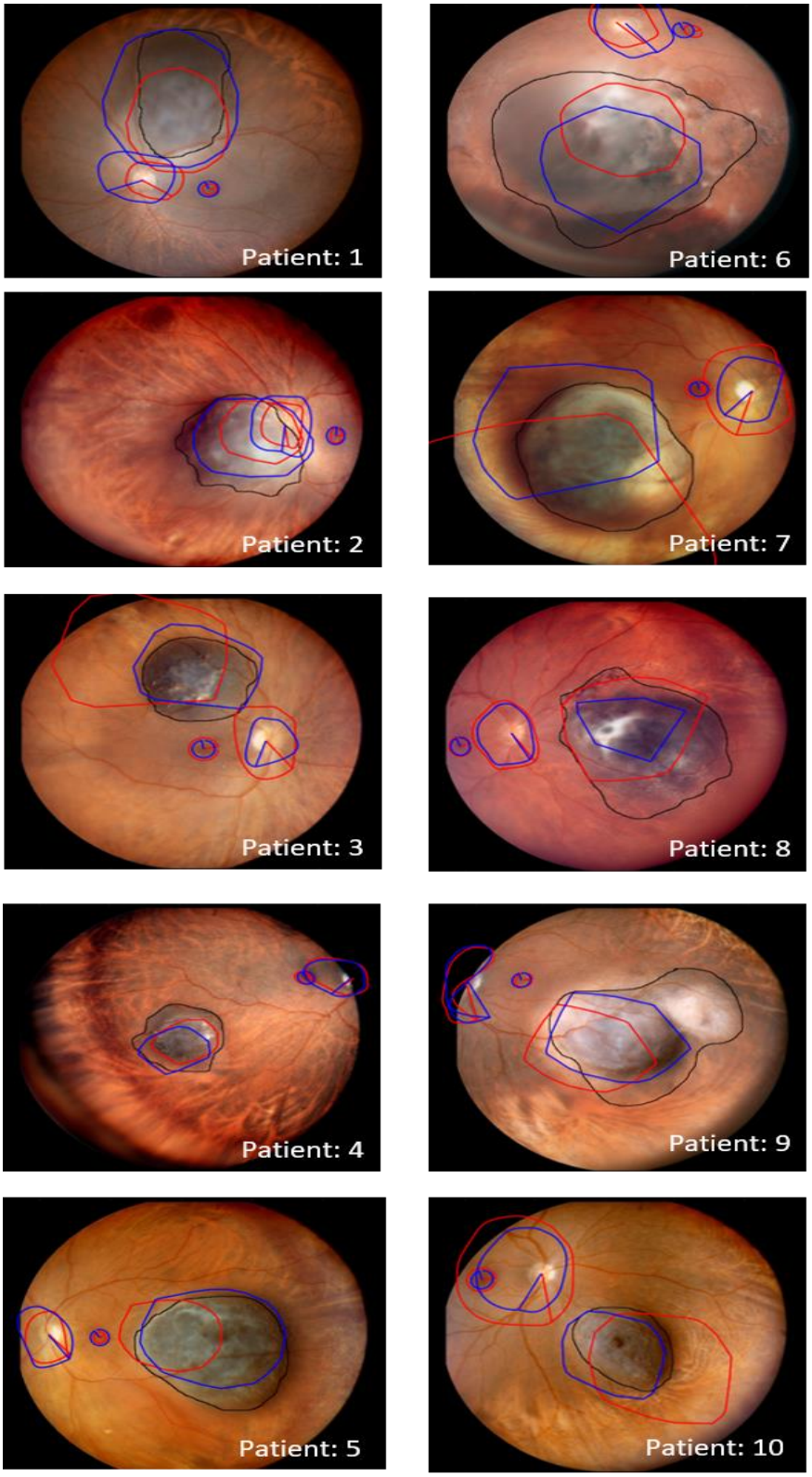

Figure 60- Comparison between the geometric projection (in red) and the T2 image-based method without the introduction of the second constraint (in blue) applied for all the ten patients.

6.2.3.3 T1 image-based method vs T2 image-based method

After having confirmed that the image-based method is superior in terms of accuracy with respect to the geometric one, it is necessary to establish which MRI volume, T1 or T2, produces better outcomes.

A comprehensive comparison between the T1 and the T2 image-based methods is resumed in Table 5.

Metric	*Geometric approach and T1 image-based difference*	*Geometric approach and T2 image-based difference*	*T1 image-based and T2 image-based difference*
DSC [a.u.]	+0.24	+0.20	+0.04
JACCARD [a.u.]	+0.26	+0.22	+0.04
OVL [a.u.]	+0.17	+0.14	+0.03
CENTROID DIST. (CD) [mm]	-1.93	-1.89	-0.02
HAUSDORFF DIST. (HD) [mm]	-3.04	-3.05	+0.01

Table 5- Comparison between the image-based methods. The use of the T1 volume shows better outcomes.

As displayed in the use of T1 virtual images led to a slight improvement in the quantitative metrics: in particular, DSC and the Jaccard coefficients increased of 0.04, OVL improved of 0.03 and the HD decreased of 0.02mm. However, the only value that confirms the superiority of the T2 virtual images is the Centroid distance (CD) that is decreased by 0.02mm compared to the T1 image-based method.

Another important evaluation that is perform is relevant to the number of iterations that each approach requires in order to meet the second constraint on the macula-optic disk distance. By analysing the graph shown in Figure 61 the number of iteration necessary to satisfy the second constraint varies from patient to patient. The mean number of iterations performed by considering the T1 and T2 were 2.8 and 3.9, respectively. The maximum and minimum number of iterations was found for patient 8, in which 9 and 18 iterations were necessary for T1 and T2, respectively.

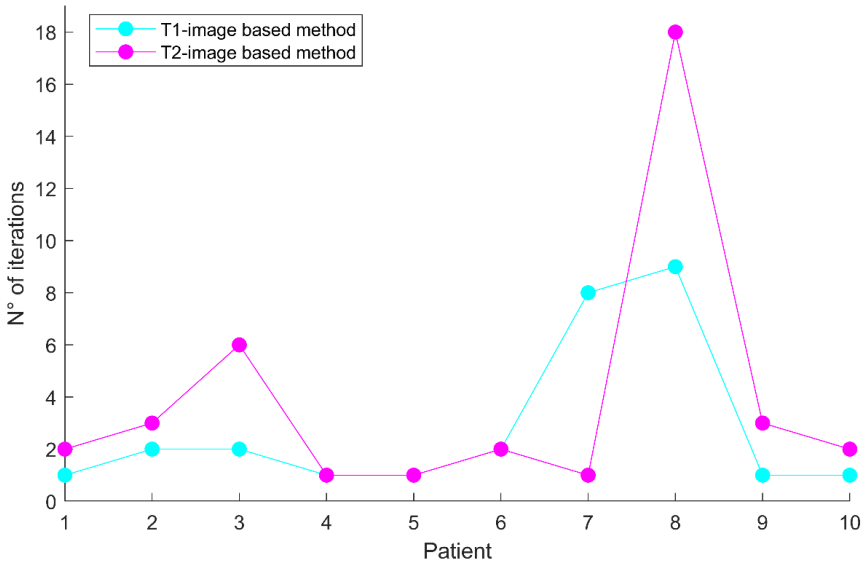

Figure 61- This graph shows the number of iterations that the algorithm performs before finding the optimal macula. The mean number of iterations for T1 is 2.8 and for T2 is 3.9.

Overall, as the parameters are slightly improved and the required number of iterations is smaller, we can state that the T1 image-based method is superior compared to the geometric one and is slightly better with respect to the T2 approach.

Wilcoxon paired signed-rank test indicated that the comparison of tumor delineation on fundus photography and tumor base contour projection using the EYEPLAN unfolding method and the novel proposed image center unfolding method resulted significantly different (alpha= 0.05), attesting the effectiveness of our procedure.

6.3 Additional analysis

In the following section are reported the results that have been obtained by using the other pre-processing procedure of fundus images (refer to chapter 4.2.7).

Table 6 resumes the values of the quantitative metrics (expressed in terms of median an IQR) for both the T1 and T2 image-based methods belonging to the first pre-processed fundus. For clarity, the values obtained before the introduction of the second constraint are omitted.

Metric	*Geometric approach*	*T1-weighted image-based approach with 2° constraint*	*T2-weighted image-based approach with 2° constraint*
DSC [a.u.]	0.53 ± 0.11	0.52 ± 0.23	0.51 ± 0.23
JACCARD [a.u.]	0.36 ± 0.11	0.39 ± 0.21	0.38 ± 0.22
OVL [a.u.]	0.83 ± 0.14	0.75 ± 0.25	0.72 ± 0.31
CENTROID DIST. (CD) [mm]	3.50 ± 1.67	3.17 ± 1.69	3.59 ± 2.19
HAUSDORFF DIST. (HD) [mm]	6.91 ± 3.16	5.71 ± 2.40	6.96 ± 2.62

Table 6- Median and interquartile range of the Geometric projection and the T1 and T2 image-based methods performed with the first pre-processed fundus. Only the cases in which the second constraint is introduced are reported.

Here, the fundus image was obtained by converting the original RBG fundus into a gray level values and then, by performing the complement. As reported in Table 6, this pre-processing does not introduce any advantage with respect to the geometric approach for both the T1 and T2. In particular, for the T2 image-based method, none of the metrics improved, whereas for the T1 approach the centroid distance (CD) and the Hausdorff distance (HD) decreased by 0.33mm and by 1.20 mm, respectively.

The second pre-processing set up investigated was the HSV colour domain. The channel S was selected and the complement has been performed. Median and IQR are summarized in Table 7.

Metric	*Geometric approach*	*T1-weighted image-based approach with 2° constraint*	*T2-weighted image-based approach with 2° constraint*
DSC [a.u.]	0.53 ± 0.11	0.60 ± 0.16	0.59 ± 0.19
JACCARD [a.u.]	0.36 ± 0.11	0.54 ± 0.17	0.45 ± 0.18
OVL [a.u.]	0.83 ± 0.14	0.89 ± 0.06	0.88 ± 0.13
CENTROID DIST. (CD) [mm]	3.50 ± 1.67	1.7 ± 0.53	2.3 ± 1.18
HAUSDORFF DIST. (HD) [mm]	6.91 ± 3.16	4.08 ± 1.66	5.26 ± 2.04

Table 7- Median and interquartile range of the Geometric projection and the T1 and T2 image-based methods performed with the second pre-processed fundus. Only the case in which the second constraint is introduced are reported.

With this pre-processing, DSC improved by 0.07 and 0.06 with respect to the geometric approach values, for T1 and T2 respectively. The Jaccard showed a similar behaviour and increased by 0.18 and 0.09, the OVL increased by 0.06 and 0.05 respectively. HD and CD decreased by 1.80 and by 2.83 mm for T1, and by 1.20mm and 1.38 mm, for T2.

7 Discussion and Conclusion

7.1 'Image center' method

The method that we have implement is an alternative for unfolding the structures included in an ocular three-dimensional eye model on the fundus image. In both the conventional and our proposed methods, the retinal unfolding is performed by having a point as the projection center and the radial distances on the bi-dimensional map correspond to the arc lengths on the 3D eye surface. This approach guarantees that the relative distances between the projected points are consistent to the spherical representation in the radial direction. However, this transformation does not guarantee point-to-point distance preservation along all the unfolded circumferences on the 3D spherical eye surface that do not pass across the projection center. This results in a distortion effect that is more prominent for unfolded structures that are further away from the projection center. In EYEPLAN, regardless of patient specificity the macula is always considered as the projection center. Therefore, if it is located in the fundus image periphery, the conventional EYEPLAN unfolding procedure may produce significant inconsistencies with the fundus as the structures are more affected by this distortion.

The method we proposed and tested considers the fundus image center as center of projection. This procedure accounts for the variation of the image acquisition geometry caused by the operation with the aim of completely guaranteeing the tumor visibility. This approach leads to the generation of more truthful projections through the reduction of contours' distortions. This is only a partial mitigation of the uncertainties affecting fundus photography acquisition but, nevertheless a significant one as demonstrated in the analysis. Indeed, the analyses performed on the proposed approach attested the effectiveness of the method, which resulted significantly different with respect to the conventional procedure. For most of the patients indeed, HD and CD were lower in the proposed approach than the EYPLAN' ones. On average, the Centroid distance and the Hausdorff distance decreased of 1.08mm and 0.11mm, respectively.

Patient n°8 resulted in slightly worse results for the proposed method than the EYEPLAN one, with a decrease in DSC and Jaccard of 0.11 and 0.13, respectively. However, by visually inspecting the unfolded boundaries belonging to both methods (see Figure 54) is visible that the 'image center' method encompasses more tightly the bulk of the tumor as visible on fundus photography, whereas the traditional unfolding method includes a broader area due to the distortion related to the macula being located in the periphery of the image. The delineations performed on fundus photography also extend to very thin infiltrations of the melanoma in the choroid and are therefore numerically better fitting the EYEPLAN projection method.

It is worth to highlight that the fundus photography acquisition system is complex, and the resulting displayed retinal image will be affected by distortion. During the fundus image acquisition, light rays reflected from the spherical retinal surface are mapped onto a planar image after traveling the two-way path through the cornea and a series of camera's lenses. The light rays will suffer nonlinear distortions due to the spherical shape of retinal surface. In fact, when a curved surface is projected onto a plane, objects are distorted: as one moves away from the focal center the effects of the distortion are more pronounced.

However, through the use of ocular mocks or planar grids is possible to geometrically calibrate the fundus camera allowing for curved distortion compensation. Is therefore impossible to completely estimate the fundus camera optic: the complex optical system created between the internal camera's lenses and the patient lens cannot be modelled and standardized, as the crystalline shape is patient specific and its contribution, in terms of optical properties, is always different. Furthermore, artefacts related to possible patient eye movements and related to the fact that being the Panoret designed for handheld use, any movement of the device, could introduce additional distortions.

Although in our work the patient subset was limited only to ten patients, our method therefore demonstrated its superiority against the conventional EYEPLAN one and its ability in reducing some of the above-mentioned uncertainties, especially the ones related to the acquisition, by means of a pinhole camera, of a curved object. Due to the improved outcomes, this novel unfolding method has been adopted as a standard one for the MRI part.

Surely, to confirm the consistency of our ‘image center’ method compared to the conventional EYEPLAN one, is necessary to test it on more cases. In particular, as in our dataset the tumors were always centered on the fundus FOV, it would be interesting to evaluate how the algorithm will respond for patients in which the tumor is located in the fundus image periphery.

7.2 MR ‘image based’ method

The second part of the work aimed at realizing a multimodal patient specific eye model through the integration of the fundus imaging with MRI. Fusing the fundus with MRI is an important step towards the creation of a more accurate eye model, able to combine the volumetric MRI information with the high-resolution details of the fundus photography.

As already said, the registration between the fundus photography and whatever model must be performed by using macula and optic disk, as they are the only two available landmarks detectable in the fundus photograph. The conventional treatment planning system EYEPLAN defines the optic disk and macula position within the model according to a standardized geometrical eye model that neglect any kind of patient specificity. In particular, the macula is approximated to be at the intersection between the optical axis and the sclera surface, although its real position, as the literature suggests, is defined at the intersection between the visual axis and the sclera surface.

The two ocular structures definition in the MR model, according to the EYEPLAN approximations, and the following unfolding operation (by mean of the ‘image center’ method) and registration with the fundus, have been implemented in the so called ‘Geometric approach’. As it is the replica of how the actual TPS places macula and optic disk within the 3D model, this approach has been used for the comparison with our proposed method.

The registration between MR volume and fundus image has been already investigated by De Zanet et al., (De Zanet, Ciller, Rudolph, & Maeder, 2010). In their approach, the same two ocular landmarks are adopted for MRI to fundus fusion, but the macula position is identified according to anatomical population-based considerations which constrain the macula to belong to the visual axis. Although the increase in the accuracy for the macula detection

compared to EYEPLAN, the anatomical constraints that have been used depend on a population-based average eye model rather than a patient-specific one (see details in section 1.5.1).

In our approach, the registration between MRI and fundus images relies as well on optic disk and macula, but the position of the latter in the MRI 3D eye model is established through an image-based approach which take into account patient-specific variability. Specifically, a set of virtual images are generated with a 'pseudo-ray tracing' approach, and these are compared with the real fundus photography through the mutual information (MI) metric. The virtual image with the highest similarity value with respect to the fundus is chosen and the patient specific macula position is found.

Overall, the proposed approach has been demonstrated to provide more accurate results compared to the Geometric approach. When considering just the optimal macula identified by the MI value, an average improvement for the T1 approach of 35.5%, was quantified for the Hausdorff distance (HD) metric.

Nevertheless, the macula identification depends on the performance of the MI metric. Thus, we decided to evaluate the distance between the selected macula and the optical disk, in order to: (i) provide a figure of merit able to evaluate the robustness of the MRI algorithm and (ii) improve the proposed procedure by including this as an anatomical constraint (in an average eye it should be between 4.0mm and 4.8 mm (De Silva, et al., 2006))in the registration process. Specifically, after having selected the 'optimal macula' candidate, the algorithm evaluates if its position satisfies this constraint. If so, the macula is found, otherwise, the algorithm iteratively repeats this operation until the macula with the highest value of MI that satisfies the requirement is selected. On average, 2.8 iterations were required for T1-weigthed MRI and 3.9 iterations for T2-weighted MRI, suggesting that MI should be combined with the anatomical constraints. Indeed, when the second anatomical constraint was introduced in the algorithm for the definition of the optimal macula, we observed an improve in the T1 approach of 49%, on the Hausdorff distance (HD) metric compared to the geometric one.

This is explained by the fact that the MI performance is significantly influenced by the type of pre-processing that is applied on both the fundus image and the virtual images. As shown in the result section, three different pre-processing methods have been tested. We noticed

that, with a more effective pre-processing applied to the fundus image, a better output is provided by MI algorithm. Indeed, the amount of information stored in the fundus image is significantly greater than the one brought by the virtual images derived from MRI: the Panoret machine provides high quality and high-resolution images, in which not only the principal organs information is stored but also the vessels network and the retinal colours. This superior amount of information affects the MI metric. The proposed pre-processing entails a closing procedure and a median filter followed by a thresholding operation. The thresholds adopted in our study were defined empirically for T1-weighted and T2-weighted MRI, thus requiring further analyses for a more robust and powerful pre-processing. Furthermore, the adoption of the 'a' channel within the LAB colour domain enhances the characteristics of the colours from green to red, thus improving the contrast between the retina and the other structures.

The pre-processing results in a decrease in the information content of the original fundus image but in an improved similarity with corresponding MRI-based virtual projection thus guaranteeing a better performance of the MI algorithm.

Another factor that affects the generation of virtual images is the selection of points belonging to the sclera. All the structures are indeed manually segmented by a radiation oncologist which could potentially introduce operator-dependent uncertainties. For example, in case of T1-weighted images, the humour vitreous is detected as a low signal whilst the tumor and the sclera surface are detected as a high signal. If the sclera contour includes points that are located in the external sclera, the high signal that they possess is stored together with the tumor's ones in the virtual images.

It must be noticed that partial volume effects and the lack of a proper gradient variation between different structures make more difficult the sclera delineation. The MR imaging was indeed performed without the use of any contrast agent, which makes more difficult tumor and organs delineation. A novel MRI data campaign acquisition, currently ongoing at PSI, is using MRI contrast agents to improve the visibility of the internal structures inside the eye. We believe that the application of the 'pseudo-ray tracing' algorithm to the new T1 MRI volumes will provide higher quality virtual images.

Overall, our results show that the virtual images generated fromT1-weighted MRI are more promising compared to those derived from T2-weighted MRI. This superiority is confirmed

by comparing the quantitative metrics and also by visually inspecting the fundus images. On average, DSC and the Jaccard coefficients are grater by 0.04, OVL by 0.03 and the HD is lower by 0.02mm.

Another limitation that needs to be highlighted regards flat and small tumors. It has been stated from Daftari and Via (Via, et al., 2020) that the MRI fails in detecting tumors whose height is less that 3mm. If the tumor is not detected in the MR volumes, the virtual images do not include any information on the lesion and the comparison with the fundus is meaningless since the image-based method is based on a similar content between the two. We expect that the fundus photography will play an important and primary role in the identification of such tumours. As suggested by this preliminary study, a multi-modal information from different imaging techniques is mandatory for accurate ocular treatments.

In addition to the above-mentioned limitations which are mainly linked to the macula identification, one has also to consider that the optic disk needs to be identify in the MRI scan, which at the moment is derived from the literature-derived anatomical constraint.
The optic disk position can be derived from the optic nerve structures as they are identifiable in the T1 MRI volumes as bright and tubular structures. The intersection between the optic nerve head (ONH), i.e. the terminal part of the nerve attached to the eye globe, and the external scleral surface defines the optic disk. It is clear that an improper delineation of the ONH and the sclera surface could lead to an error in the optic disk position. In this case, a minimum variation could affect all the algorithm as the optic disk is used for: (i) MI figure of merit and (ii) as a registration landmark. Actually, the way in which the optic disk is defined is error-prone and an important future development will be the implementation of a fully automatic method able to increase the segmentation accuracy.

As mentioned before, at PSI, an MRI campaign acquisition is ongoing and soon new data will be available, providing the possibility of testing our method on new cases. Furthermore, the introduction of contrast agents during the MR acquisitions will enhance structures visibility, allowing for better contouring and for a less noisy virtual images generation.
As a step forward, a dosimetric comparison between the conventional EYEPLAN eye model and the MRI one should be performed. Differences in the eye model used for planning could have impact on the treatment for two reasons: firstly, the variation of the shape of the eye

(sclera surface) could result in changes in the dose distribution, and secondly, the enhanced CTV, obtained through the additional fundus information requires an adjustment of the delivered dose to the target volume.

7.3. Final remarks

Overall, our work aims at the realization of a patient-specific multimodal eye model in which the MRI defined structures can be combined with the imaging information present in the fundus photography. This would potentially provide a personalized model with respect to the current clinical procedure, as implemented in the EYEPLAN TPS. Furthermore, the conventional EYEPLAN unfolding method has been improved and the novel one accounts for the variations in the fundus acquisition geometry leading to a more accurate fundus fusion. Our study is therefore the first attempt for the definition of an improved and personalized eye model, including, in an innovative modality, the information from different imaging sources, which can serve as a groundwork towards clipless ocular proton therapy (OPT).

Besides the fact that some of the main challenges of clipless OPT have already been investigated, there are still many problems to be faced before a clipless workflow becomes clinical reality. The current treatment set a high standard, against which all innovations must be benchmarked. Nevertheless, the potential to be able to provide a more comfortable and economic treatment for ocular tumors justifies further developments and research into the possibilities of a clipless approach, of which this work would give its contribution.

8 Acknowledgements

I would like to thank my Supervisors Prof. Baroni and PhD Hrbacek Jan for letting me work on an important project in one of the more prestigious Research Institute in Switzerland. This international experience at PSI has made me grow both personally and professionally. Furthermore, I would like to thank my Co-Supervisors Riccardo and Chiara for all their teachings and for having helped me in the realization of this amazing work. I also would like to thank the guys and the PhD with whom I shared the long office hours during this experience at PSI.

A heartfelt thank you goes to all of my university friends with whom I shared these years and enjoyed each moment (I won't mention them one by one because, trust me, they are so many that I would need another thesis), especially to all of my ' I 💔 Zucchina' friends. Also, I would like to thank my housemates with whom I shared the best apartment in Milan, only them will know what happened in that house. A special thanks you to my friend Andrea, business and study partner. I would like to thank all my friends from Gorlago for the many adventures we luckily survived from and especially to the 'Branco'.

I'd like to enormously thank Sally, Rosie and Jamie that during the last summer allowed me to spend with them a month in Cornwall and to improve my English.

A super thank you to my girlfriend Erica, who has always supported and encouraged me to achieve every predetermined objective. Now I reached the goal and without her I know for sure that I wouldn't have climbed the peak.

I don't know if I can find the right words to thank my parents and family, but I'd love this achievement, as far as possible, to be also for them a reward, for the many sacrifices that they have done. An endless thanks for always being there and for supporting me. Thanks for each advice, for your critics that pushed me to mature!

Finally, I would like to dedicate this work to my best friend, my dog Black, that now isn't with me anymore.

Thanks

9 Bibliography

Abràmoff, M., Garvin, M., & Sonka, M. (2011). Retinal Imaging and Image Analysis.

Arepalli, S., Kaliki, S., & L., S. (2015). Choroidal metastases: Origin, features, and therapy.

Bechrakis, N., Blatsios, G., & Hass, G. (2015). Short review of the history of radiotherapy for intraocular tumors. *Klin Mombl Augenheilkd*.

Broehan, M., Rudolph, T., Amstutz, C., & Kowal, J. (2011). Real-time multimodal retinal image registration for a computer-assisted laser photocoagulation system. *IEEE Trans. Bio-Med*.

C.O.M.S. (1990). Accuracy of diagnosis of choroidal melanomas in the Collaborative Ocular Melanoma Study.

Carnicer, A. e. (2013). Quantification of dose perturbations induced by external and internal accessories in ocular proton therapy and evaluation of their dosimetric impact.

Char DH. (1978). The management of small choroidal melanomas. *Surv Ophtalmol*, 22:377-86.

Daftari, I., Aghaian, E., O'Brien, J., Dillon, W., & Phillips, T. (2005). 3D MRI-based tumor delination of ocular melanoma and its comparison with conventional techniques.

Daftari, I., Mishra, K., O'Brien, J., Tsai, T., Park, S., Sheen, M., & Phillips, T. (2010). Fundus image fusion in EYEPLAN software: an evaluation of a novel technique for ocular melanoma radiation tratment planning.

Damato B. (2001). Detection of uveal melanoma by optometrists in the United Kingdom. *Ophtal. Physiol. Opt, 21(4),*, 268-271.

Damato, B. (2004). Developments in the management of uveal melanomas. *Clinical and Experimental Ophtalmology*.

De Silva, D., Cocker, K., Lau, G., Clay, S., Fielder, A., & Moseley, M. (2006). Optic disk size and optic disk-to-fovea distance in preterm and full-term infants. *Invest. Ophthalmol. Visual Sci., vol. 47,*.

De Vera, P., Abril, L., & Garcia-Molina, R. (2018). Energy Spectra of Protons and Generated Secondary Electrons around the Bragg Peak in Materials of Interest in Proton Therapy.

De Zanet, S., Ciller, C., Rudolph, T., & Maeder, P. (2010). Landmark Detection for Fusion of Fundus and MRI Towards a Patient-Specific Multi-Modal Eye Model.

Descovich, M., Sneed, P., Barbaro, N., McDermott, M., Chuang, C., Barani, I., . . . Lijun, M. (2010). A dosimetric comparison between Gamma Knife and CyberKnife treatment plans for trigeminal neuralgia.

Dieckmann, K., Langmann, G., Ma, R., Schmutzer, M., Poetter, R., Wackernagel, W., & Zehetmaye, M. (2004). Uveal malignant melanoma: management options – stereotactic radiotherapy.

Dobler, B., & Bendl, R. (2002). Precise modelling of the eye for proton therapy of intra-ocular tumours. *Physics in Medicine and Biology, 47*(4), 593-613.

Durante, M., Orecchia, R., & Loeffler, J. (2017). Charged-particle therapy in cancer: clinical uses and future perspectives.

Egger, E., Schalenbourg, A., Zografos, L., Bercher, L., Boehringer, T., Chamot, L., & Goitein, G. (2001). Maximizing local tumor control and survival after proton beam radiotherapy of uveal melanoma. *International Journal of Radiation Oncology*, 138-147.

Evans, C., Nestoridis, A., Papadopoulos, A., & Rimm, N. (2004). Spherical arc-length for analytic curves in the Riemann sphere.

Finger, P., Berson, A., & Szechter, A. (2002). Palladium-103 Plaque Radiotherapy for Choroidal Melanoma: An 11-Year Study.

Fuss, M., Loredo, M., Blacharski, P., Grove, R., & Slater, R. (2001). Proton radiation therapy for medium and large chorodial melanoma:preservation of the eye and its functionality.

Gala, F. (2015). Magnetic resonance imaging of optic nerve.

Goitein, M., & Miller, T. (1983). Planning proton therapy of the eye. 275-283.

Gragoudas, E. (2006). Proton beam irradiation of uveal melanomas: the first 30 years. 4666-4673.

Gragoudas, E., Li, W., Goitein, M., Lane, A., Munzenrider, J., & Egan, M. (2002). Evidence-based estimates of outcome in patients irradiated for intraocular melanoma.

Gundzu, K., & al., e. (1999). Radiation Retinopathy Following Plaque Radiotherapy for Uveal Melanoma.

Jonas, R., Wang, X., Yang, H., Jun Li, Y., Xu, L., Panda-Jonas, S., & Bruno Jonas, J. (2015). Optic Disc - Fovea Distance, Axial Length and Parapapillary Zones. The Beijing Eye Study 2011.

Jovanovic, P., Mihajlovic, M., Djordjevic-Jocic, P., Vlajkovic, S., Cekic, S., & Stefanovic, S. (2013). Ocular melanoma: an overview of the current status.

Kacperek, A. (1995). Ophthalmological Proton Facilities. *Ion Beams in Tumor Therapy* , 360-370.

Kacperek, A. (2012). Ocular proton therapy centers: Ion beam therapy.

Kellner, U., Bornfeld, N., & Foerster, M. (1993). Radiation-induced optic neuropathy following brachytherapy of uveal melanomas.

Laube, T., Fluhs, D., Kessler, C., Fiscia, L., & Bornfeld, N. (2007). Determination of Surgeon's Absorbed Dose in Iodine-125 and Ruthenium-106 Ophthalmic Plaque Surgery Ophthalmology.

LD, P., Chong, N., & Au, S. (2015). Optomap ultrawide field imaging identifies additional retinal anomalies in patients with diabetic retinopathy . 527-531.

Mahendraraj, K., Lau, C., Lee, I., & Chamberlain, R. (2016). Trends in incidence, survival, and management of uveal melanoma: a population-based study of 7,516 patients from the Surveillance, Epidemiology, and End Results database. 2113—2119.

Marnitz, S. C. (2006). Proton Therapy of Uveal Melanomas: Intercomparison of MRI-Based and Conventional Treatment Planning .

Maschi, D., Thariat, J., Heault, J., & Caujolle J. (2015). Tumor response in uveal melanomas treated with proton beam therapy. *Clinical Oncology*.

McLaughlin, C., Wu, X., Jemal, A., Martin, H., Roche, L., & Chen, V. (2005). Incidence of noncutaneous melanomas in the U. S. Cancer.

Merle, L., Arthur, B., Eugene, J., & Donn, M. (1960). The relative Biological Effectiveness of cobalt-60 Gamma Rays and 220Kvp X-rays on the viability of chicken Eggs.

Mourtada, F., & Koch, N. N. (2005). 106Ru/106Rh plaque and proton radiotherapy for ocular melanoma: a comparative dosimetric study.

Muller, K., Nowak, P., De Pan, C., Marijnissen, J., DA, P., Levendag, P., & GP, L. (2005). Effectiveness of fractionated stereotactic radiotherapy for uveal melanoma.

Newhauser, W. D. (2007). Dosimetric impact of tantalum markers used in the treatment of uveal melanoma with proton beam therapy. . *Physics in Medicine and Biology,*.

Olsen, D. B. (2007). Proton therapy- a systematic review of clinical effectiveness. *Radiotherapy and oncology* .

Perret, C. C. (1988). Die behandlung intraokularer melanome mit protonen.

Recsan, Z. K., & Fodor, M. (2002). MRI for the evaluation of scleral invasion and extrascleral extension of uveal melanomas.

Sas-Korczyska, B., Markiewicz, A., Romanowska-Dixon, B., & Pluta, E. (2014). Preliminary results of proton radiotherapy for choroidal melanoma.

Schaeffel, K. (2002). Kappa and Hirschberg Ratio Measured with an AutomatedVideo Gaze Tracker. *Optometry and vision science*, 79(5):329–334,.

Simiantonakis, I., Cordini, D., & Fuchs, H. (2005). Comparative treatment planning for proton therapy of eye tumours with EYEPLAN and OCTOPUS. *Biomed tech*.

Sing, M., Turell, M., & BA, T. (2011). Uveal Melanoma: Trends in Incidence, Treatment, and Survival.

Stefan, R. (2004). Proton therapy of uveal melanomas in Berlin.

Tataru, C., & Pop, M. (2012). ENUCLEATION IN MALIGNANT CHOROIDAL MELANOMA - results in 15 years of using a new material in the prosthesis of the orbital cavity.

Via, R., Fassi, A., Fattori, G., Fontana, G., Pella, A., Tagaste, B., . . . Baroni, G. (2015). Optica eye tracking system for real-time noninvasive tumor localization in external beam radiotherapy.

Via, R., Henning, F., Beer, J., Pica, A., Peroni, M., Fattori, G., . . . Hrbacek, J. (2020). MRI based eye and tumor modeling for ocular proton therapy and its dosimetric impact.

Weber, D. e. (2005). Proton beam radiotherapy versus fractionated stereotactic radiotherapy for uveal melanomas: A comparative study. *Internation Journal of Radiotion Oncology Biology Physics.* , 373-384.

Wuestermayer, H. e. (2006). Proton radiotherapy as an alternative to exenteration in the management of extended conjunctival melanoma.

Yu, G., Hu, D., McCormick, S., & Finger, P. (2003). Conjunctival melanoma: is it increasing in the United States? .